Politecnico di Torino

Master's degree in Biomedical Engineering

Department of Mechanical and Aerospace Engineering

Master's thesis in Biomechanical Engineering

"Development of an applicative model to filter outliers from intra-operative acquired data in Total Knee Replacement using Computer Assisted Surgery"

Supervisor
prof.ssa Cristina Bignardi
Co-supervisor
Ing. Simone Bignozzi
Ing. Ruben Giagnoni

Candidate
Ilenia Moneta
S253822

A.A. 2019-2020

A Bea
alla forza che hai già dentro,
prima ancora di venire al mondo

e a tutta la Vita che ci aspetta.

Table of contents

Acronyms

TKA Total Knee Replacement

RANSAC Random Sample Consensus

MAE Mean Absolute Error

CAS Computer-Assisted Surgery

THR Total Hip Replacement

ACL Anterior Cruciate Ligament

PCL Posterior Cruciate Ligament

CT Computer Tomography

MRI Magnetic Resonance Imaging

RS Reference System

ML Medial-Lateral

AP Anterior-Posterior

NURBS Non-Uniform Rational B-Splines

TRE Target Registration Error

PCA Principal Component Analysis

RMSE Root-Mean-Squared Error

SSM Statistical Shape Model

ICP Iterative Closest Point

MDL Minimum Description Length

ASM Active Shape Models

MCT Minimum Consensus Threshold

RP Reference Point

MPC Medial Posterior Condyle

LPC Lateral Posterior Condyle

MDC Medial Distal Condyle

LDC Lateral Distal Condyle

TME Tibial Medial Emiplateaux

TLE Tibial Lateral Emiplateaux

Abstract

In orthopaedic surgery, with a special focus on Total Knee Arthroplasty (TKA), planning the intervention is of fundamental importance. The rate of success of the surgery is strictly connected to the right alignment of the prosthesis. In order to improve overall alignment and to minimize situations of gross positioning, systems for computer-assisted total knee arthroplasty have been introduced. These systems use computer technology for surgical planning, for guiding or performing surgical interventions. Orthopaedic surgeons use computer-assisted systems to acquire the surface of the bone, so that the software can reconstruct the patient-specific morphology and plan the most appropriate cut, depending on the characteristic of the intervention and on the surgeon's specifications. The efficacy of this technology relies much on the correct use of the system by the surgeon, who must understand the basic principles and try not to commit errors during the registration phase. The work herein presented shows a method to detect and filter wrong acquisition from intra-operative data, to improve the performances of the system and lead to good results even if the registration phase is not optimal. Several methods from the literature were analysed, and the most suitable for our purpose was found to be an algorithm that is already used in many medical images application: Random Sample Consensus (RANSAC). In order to carry out an implementation of the method, a mathematical function that describes the bone's morphology was found both in a two-dimensional and three-dimensional space. The mathematical model and the algorithm itself were subject to some parameters, which were defined through an optimization process. The final model was the most likely to fit the data acquired by the surgeon in the operating room and find eventual outliers. Tests to validate the model were carried out on three different datasets: real intra-operative data and two sessions of in vitro experiments on plastic specimens. Since there is no information about the data acquired on patients, the validation is only based on the last two sets of acquired points, which were collected by reporting the acquisition modality and the presence or absence of outliers. In this way, a comparison was made between the expected result and the output of the algorithm. The two validation datasets were acquired in different conditions: the first one was taken with complete awareness of how the algorithm works, and the second one was taken by three different operators, who know the surgical procedure and the software functioning, but not exactly every algorithm's step. The results show a 97% decrease in errors occurrences for the first validation, and the application of RANSAC leads to better results compared to the case where the algorithm

is not applied: the Mean Absolute Error (MAE) decreases from 5,14 $\pm 3,93$ mm to 0,43 $\pm 0,48$ mm. As regards the second validation, the improvement induced by the application of the algorithm is less evident: a 49% decrease in errors occurrences is reached, with MAE reduced from 3,0 $\pm 3,07$ mm to 1,14 $\pm 1,53$ mm. Differences in results suggest a dependence of the performances of the algorithm on the system know-how and expertise achieved by the surgeon that effects the acquisition, who must understand which movements must be avoided during the registration so as not to incur gross errors.
The present algorithm shows an excellent compromise between precision and computational costs (which rise to 31 ms in the worst case) and is meant to be applied in the BLU-IGS® software, a CAS system provided by Orthokey Italia s.r.l.

Introduction

In the last few decades, Total Knee Arthroplasty (TKA) has seen huge technological growth, due to the development of new techniques, materials, design and the possibility to help the surgeon in some accurate practices to be performed during the surgery.
The main reason that could lead the patient to undergo a TKA is osteoarthritis, which causes pain and the reduction of knee functionality. More than 90% of people undergoing knee prosthesis have experienced a significant reduction in knee pain and an improvement in their ability to perform common daily life activities. However, it is important to evaluate the risks and the benefits of this solution, which could imply some complications and the failure of the implant. From the 2018 annual report on arthroplasty in Italy, published by R.I.A.P. ("Registro Italiano ArtroProtesi"), it emerged that more than 25,000 knee arthroplasty surgeries were performed in 2017, of which 96% were primary surgeries. In the United States, the situation is much more pronounced: over 300,000 knee replacements are performed each year [13], a number which is expected to increase 525% by the year 2030. Most of knee replacement patients have a successful outcome after the surgery: patients report pain relief and the ability to perform basic tasks they could not do before the intervention. Although prosthetic surgery is undoubtedly a successful surgery, about 10% of the implants will fail and will require a second surgery, called "revision", to remove the old implants and replace them with new components. Prosthetic revision surgery, however, is a complex procedure that requires extensive preoperative planning, specialized implants and instruments, and mastery of difficult surgical techniques to achieve a good result. This is not a factor to be underestimated if we think that the patient could be in old age and, most of all, that a further surgery implies a greater removal of original bone, weakening it further. Fortunately, most knee prostheses will work well for the rest of the patient's life. Today we can reasonably say that modern prostheses should work for between 10 and 20 years in 90% of patients [7].
In this context, computer-assisted surgery (CAS) takes its place, to assist the medical equipment and let the arthroplasty be successful as much as it is possible, reducing the possibility to commit human errors. CAS and robotics have been introduced many years ago for joint replacement with the purpose to improve the accuracy in prosthesis components alignment. They also may represent for surgeons a significant incentive and stimulus to improve the surgical technique and an effective way to a better quality of life for patients. Literature data compared CAS with standard joint replacement technique and showed

statistically significant differences in prosthesis component alignment, in particular for the femur. The use of CAS or robotics in clinical practice is in the order of 8–10% of all TKR and less than 2–3% in Total Hip Replacement (THR). When using a CAS system, the surgeon literally "navigates" the bone's surface with instruments that are detected by an infrared camera: the software then reconstructs specific landmarks useful to plan the ideal cut, based on patient-specific morphology.

Due to the widespread of TKA and to the perspective of improvement on the results and precision of the intervention, the development of new technologies is subject of many studies. This work has been carried out at Orthokey s.r.l., an Italian company based in Florence, which designs and manufactures CAS systems in the orthopaedic field. Thanks to the relationship that the company maintains with customers in the clinical sector, some critical issues have emerged during the utilization of the systems in the operating room, which are meant to be solved, to improve the performances and the satisfaction of both the surgeons and the patients.

Aim of this thesis is to find the best solution to the problem of filtering the data acquired during the surgery, from which the planning of the arthroplasty takes place, relating the BLU-IGS® navigation system. It is possible that the surgeon acquires the bone's surface including some mistaken points (henceforth called "outliers"), and this could lead to a bad plan and the possible failure of the intervention. A good strategy to delete unwanted data will bring better results of the surgery itself, as long as this does not constitute a limit for added computational costs.

The thesis begins with two introductive chapters, which contain an overview on knee joint arthroplasty and surgeries characteristics, providing a global view of the problem and the essential knowledge to understand the terminology and background of the present study. Chapter 3 is dedicated to the state-of-the-art relating all the strategies which are currently used to solve similar or related problems: the described studies constituted an important outset for the realization of the proposed method, which is represented by the Random Sample Consensus algorithm. The chosen strategy is represented by an iterative method to estimate parameters of a mathematical model from a set of observed data containing outliers. The algorithm is described in all its aspects in Chapter 4, presenting the parameters that must be set and their meaning. In Chapters 5 and 6, the strategy used to find the best model is addressed, providing the failures and successes achieved, which lead to the definition of the best fitting model. The experimental set up involves the description of the mathematical model used to fit the data and the materials employed, which mainly consist of the points' coordinates included in the log file assembled by the software during the registration phase. The methods used to build the datasets are explained in detail, as well as the analysis of the indicators used to quantify the results. Chapter 7 and 8 concern the results and their discussion, while a summary of the achievements and limits of the presented method is given in the conclusions in Chapter 9. Future works are then suggested to improve the performances or apply the method for other purposes related to TKR.

Chapter 1

Knee Joint Arthroplasty

The knee is one of the largest joints in the human body and due to its complexity, it has been deeply studied. A short background is required to understand the field of the present study, with a focus on the anatomy of the knee, the diseases which cause pain and impossibility of motion, and the prosthesis characteristics.

1.1 Knee Anatomy

The knee joint consists of two articulations: tibiofemoral and patellofemoral. It is made up of bones, cartilage, ligaments, tendons and other tissues. The knee joint is a hinge joint: it can allow the leg to extend and bend back and forth with minimal side-to-side motion. Flexion and extension (and a small degree of medial and lateral rotation) are facilitated by the presence of the synovial capsule, which contains the synovial fluid.

1.1.1 Bones

The bones involved in this joint are the femur (thig bone), the tibia (shin bone) and the patella (kneecap), as shown in Figure 1.1. The patella is located in an indentation of the femur, called the intercondylar groove. These three bones are covered with articular cartilage, which has an important role to decrease the friction forces thanks to its smoothness and hardness. The fibula (the smaller shin bone) is not involved in the knee joint, but it is an important insertion point for the muscles.
The distal part of the femur is characterized by two condyles (the medial and the lateral), that form the proximal articulating surface. They are separated inferiorly by the intercondylar notch and connected anteriorly by the intercondylar groove. The presence of the patella articulating with the anterior part of the femur, makes the tendon to be inserted over the knee, increasing the efficiency of the muscles and the power of the extensor and works as a stabilizing structure.
The tibia also has two asymmetrical and flat surfaces (medial and lateral) in the proximal part, called tibial plateau.

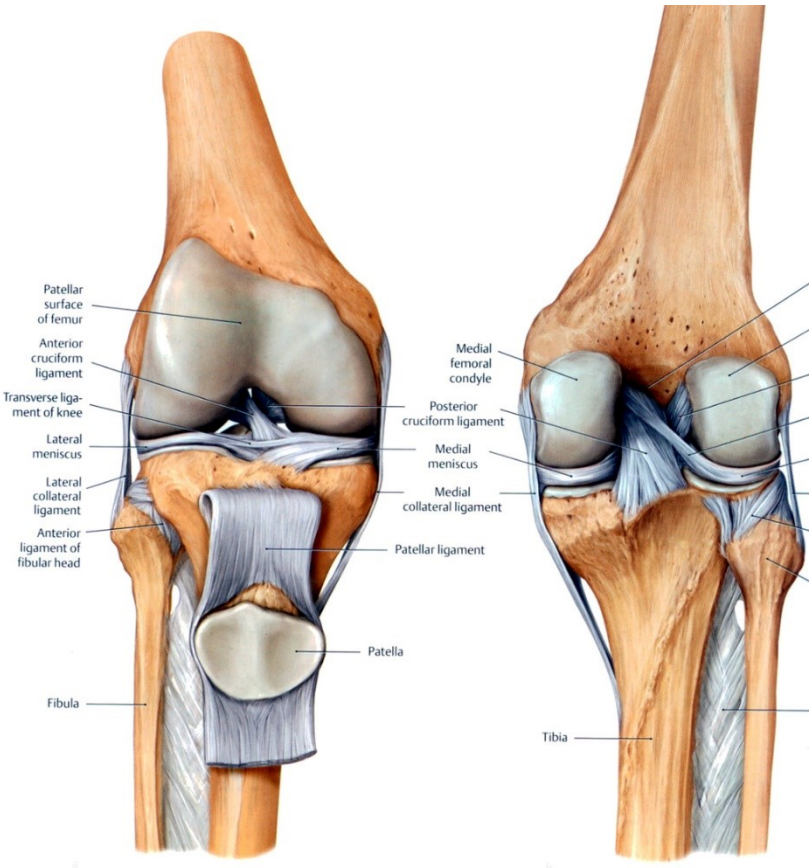

Figure 1.1: Structure of the knee joint, including bones, ligament, and menisci. All the main components and their relationships are represented. [31]

1.1.2 Cartilage

The cartilage in the knee joint can be classified into two types: the articular cartilage and the menisci. The first one can be found at the end of the bones and its purpose is to provide a slippery surface so that the contiguous bones can slide easily against each other. The menisci are two pieces of fibrocartilage structures between the bones in the knee joint. The medial and lateral menisci are C-shaped even if the lateral one appears more O-shaped, due to the increased size of the medial one (which can expose a large area to injuries). The menisci are attached at both ends to the intercondylar area of the tibia and the medial meniscus is fixed to the tibial collateral ligament and the joint capsule (see Figure 1.2). The lateral meniscus is smaller and does not have any extra attachments, thus making it fairly mobile.
The main functions of each meniscus are to:

- distribute the impact and weight on the bone surface, thanks to the arrangement of the fibres in the structure;
- correct the lack of congruence between the articular surfaces of tibia and femur;
- deepen the articular surface of the tibia, increasing the stability of the joint;

- act as shock absorbers by increasing surface area to further dissipate forces;
- guide and coordinate knee motion.

The surface of each meniscus is concave superiorly, providing a congruous surface to the femoral condyles and is flat inferiorly to accompany the relatively flat tibial plateau.

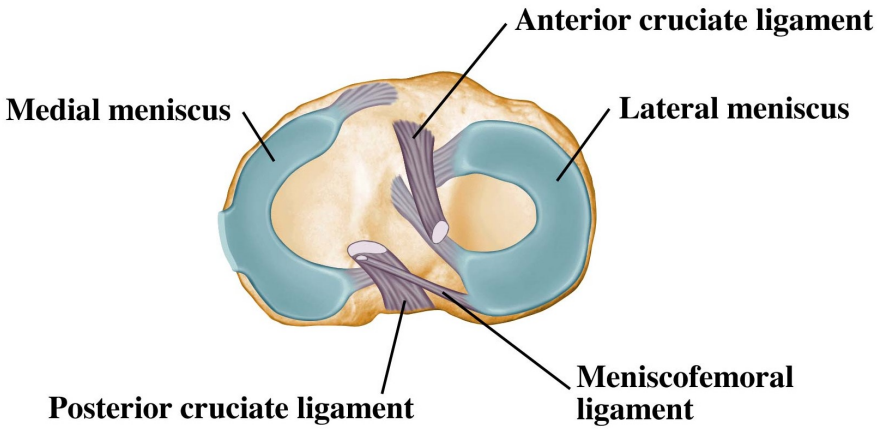

Figure 1.2: Superior top view of the right knee: lateral meniscus and medial meniscus are shown with their particular shape as well as their connection with the cruciate ligaments.

The stability of the knee is due particularly to the ligaments and to the structure of the joint capsule. The latter has thick and fibrous layers superficially and thinner layers in the deep. A specialized membrane called synovial membrane is found inside the capsule, to provide nourishment to all the surrounding structures. The membrane produces synovial fluid to lubricate the joint, which is pushed anteriorly during extension and posteriorly in flexion. As a function of cushions, we can find also the infrapatellar fat pad and the bursa, a synovial fluid-filled sac that reduces the wear and tear of the joint.

The ligament in the knee joint are the following (Figure 1.3):

- Patellar ligament: it is a continuation of the quadriceps femoris tendon and it attaches to the tibial tuberosity;
- Collateral ligaments: two strap-like ligaments that stabilize the hinge motion, preventing excessive medial or lateral movement
  - Tibial medial collateral ligament: it resists the valgus forces acting from the outer surface of the knee and it can prevent the anterior translation of the tibia on the femur;
  - Fibular lateral collateral ligament: it can resist varus forces on the knee and prevent the anterior translation of the tibia on the femur;
- Cruciate ligaments: two ligaments that connect the femur and the tibia, crossing each other

- Anterior cruciate ligament (ACL): it prevents anterior dislocation of the tibia onto the femur and it is responsible for resisting anterior shearing forces on the knee and rotatory forces medially and laterally as well as valgus and varus forces;
- Posterior cruciate ligament (PCL): it prevents posterior dislocation of the tibia onto the femur, it can resist posterior translation and shearing forces in the knee, and it plays an important role in resisting rotation and valgus/varus forces on the knee;

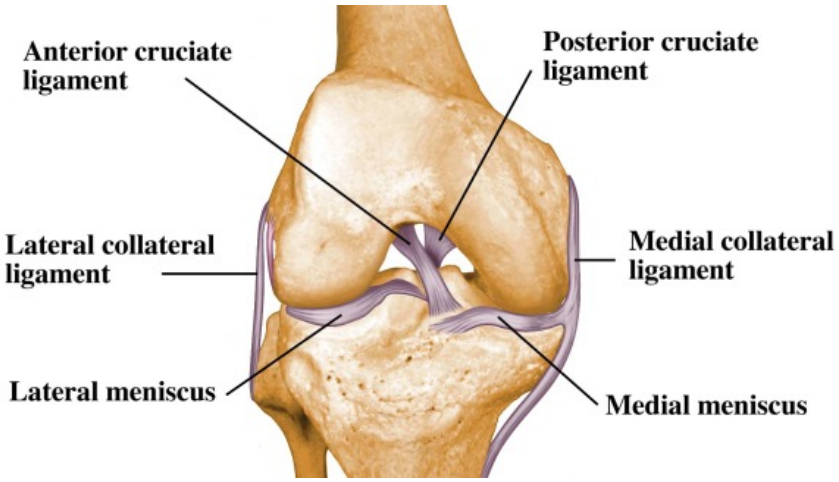

Figure 1.3: Representation of the knee ligaments and their contribution to knee stability. [31]

1.1.3 Muscles

There are four main movements that the knee joint permits:

- Extension: produced by the quadriceps femoris
- Flexion: produced by the hamstrings, gracilis, sartorius, and popliteus
- Lateral rotation: produced by the biceps femoris
- Medial rotation: produced by the semimembranosus, semitendinosus, gracilis, sartorius and popliteus

Lateral and medial rotation can only occur when the knee is flexed (if the knee is not flexed, the medial/lateral rotation occurs at the hip joint).

1.1.4 Reference axes

The main axes of the femur, in the near-distal direction, are two: the anatomical axis and the mechanical axis (Figure 1.4). The first one refers to the line that connects the

centre of the diaphysis of the femur and the centre of the knee (intercondylar groove). The mechanical axis refers to the line that connects the centre of the femoral head and passes through the centre of the knee into the centre of the ankle joint. It represents the axis of the femoral loads and it lies in a direction that forms an angle in the range of 5° - 7° with the anatomical axes.
In the case of the tibia, the axis is unique and is the anatomical one: the connecting line goes from the centre of the knee and the centre of the ankle. The diaphyseal axis of the tibia coincides with the distal area of the load axis of the lower limb.
Since the proximal-to-distal mechanical axis forms an angle of 3° with the midline vertical axis of the body, there typically exists a 3° angle between the knee joint line and the axis of the tibial shaft, and a 9° angle between the joint line axis and the axis of the femoral shaft.

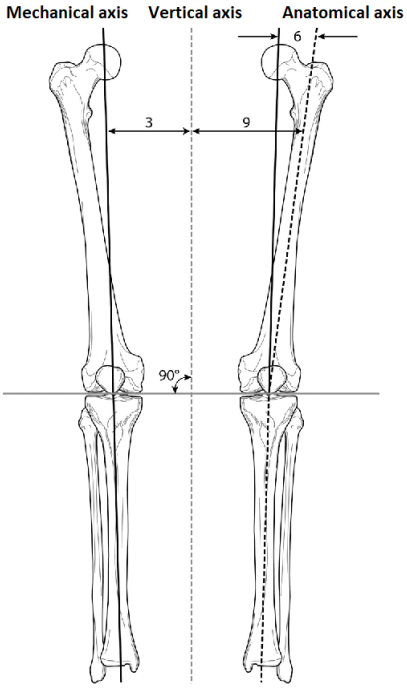

Figure 1.4: Representation of the mechanical and anatomic axes of the femur and the angles between them. The relationship with the vertical axis is also shown. [21]

The reference axes for positioning the prosthesis are the following (Figure 1.5):

- *Trans-epicondylar axis* connects the medial epicondyle to the lateral one;
- *Whiteside line* joins the lowest point of the trochlear sulcus and the centre of the sulcus;
- *Posterior condyle axis* connects the posterior points of the condyle medial and lateral

All three of the axes are defined in the transverse plane (see Appendix C for Anatomical planes and axes). The line of Whiteside and the Trans-epicondylar axis appear to be

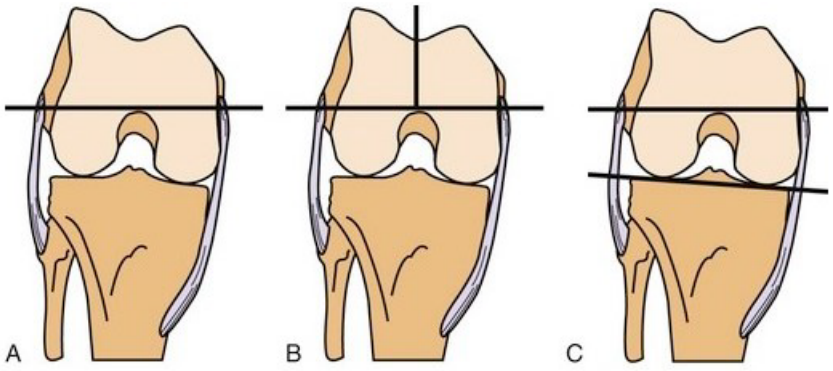

Figure 1.5: Reference axes for the positioning of the prosthetic femoral component. A: transepicondylar axis; B: Whiteside line; C: condyle axis. [36]

perpendicular to each other, while between the trans-epicondylar and the posterior condyle axes 3° of rotation are permitted.

1.2 Osteoarthritis

Osteoarthritis is the most common type of arthritis and it occurs when the cartilage wears away letting the bones' surfaces rub against one another causing pain, swelling, stiffness, decreased ability to move and, sometimes, the formation of bone spurs (Figure 1.6). The chance of developing osteoarthritis rises after age 45, but it can occur even in young people.

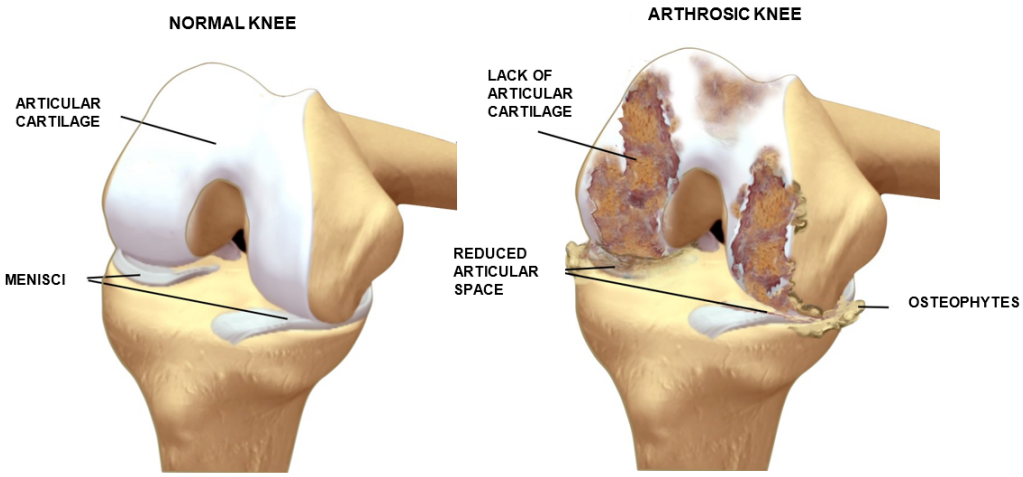

Figure 1.6: Normal and arthrosis knee are represented in comparison. [35]

Many factors can lead to osteoarthritis [51]:

- Age: the ability of cartilage to heal decreases as a person gets older
- Weight: it increases pressure on all the joints, especially the knees
- Heredity: this includes genetic mutations that might make a person more likely to develop osteoarthritis of the knee

- Gender: women are more likely to have osteoarthritis than men in old ages, due to the lower estrogen levels - which normally arise as a result of menopause – that is associated with greater production of bone-destroying cells
- Repetitive stress injuries: usually linked to the type of job a person has
- Athletics: soccer, tennis, or long-distance running may lead to a higher risk for developing osteoarthritis of the knee, even if regular moderate exercise strengthens joints and can decrease the risk
- Other illnesses: people with rheumatoid arthritis, the second most common type of arthritis, or people with certain metabolic disorders are also more likely to develop osteoarthritis

The primary goals of treating osteoarthritis of the knee are to relieve the pain and return mobility. The treatment plan will typically include a combination of the following [43]:

- Weight loss: losing even a small amount of weight can significantly decrease knee pain
- Exercise: strengthening the muscles around the knee makes the joint more stable and decreases pain
- Pain relievers and anti-inflammatory drugs
- Injections of corticosteroids or hyaluronic acid into the knee: steroids are powerful anti-inflammatory drugs, while hyaluronic acid is normally present in joints as a type of lubricating fluid
- Use of devices such as braces
- Surgery: when other treatments don't work
  - Arthroscopy: it is performed with small incisions through which the instruments and the camera (arthroscope) can enter and with which the surgeon can remove the damaged cartilage and repair the tissues. This kind of surgery is performed for young patients to delay more invasive solutions.
  - Osteotomy: the surgeon changes the shape of the bone by cutting parts of it in order to make a better alignment.
  - Arthroplasty: also called joint replacement surgery, it is a surgical procedure in which joints are replaced with prostheses. The replacement could involve one side of the knee or the entire knee. It is performed for patients with severe osteoarthritis aged 50 or more.

1.3 Knee prosthesis

Knee prosthesis is composed of three or four parts, as it is shown in Figure 1.7: the femoral component, usually in cobalt-chrome alloy, is fixed to the distal part of the bone; the tibial component in metallic materials, usually titanium alloy, that is fixed to the proximal part of the bone; between the two metallic components, there is a polyethylene insert, which is used as a mobile bearing surface; sometimes we can find the fourth component which replaces the patella and is made of polyethylene.

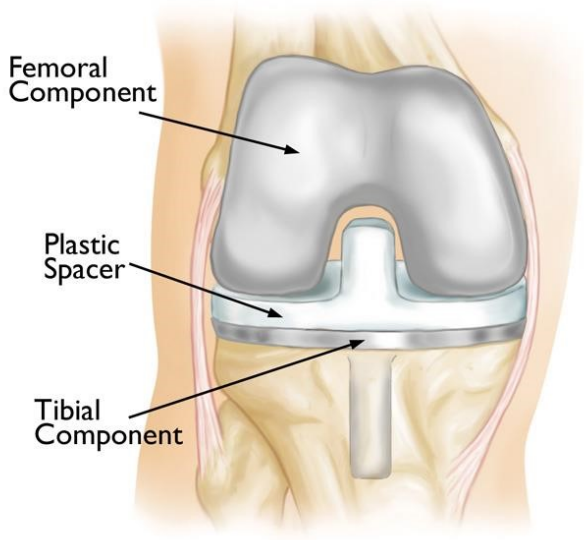

Figure 1.7: Main component of a knee prosthesis: the femoral component that covers the condyles' surface; the tibial component with the stem; and the polyethylene insert between them. [22]

The femoral component is the largest and has a curved part that replaces the damaged condyles, while the tibial component has a flat shape, over which is joined the plastic spacer, and a stem that is inserted into the bone. The polyethylene insert fits between the femoral and the tibial components and provides a smooth surface to allow physiological flexion and extension movements.
The design and materials of the prostheses must satisfy important requirements to achieve the main purpose: restore a physiological movement of the joint and partially or totally eliminate pain [1]. In Figure 1.8 a radiography of the knee shows the metallic components of the prosthesis.

Many types of prostheses are used in TKA [37] and since the beginning of this surgery, prostheses have seen many changes and evolutions. The main challenge is represented by the difficulty to find the best compromise between stability and allowed movements. Furthermore, controversy exists regarding which prostheses are the most appropriate for individual surgeons and specific patients.
In summary, total knee prostheses can be classified according to:

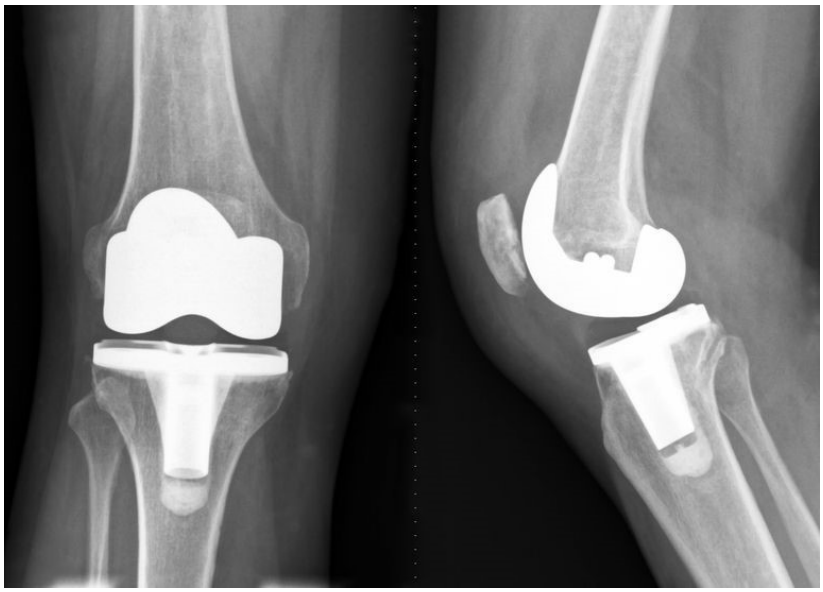

Figure 1.8: Radiography of a total knee prosthesis.

1. The degree of freedom of the mechanical constraint

   a. Unconstrained prosthesis: the posterior cruciate ligament (PCL) is kept and it will act as a constraint to ensure the stability of the system. In this case, the femoral prosthetic component will have a central area that will welcome the ligament;

   b. Semi-constrained prosthesis: the PCL is sacrificed and will be replaced by a particular mechanism, which has the purpose of stabilizing the joint, in the anteroposterior direction;

   c. Constrained prosthesis: it is characterized by a central pin that blocks the tibial component to the femoral. Nowadays, these models are mostly abandoned due to the high rate of postoperative complications caused by excessive rigidity of the implant.

2. The tibial insert, that can be:

   a. Mobile: the polyethylene tibial insert can slide. This mechanism can be reached with a pin that is inserted in the tibial component. This movement allows automatic alignment of the prosthesis on the different planes, trying to reproduce the original anatomical features of the knee;

   b. Fixed: the joint insert is fixed and integral with the underlying tibial component.

The history of prostheses evolution follows a repetitive course of development and failure: what is the best solution remains a topic of discussion among both researchers and surgeons.

Chapter 2

Total Knee Replacement Surgery

Knee replacement surgery could be more accurately defined as a "lining" of the knee since only the surface of the bones will be replaced. The surgery lasts about two hours and requires the resection of the proximal part of the tibia and the distal part of the femur, before the implantation of the prostheses.
From a mathematical point of view, performing a knee joint replacement is, therefore, a rather complex optimization problem in which the best compromise must be found in order to allow a full range of motion with perfect mobility/stability in both the femoro-patellar as well as the tibio-femoral joint. [39]
During the surgery, it is important to maintain the right alignment of the knee, to avoid early failure of the intervention. Proper alignment of the knee is characterized by two independent conditions: the prosthetic knee must be centred on the mechanical axis of the lower extremity and the joint line should be oriented in a proper way. The objective of prosthetic replacement is to distribute contact stresses across the artificial joint as symmetrically as possible, avoiding overloading of one compartment. This philosophy can require altering an individual's pre-arthritic anatomy.
Optimizing alignment in TKA requires an understanding of the chosen instrumentation system. Computer-assisted knee navigation is available for helping the surgeon to achieve more accurate positioning of jigs, to correctly establish femoral component rotation, to have instantaneous feedback on overall alignment and to prevent implantation of bad-positioned components. Component malposition can, in fact, cause pain, limited range of motion instability, polyethylene wear, and loosening of the implant.
Instrumentation systems have been grouped, referring to a classical alignment or anatomical alignment. In the classical variety, which is the most common, the main goal is to establish a joint line perpendicular to the reconstructed mechanical axis. In this way, the tibial cut is perpendicular to the overall tibial shaft axis (as shown in Figure 2.1).

Since the distal femoral cut is perpendicular to the femoral portion of the mechanical axis, it is oriented at an angle of approximately 6° relative to the femoral shaft axis. The anatomical alignment establishes a femoral component rotation directing the rotation of the posterior aspects of the femoral component to lie parallel to the original position of

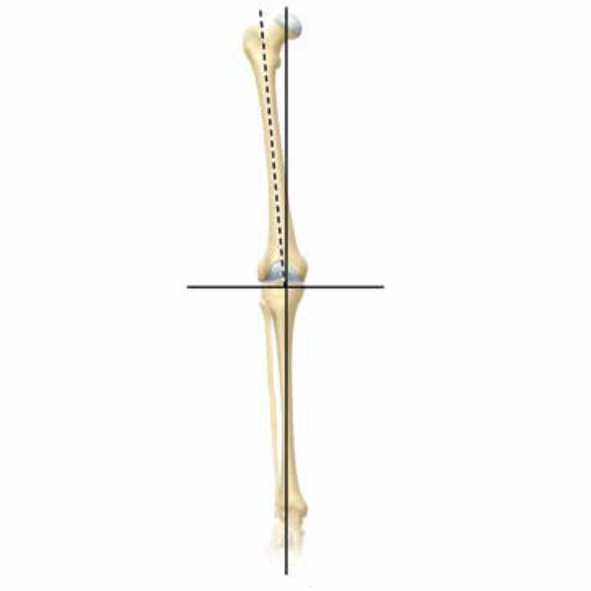

Figure 2.1: Pre-operative planning. The tibial cut is perpendicular to the mechanical axis. Image taken from Vanguard® Complete Knee System: Surgical Technique.

the patient's posterior condyles. This leads to an angle of 3° valgus.

The proximal tibial osteotomy is usually performed 10 mm below the least compromised articular cartilage. A perpendicular tibial cut establishes proper limb alignment with reference to the distal femoral cut.

2.1 Computer-Assisted Surgery

To improve the alignment and minimize situations of gross malalignment, a system for computer-assisted surgery (CAS) for TKA was developed. It has been recognized, in fact, that an accurate reconstruction of leg alignment offers the best opportunity for achieving good long-term results in TKA.
CAS and robotics have been introduced many years ago for joint replacement (hip and knee) with the aim to improve the accuracy in prosthesis components alignment. The technology was appealing but the learning curve of the orthopaedic surgeons was quite steep. CAS introduced more costs, more materials to be sterilized and longer time for the surgeon in performing joint replacement, meaning an increasing time of surgery and increased hospital costs.
The most important advantage of using CAS technology is the understanding of the mistakes that can be faced during surgery. Information such as optimal resection planes (level and inclinations of osteotomy planes), component size selection and targeted limb alignment is displayed to the surgeon. In general, surgical navigation systems are meant to enhance the final positioning of the implant (accuracy), as well as the visibility in inaccessible areas (security), and the prediction of the effects of the surgical actions (control).

CAS can be defined as a surgical method, based on IT systems, which denotes a large group of applications that involve the use of the computer in order to make surgical procedures in the orthopaedic field less invasive, more effective, safe and reliable achieved throughout the process of digital images. These techniques can assist the surgeon in the pre-operative phase (planning), intra-operative (providing real-time information) and in the post-operative phase (evaluation). This basic information is represented as a set of remarkable points and axes that describe the main features of the anatomy and provide the surgeon with the fundamental references for carrying out the surgery. After the first phase of registration, the system can propose a planning of the intervention in terms of positioning and measures of the prostheses, which the surgeon can both reproduce on the patient and modify, thus obtaining a measure of the effects of the modifications made. Navigation systems for TKA are thus devices that monitor the position of the surgical instruments with respect to the patient's anatomy and surgical references of interest reconstructed from anatomical landmarks without increasing the invasiveness of the manoeuvres. Usually, the estimation of the spatial position of 3-D objects to be monitored is done with stereoscopic systems, some of which use infrared light and markers.
There are different types of navigation systems:

- Image-based or imageless systems: in the first case they use radiographic images pre-operative, from Computed Tomography (CT) or Magnetic Resonance Imaging (MRI) and integrating them with manual acquisitions. In the second case, they do not use CT images or MRI neither pre- nor intra-operative. For both of them, it is necessary a registration phase of the intraoperative anatomy, obtained with detectors attached to the bone segments and a probe for identification anatomical landmarks of interest;

- Open or closed systems: depending on whether they can be used on various prosthetic models or not.

The components of a navigation system are:

- Workstation: consisting of a control unit, a monitor for the doctor to see graphics and numbers by the and a camera system with a specific nominal accuracy;

- Trackers: implanted in the bone segments, they have spherical markers (active or passive, depending on the presence of LEDs or retroreflective materials, respectively) and their movement is tracked by the cameras.

- Probe: that acquires points on the surfaces, to make a spatial and morphological registration of the bone;

- Surgical instruments: to perform the intervention. They can be coupled with the probe.

The cameras, the stars, and the probe have their own Reference System (RS) to define the position and orientation of the bone segments in the three-dimensional space.

The infrared camera is located at the side of the operating room table and it is used by this system to localize emitters placed at specific locations on the patient. The tracking markers are in the distal femur and proximal tibial bony.
The pointer serves to digitise the clouds of points on the surfaces, for spatial registration, bone morphing, and other geometrical calculations. Given all the defined points, the tibiofemoral and mechanical axes can be determined before any bone cuts have been made. Additionally, this navigation system can identify intraoperatively the real-time relative position of the tibia with respect to the femur.

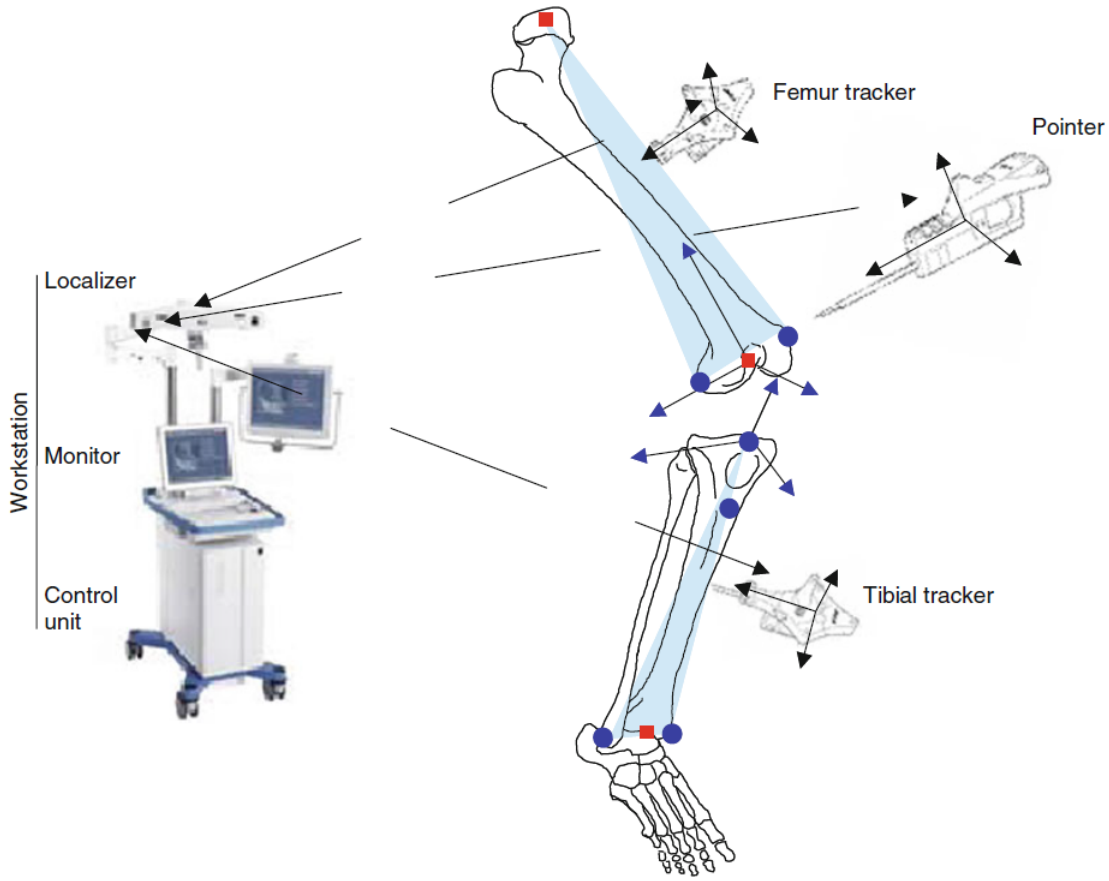

Figure 2.2: Diagram showing the main instruments and references in a knee navigation system. The main workstation is made of the control unit with the computing power, a monitor for control, and graphical restitution to the surgeon and the localiser with the digital cameras to track the trackers' motion. [14]

The main workstation is made of the control unit with the computing power, a monitor for control, and graphical restitution to the surgeon and the localiser with the digital cameras to track motion of the trackers (Figure 2.2).
The software displays online the orientation of the cutting block in comparison to the anatomical references of the bone and the surgeon can fix it with the desired orientation before performing the bony resection. A navigated plate makes it possible to check the actual orientation of the resections in comparison to the expected one.

The resolution, or sensibility, of the system is the smallest change in the quantity that produces a response in the measurement.
Many studies have provided large evidence that implant alignment is significantly improved compared with that achieved by conventional surgery.
Many factors should be taken under control, to prevent the system from leading to an incorrect behaviour: the deterioration of the optoelectronic cameras as well as the instruments, also dependant on the process of sterilisation; the definition of surgical targets according to different surgical goals; the reliance on rigid fixations of trackers on bones and surgical instruments; the requirement of manual definition of axes and calibration of landmarks; the implication of anatomical, functional, and mathematical conventions; the communication with the surgeon through a visual or numerical interface and the monitoring of surgical actions which cannot be controlled. All these processes involve necessarily potential errors, which must be understood and, when it is possible, solved.

2.1.1 Surgical steps

The surgical procedure that the surgeon must carry out, using a navigation system, is made of several steps, briefly described below:

1. *Positioning*: the patient position is chosen so that the doctor has a complete view of the screen and that the cameras can continuously monitor the trackers fixed on femur, tibia, and probe, in a wide variety of movements.

2. *Initial Skin Incision*: the skin incision is centred over the medial one-third of the patella and the length will vary depending on the anatomy, but generally ranges between 10–15 cm.

3. *Deep Exposure*: according to the different approaches, arthrotomy is performed from 1–2 cm above the superior pole of the patella. The fat pad is removed to facilitate exposure and to improve patellar mobility. The medial release is performed at this point.

4. *CAS Application*:

   a. Positioning of the femoral and tibial stars according to the specific surgical technique

   b. Acquisition of the anatomical landmarks through the use of the probe, which allows to create the RS of the navigator (see Appendix B) and to describe the main axes of the limb and the morphology of the patient.

   c. Planning of the cuts

5. *Tibial and femoral Resection*: it is based on the rules of the surgical technique to obtain optimal positioning of the prosthesis.

6. *Tibial Sizing*: After a flat tibial resection has been made, the appropriate tibial base plate is selected so that it provides the best tibial coverage both anteroposteriorly and mediolaterally.

7. *Tibial and Femoral Implant Insertion*

2.1.2 BLU-IGS® system

BLU-IGS® is the first of the computer-assisted tool designed at Orthokey Italia s.r.l. and it was developed in cooperation with Rizzoli Institute in Italy. BLU-IGS® allows us to perform surgery keeping all the key phases under control: in a few steps, it is possible to plan and control optimal resections, based on anatomy or considering also joint stability and range of motion. The acquisition of the anatomical landmarks with the probe creates the RS and is used to describe the main axes of the limb and the morphology of the patient. The system allows both to acquire a specific point and an entire area of interest, using the STREAM mode, collecting a maximum of 80 points. In this case, the surgeon starts and ends the acquisition through the buttons on a pedal board, passing the probe over the area to be acquired during the registration phase. The system accuracy is 0,5 mm.
The navigated procedure starts with the definition of the femoral mechanical axes. The most proximal point is the centre of the head of the femur which is obtained through a rotary movement of the femur itself and the most distal point is the intercondylar notch. The centre of the femoral head is calculated using an iterative Gaussian algorithm to solve the non-linear system and it assumes that the femoral head is spherical. The method of least squares is used to find the best-fit sphere given the data points collected by rotating the femur into the acetabulum. Finally, the centre point is transformed into the femoral reference frame. The tibial axis is defined as the axis passing between the centre of the tibial plates and the midpoint of the medial and lateral malleolar prominences. In the same way, other points are acquired: the tibial tuberosity and the shaft, which is the point on the femur above the upper edge of the patellofemoral joint. For the acquisition of the lateral and medial tibial plates and the distal and posterior condyles (medial and lateral), the pointer is used in STREAM mode. All the acquired points are saved and subsequently processed by the software which identifies a representative point for each zone and uses them for the reconstruction of the patient-specific bone morphology, using an approximation with spline curves. This step is essential for the planning of the surgical cuts.
After the acquisition of all the points, the anatomical reference system is constructed (see Appendix B for the positioning of objects in 3-dimensional space):

- Femoral RS:
  - Origin: intercondylar notch;
  - x-axis, coinciding with the medium-lateral (ML) axis: positive laterally for both the left and right limbs;

  - y-axis, coinciding with the anteroposterior axis (AP): positive posteriorly for both limbs;
  - z-axis, coinciding with the mechanical axis: positive proximally for the left and distally for the right limbs.

- Tibial RS:
  - Origin: tibial spine;
  - x-axis, coinciding with the medium-lateral (ML) axis: positive laterally for the limb left and medially for the right;
  - y-axis, coinciding with the anteroposterior (AP) axis: positive posteriorly for both limbs;
  - z-axis, coinciding with the mechanical axis: positive proximally for the left limb and distally for the right limb.

After the acquisition phase, the system moves on to the planning of the tibial and femoral cut to obtain an optimal positioning of the prosthesis. Figure 2.3 shows the interface that is represented during the positioning of the cutting guide on the tibia: the surgeon must overlap the yellow (real) line to the green (planned) line. In the automatic planning, the tibial cutting plan must be perpendicular to the tibial mechanical axis in the front view, the slope (inclination of the tibial plateau) must coincide with that acquired, or with the default one, and the proximal-distal positioning must depend on the plate chosen as a reference by the surgeon. He performs tibial resection and, observing the interface, he must try to respect the planned cutting plan by making it coincide with the associated one to the cutting guide. If the doctor is satisfied, the resection is performed.

As regards the femoral planning, the internal-external rotation of the femoral component with respect to the Posterior condyle axis is first evaluated and then the thickness of the cut is evaluated considering the flexion and extension ligament balance. The surgeon then optimizes the cut to obtain the desired surgical result. At this point, he proceeds with the femoral resection phase both in the distal and anterior part. The cut is performed as for the tibial resection. Both in the pre- and post-operative phase, a kinematic analysis can be carried out by observing in extension and in flexion, at various angles, the degrees of varus or valgus limb. This evaluation provides an indication of the level of stability and alignment obtained.

All these procedures require a particular attention of the surgeon, which must perform a long-lasting intervention and keep under control many parameters for the success of the implantation. Sometimes, this can lead to wrong acquisitions, due to drops in attention or small uncontrolled movements of the surgeon. This situation can lead to mistaken conclusions by the software and result in bad planned cut. One of the situations that could happen, for example, is that the surgeon starts the registration of the surface before the probe is located on the bone, or accidentally pick off the probe during the acquisition, obtaining some outliers within the acquired points. The critical surfaces are the condyles

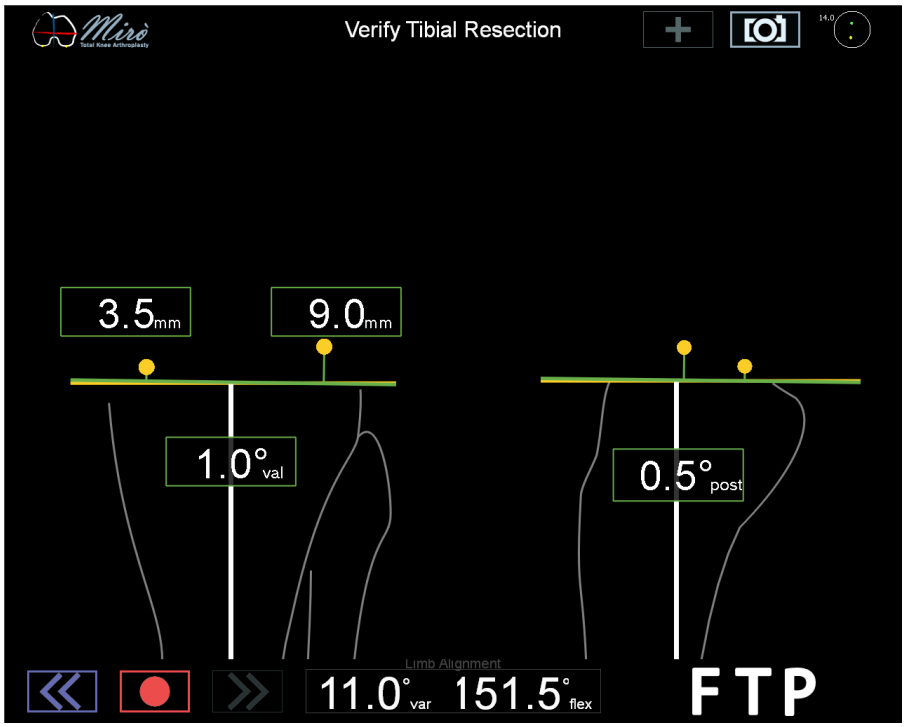

Figure 2.3: BLU-IGS® interface during the checking of the tibial cut.

and the tibial plateau. During the acquisition of these points, the surgeon must deal with curved and damaged portions of the bone that could be covered with blood and disturbed by adjacent tissues. From this acquisition, reference points are taken. On the femur surface, the most distal point on the distal condyle and the most posterior point on the posterior condyle are registered to deduct the prosthesis size and to plan the femoral cuts. On the tibial surface, the most distal point on the tibial plateau is registered to orient the cut in order to leave the right room for the prosthesis insert.
The aim of this thesis is to find a way to identify and delete the points acquired which are not on the surface of the bone, considering that each patient's bone has its own shape and morphological characteristic, which must be taken into account.

Chapter 3

Bone's Shape Reconstruction: State-of-the-art

The reconstruction of the bone's morphology has been widely investigated in the literature, in order to analyse the complex shape of the knee, understand the possible causes of pain, and propose optimal solutions for prosthesis or other treatments. In this chapter, the studies conducted on the bones' reconstruction are presented, with a focus on the mathematical models to reconstruct the shape of the bone and the methods to detect outliers from surface registrations. These works constitute the starting point for the development of a solution to our purpose.

3.1 Mathematical Models for bone's surfaces

The surface we must represent through the points cloud acquired with BLU-IGS® is relative to the femur condyles and the tibial emiplateaux. Finding the best fitting model is not trivial, and we must face the possibility to represent the surfaces with bi-dimensional (2-D) or tri-dimensional (3-D) models.
The femur surface morphology has been studied in a 2-D sense in many works. Van den Heever [46], aimed to reconstruct the human femoral condyles with a mathematical function in both the sagittal and transverse planes (see Figure 3.1). In another study [29], the shape of the distal femur has been investigated, considering the condyle's distal and posterior portion as a whole, and fitting them with a circle (Figure 3.2).

In the 3-D space, dealing with data fitting problem means finding a mathematical function $f(x, y)$, able to reproduce z at best (see Figure 3.3 and 3.4).

The 3-D reconstruction gives information not appreciable with the 2-D model, but the complexity of the problem must be taken into account: in our case, the reconstruction of the bone's surface must not slow down the procedure of the acquisition during the surgery.

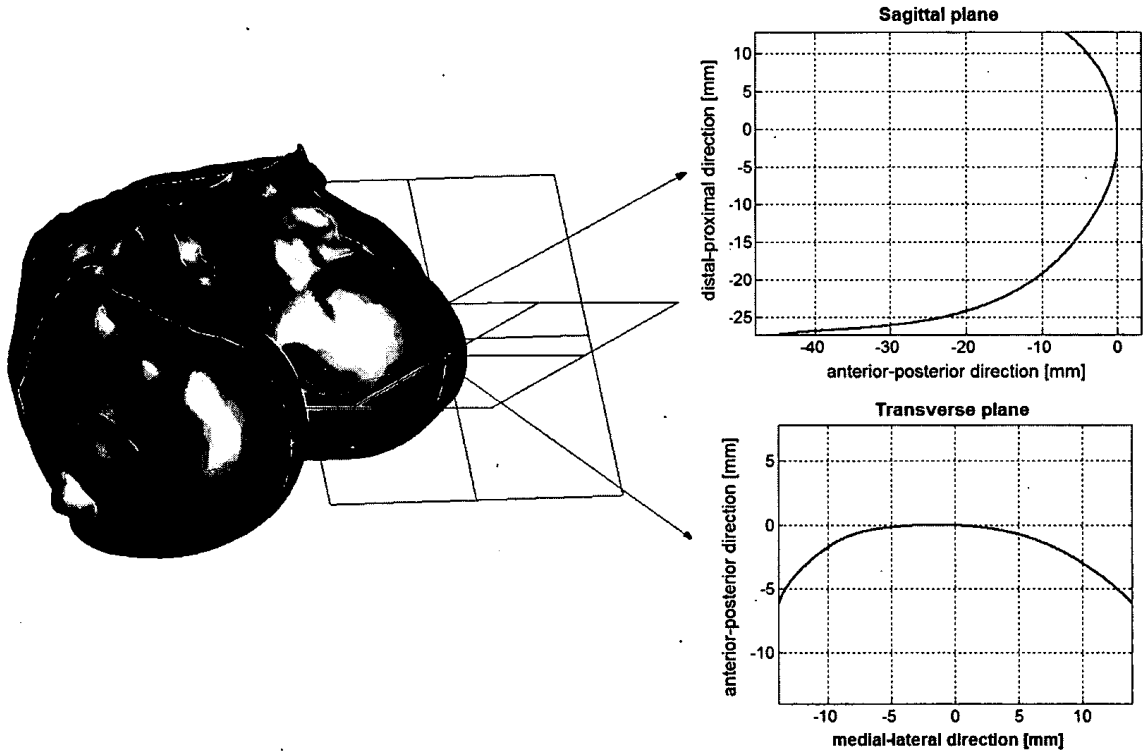

Figure 3.1: Intersection planes through the lateral condyle of a distal femur with the corresponding sagittal and transverse intersection curves. [46]

3.1.1 2-D Mathematical model

Many studies have been carried out to determine the shape and geometry of the femoral condyles, while very few quantitative data have been published regarding the asymmetric geometry of the tibial plateau.
The main information relative to the tibial geometry is focused on the characteristic posterior slope of the tibial plateau (with the anterior elevation that is higher than the posterior) [19]. Tibial slope is defined as the angle between the orthogonal line passing through the centre of the tibial diaphysis and the line representing the posterior inclination of the tibial plateau. This slope is a 2-D approximation of a complex, asymmetric, and three-dimensional surface and it does not consider the differences in the medial and lateral aspects of the tibia.
The femoral condyle morphology was examined in [6], where the aim was to mathematically approximate the shape of the femoral articulating line and compare, from the side view knee X-ray, the radiuses of condylar curves between and within males and females, using a mathematical equation. The profile shape of the femoral condyles, between a flexion range 0°-90° of the contact point, is commonly described as an ellipsoid curve. The radiuses of the anterior part are longer than the radiuses of the posterior part and the connecting line of the end of all the radiuses is letter "J" shaped (see Figure 3.5).

Different surfaces have been chosen to mimic knee joint surfaces: cones, arches, hemi-

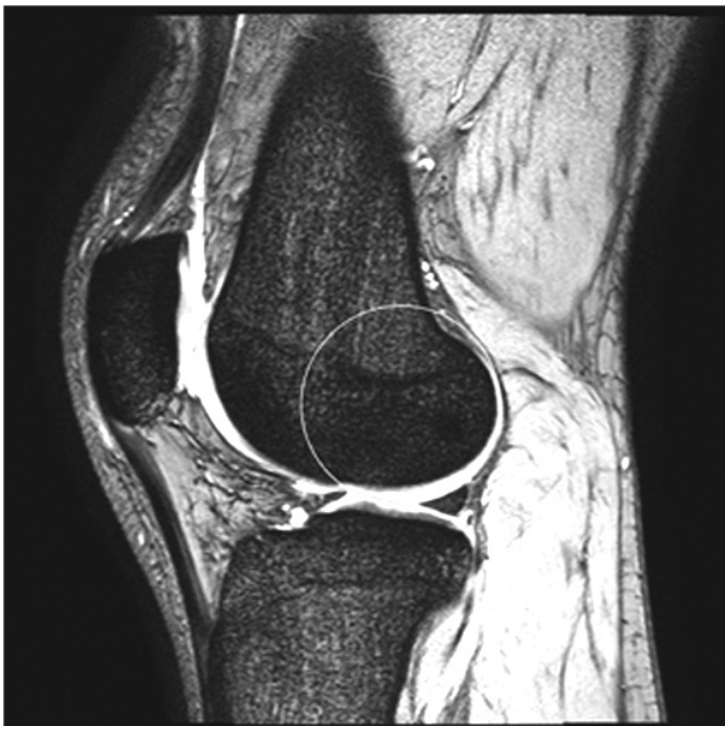

Figure 3.2: Parasagittal plane MRI scans through the lateral condyle with a circle fitted to the posterior and inferior facets.[29]

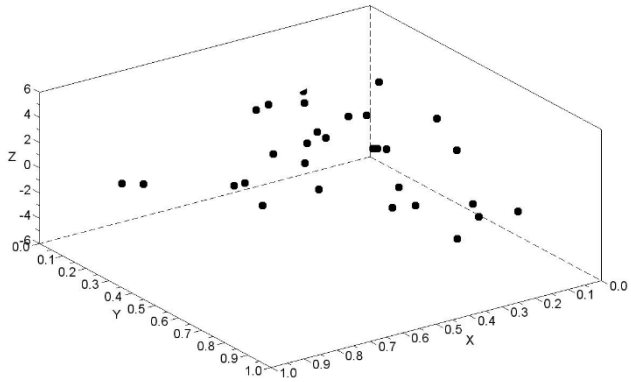

Figure 3.3: 3-D plot of a data set involved in model fitting problem with 30 couples of values (x and y, belonging to the interval [0, 1]). *https://www.scilab.org/tutorials/surface-fitting*

spheres or polynomial approximation. All those studies on condylar surfaces and almost all the employed mathematical models are based on 2-D (planar) description. In [6], researchers focused on the radiuses, approximating the profile with 2-D mathematical models, by analysing twenty femoral condyles (ten males and ten females). The results of this study lead to the following statements: the anterior distal part (fourth quadrant) and the posterior proximal part (second quadrant) are quarters of a circle, with diameters approximately 4 and 2 cm diameters, respectively; the posterior distal part (third quadrant), that articulates with the tibia in a range of flexion from 0° up to 90°, is quarter of

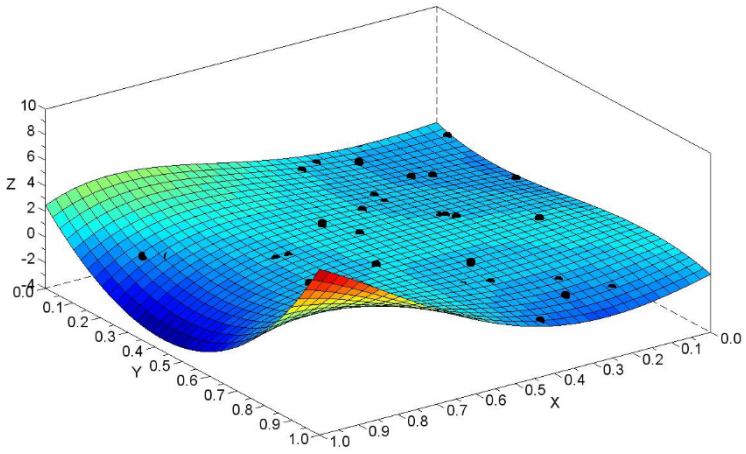

Figure 3.4: Dataset points (black dots) and fitting 3-D model, using Scilab software. It can be noticed that the resulting surface, even if it approximates the data, does not pass through the points, being not interpolating. *https://www.scilab.org/tutorials/surface-fitting*

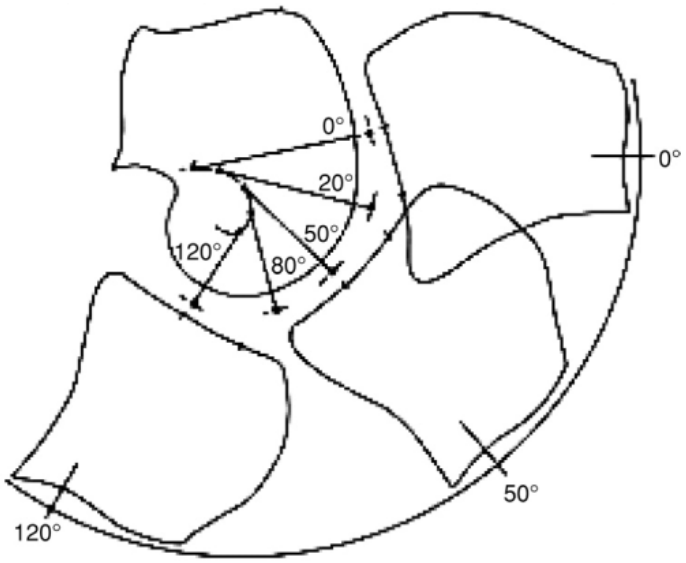

Figure 3.5: Sagittal view of the knee with the representation of the changes in radiuses and their connecting line. [6]

ellipsoidal. Results are showed in Figure 3.6.

By analysing the shape of the medial and lateral condylar curves, it can be noticed that radiuses reduce and that the anterior part of femoral condyles results less curved compared to the posterior part. For the medial compartment, the mean radius goes from 45 mm to 17 mm (from 0° flexion contact point to 90°), while the lateral one decreases from 31 mm to 14 mm.

The reconstruction of the best mathematical model to describe the articulating profile geometries of the knee was the object of another study, conducted by van den Heever [46]. In this study, the sagittal and transverse profiles were described using four mathematical

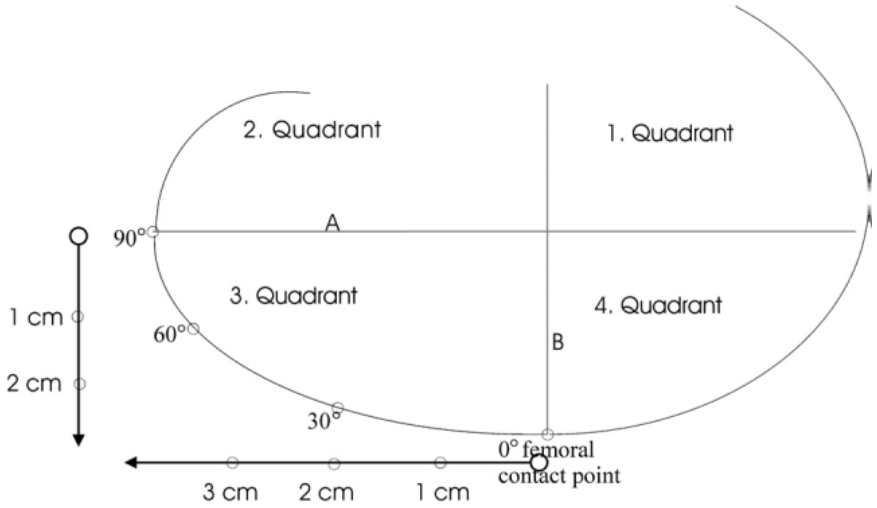

Figure 3.6: Femoral condyle contours in sagittal plane divided in quarters. [6]

equations: single radius, dual-radius, polynomial, and B-spline.

- Single Radius Model: a single radius arc was used to reconstruct the condyles in the sagittal and transverse planes. The radius and the centre of the arc were defined by a minimization of the sum squared radial deviations.
- Dual Radius Model: to reconstruct the sagittal curve a dual radius model was used by dividing the condyles into two parts: the distal portion, below the most posterior point, and the proximal portion, above that point. Then, a single radius arc was fitted to each portion.
- Polynomial Model: by dividing the condyles into the distal and proximal part, two polynomials were used to represent each part. A second-order polynomial was used for the proximal portion, while a fourth polynomial was used for the distal one.

$$f = a_0 x^n + a_1 x^{n-1} + \ldots + a_{n-1} x + a_n \tag{3.1}$$

- B-spline Model: non-uniform rational B-splines (NURBS) were used to reconstruct the femoral condyles, due to their flexibility to design a large variety of shapes. A NURBS curve is defined by its order, a set of weighted (w_i) control points (P_i) and a knot vector (u). In the following equation, $N_{i,k}$ represents the normalized B-spline basis function of degree k.

$$C(u) = \frac{\sum_{i=0}^{n} w_i P_i N_{i,k}(u)}{\sum_{i=0}^{n} w_i N_{i,k}(u)} \tag{3.2}$$

To compare these models, the difference between each point in the data set and the fitted curve was calculated. The results can be seen in Figure 3.7, where a medial condyle was used as representative. The B-spline model fits the original data most accurately, with a mean maximum error of 0.15 mm and 0.6 mm for the medial and lateral condyles,

respectively. The polynomial model showed a mean maximum error of 1.75 mm for the medial condyle and 1.79 mm for the lateral condyle. The dual radius model presents the largest mean maximum errors and the single radius model showed the largest mean RMS errors.

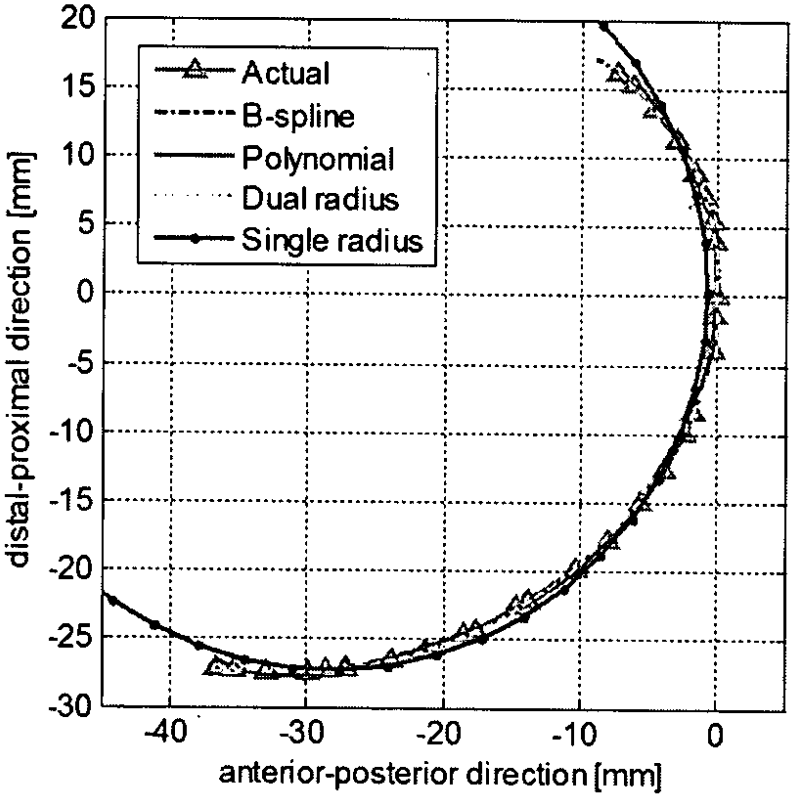

Figure 3.7: Fitted models on the medial condyle in the sagittal plane. [46]

The NURBS curve describes precisely the shape of the femoral condyles' profile. A spline curve is a composite curve, constructed by joining adjacent segments of polynomial curves with appropriate continuity, generally C^2, so that the last point of the first curve coincides with the first point of the second curve and in these two points there is the same tangent (first derivative) and curvature (second derivative). The B-splines join together several Bézier curves and are mainly divided into three types:

- Uniform B-splines: parameterized on intervals [0,1]
- Non-uniform B-splines: parameterized at different intervals
- Rational Non-uniform B-splines, called NURBS: defined as rational polynomial curves

Many computer software allow constructing a NURBS curve, by setting the curve degree and choosing either the interpolation points or the control points (Figures 3.8 and 3.9).

Figure 3.8: NURBS curve created by setting interpolation points.

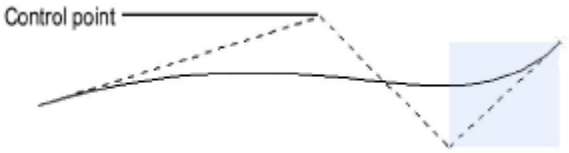

Figure 3.9: NURBS curve created by setting control points.

3.1.2 3-D Mathematical Model

Chen et al. [10] developed a parameterization method to reconstruct three-dimensional volumes of the entire femur, through the study of one hundred CT images of right healthy femurs. To level out the ethnic and regional differences, a statistical shape analysis was used to create an average model, that described the entire population. Through the definition of a set of feature parameters, a feature surface morphing was performed over the head, neck, trochanter, shaft, and condyles.

The polynomial fitting in three-dimensions is probably one of the simplest and most used data fitting techniques. The main idea is that the system (data set) can be adequately modelled by a mathematical function $p(x, y)$, expressed as:

$$p(x, y) = C_0 + C_1 x + C_2 y + C_3 xy + C_4 x^2 + C_5 y^2 + \dots \tag{3.3}$$

where coefficients represent the free parameters of the model. Polynomial coefficients are determined by imposing the interpolation condition of $p(x, y)$ in each point of the data set (x_i, y_i), thus obtaining a linear equation system, as follows:

$$\begin{bmatrix} 1 & x_1 & {x_1}^2 & \dots & {x_1}^n \\ 1 & x_2 & {x_2}^2 & & {x_2}^n \\ & \vdots & & \ddots & \vdots \\ 1 & x_p & {x_p}^2 & \dots & {x_p}^n \end{bmatrix} \begin{bmatrix} C_0 \\ C_1 \\ \vdots \\ C_n \end{bmatrix} = \begin{bmatrix} y_1 \\ y_2 \\ \vdots \\ y_n \end{bmatrix} \tag{3.4}$$

The number of points to be fitted is usually larger than the number of the coefficient of the polynomial, thus leading to an over-determinated system which will be solved in a least-square sense. The resulting polynomial, as for the 2-D model, does not interpolate exactly all the data, but it fits the data.

3.2 Outliers Detection Methods

In surgical navigation systems, spatial errors may be caused by several factors: most of them depends only on the system itself, such as position measurements, visibility, references, calculations, and conventions. Other errors depend on the surgeon's ability [14], such as landmarking and execution process. The latter has been investigated for several systems and can be certainly limited by a more complete consciousness of the procedures and the most common errors. Navigation systems will likely be enhanced by a more careful measure and analysis of all these errors, and by the development of compensation algorithms, which are meant to lead to the right results even if the process of registration is affected by inaccuracies.

3.2.1 Sources of errors

Registration [16] is the central operation required for surgical guidance and if it is not done well, then a guidance system may be not only useless but also dangerous. Registration could be defined as a geometrical transformation that aligns one view of an object with another, where a "view" can be an image, such as CT or MR, but it can also be the physical object itself. This alignment is done through a mathematical function that maps each point in the space of one view onto the corresponding point in the other, and it is the accuracy of this correspondence that determines the value of the guidance.
Modern surgery depends significantly on medical equipment, which contributes to the quality of the surgical intervention and allows it to be raised to a level previously not achievable. Many navigation systems have registration methods that are enhanced with algorithms that process the data to produce optimal (but not ideal) registration. Most of these algorithms have the purpose to limit the errors due to the incorrect transformation of the system, including the identification error of the external features used for registration, geometrical distortion in the preoperative images, and tracking error of the surgical instruments. The final aim is to reach an ideal transformation, which means, for example, that when a depicted probe touches an anatomical target point on the computer screen, the actual probe will be touching the actual anatomical target on the patient. If the optimal transformation is not ideal, however, then the actual probe will be displaced some distance from the actual target. This distance is called "target registration error" (TRE), and it is the commonly accepted true measure of the accuracy of a registration process.
If the optimal transformation produced by a registration process is specified by T, then a target point p in the image will be mapped into a physical point p':

$$p' = T(p) \tag{3.5}$$

If the ideal transformation maps p to q, then the error vector, $TRE(p)$ is equal to $p' - q$. $TRE(p)$ has three components, in the x, y, and z directions, but we can also identify with $TRE(p)$ the size of the error at that point, that is equal to the length of the displacement

vector:

$$TRE(p) = |p - q| \tag{3.6}$$

A registration with high accuracy is one with low TRE. Reaching this purpose, enables surgeons to perform a simulation of the surgical intervention and to determine the most effective surgical approach.
Strategies to detect and possibly delete the causes of an increased TRE have been developed since the beginning of CAS [16], in many fields of surgery, including neurosurgery [3], but also to detect anatomical landmarks in cranio-maxillofacial surgery [2].
It is important to distinguish three categories between these systems at the levels of data perception: CT-less systems using Bone Morphing; CT-less systems using landmarks; and CT-based systems.
In 1999 Fleute and Lavallèe applied a statistically-based shape model into a system for computer-assisted anterior cruciate ligament surgery [18], facing the problem of extrapolating very sparse three-dimensional data to obtain a complete surface representation (as described in the following sections). The main goal of this method was to reconstruct the expected surface from a set of given points providing a surface-matching option. Algorithms are included for defining a surface and then, in the operating room, the surgeon touches the surface at multiple points with a probe to determine a set of points on the same surface. An optimal transformation is sought that minimizes the distance between the surface points found in the operating room and the surfaces identified in the image.
This approach could represent a good starting point to develop an algorithm that eliminates the spatial errors due to the surgeon's ability: the idea is that the reconstructed surface of the bone should be matching with the normal shape of the acquired portion. If there are consistent differences between the expected model and the acquired data, some points must be affected by errors.
In this chapter, the main strategies to reach optimal transformations are reviewed, trying to relate this purpose to the objectives of this work. An important factor to be considered is that most of the following algorithms assume the presence of an a-priori image of the specific surface, that could be represented by a CT or MRI image of the patient's bone or by an a-priori knowledge of the bone surface. BLU-IGS® is an imageless system, that uses only intra-operative data obtained with an optical localizer without requiring additional images such as x-rays, CT or MRI (which also means avoiding the high radiation dose and costs associated with such scans). Constructing a patient-specific 3-D surface in imageless-based systems is quite challenging. This is usually done by building a deformable model and adapting the model to the surface of interest related to the patient. By comparing the model and the acquired surface, there should be evidence to state whether the unwanted outliers are present or not within the points cloud.

3.3 Bone Morphing

The literature proposes a large variety of methods to build a surface model from range data. The extrapolation procedure also called Bone Morphing is done via a statistical Principal Component Analysis (PCA, see Appendix C) based shape model. This approach to Bone Morphing based on fitting procedures has the disadvantage that it is computationally expensive and only a small set of shape variations can be considered. Also, non-spatial information such as patient height, weight, and sex cannot be incorporated in these earlier techniques.
3-D morphologic data obtained with the Bone Morphing technique are very useful to visualize (in real-time and in the 3-D space) bone defects, planned surgical cuts, choice of implant size, choice of implant position and rotation with respect to bone cortical surfaces, and distances between bones and components before making any real cut. Any one of these parameters directly affects the implant position during the planning phase.
This approach was chosen by Praxim®, whose surgical image-free system, used for the reconstruction of the ACL, integrates Bone Morphing technology to reconstruct the anatomy of the patient under arthroscopy [32] and to perform TKA [38]. In this system, Bone Morphing is used to compute the accurate morphology of the patient's knee starting from a deformable statistical model, without any use of CT, radiography or fluoroscopy. Several hundred scattered points are acquired by the surgeon, by "painting" the cartilage and bone surface with the probe. These points are matched with the statistical model using a 3-D/3-D registration algorithm. The bone model displayed on the screen is formed in real-time, to adapt to the knee of the patient.
The digitization of the cloud of random points on the bone surface of the patient is achieved using a pointer as shown in Figure 3.10

Figure 3.10: First step of the Bone Morphing procedure: Digitization of a cloud of random points on the bone surfaces of the patient. Source: [38]

Three steps are required to obtain this 3-D statistical shape:

1. Acquisition of n training shapes, consisting of dry human bones (n must be sufficient to represent a good variability of the population). An additional bone was digitized with higher point density, to construct a template model;

2. Definition of a point-to-point correspondence between training shapes, matching each of the n set points to the template (using the process developed by Szeliski and Lavallèe and explained in the following sections);

3. Statistical analysis, to compensate for deviation of any pathologic shape with respect to statistical shapes. The patient-adapted statistical model is deformed locally until it correctly and precisely fits the cloud of points;

This technique is a very robust and accurate process, also because it rejects the results that give an error greater than 1 mm, computed as the root-mean-square (RMS) difference between the model and the set of points digitized by the surgeon. In this case, the user must take new points.

3.3.1 Statistical Shape Models

Statistical shape models are currently used in orthopaedic surgery to allow accurate positioning of prosthetic components through Bone Morphing and to assess the correct post-operative follow up by virtually reconstructing the surgical site. A Statistical Shape Model (SSM) is a collection of similar shapes, called instances, from which a mean shape is extracted. The covariance of the model is used to deform the shape, according to the principal axis of variation, and the balance between the eigenvectors that deform the model is achieved using different weights. Different types of SSMs have been proposed, allowing accurate modeling of shape structure and variation.
Fleute et al. [17] proposed a method to extrapolate a complete surface representation of an anatomical structure starting from a data set of points. The method uses SSM and it was applied to a few points manually digitized on the femoral surface, to improve the performance of an imageless computer-assisted system. The main idea is to construct an ideal model of the femur surface, from an accurate and dense registration of the bone and use it as a template. In addition to the template, a key point is the collection of N sets with corresponding landmarks from training images. These non-organized point sets must be matched with the template mesh in such a way that each vertex of the template mesh is mapped to its anatomically corresponding point on the femur represented by the set of points. Before doing that, each set of points is interpolated using an octree-spline deformation: the method performs a least-squares minimization of the distances between a sparse and unorganized set of points and a dense set of points used to build a 3-D octree-spline distance map (as was previously suggested by Lavallèe and Szeliski [40]). The result of the octree-spline based registration technique is a smooth volumetric transform T that maps each point P of the data space to a point $M = T(P)$ of the model space. Reciprocally, given a point M of the template mesh, an iterative search is performed to find the point $P = T^{-1}(M)$ such that $\|M - T(P)\| < \epsilon$. A more detailed explanation of the octree spline transformation is given below. By this process, each point M_i of the template mesh is assigned to a data point P_i for each data set. At first, all training shapes are matched to the template mesh as described above. After calculating the mean shape,

now all training shapes are matched to this current mean. This process is repeated until convergence occurs. The displacement vectors

$$d_{m_i} = m_i - \bar{m} \tag{3.7}$$

describe the mapping between the mean shape and each of the training objects. At this point, one can apply a Principal Component Analysis (PCA) to the data which results in finding the eigenvectors of the covariance matrix

$$C = \frac{1}{N} \sum_{i=1}^{N} d_{m_i} d_{m_i}^T \tag{3.8}$$

of dimension $3Mx3M$ which can be calculated from the displacement vectors. The mean surface and the t principal modes obtained by PCA constitute the statistically-based shape model. The basic idea of a PCA model consists of separating and quantifying the main variations of shape that occur within a training population of objects. PCA defines a linear transformation that decorrelates the parameter signals. If the parameter signals are highly correlated, then the major variations of shape are described by the first few basis vectors (to better understand how PCA is carried out, see Appendix C).

Kumar et al. [34] proposed a Bone Morphing scheme where they progressively remove shape information associated with the digitized points, from the PCA model. Using statistical shape analysis, shape variability is examined, after the surface information coded by the digitized points is progressively subtracted. This procedure of point selection and variability removal is repeated until a close approximation to the patient anatomy is achieved. The final extrapolated surface represents the most probable surface in the shape space given the digitized landmarks. The 3-D model is hence obtained by deforming the statistical model to match the digitized data.

To recover the whole surface of the object from a new set made of a few sparse data points it is necessary to find simultaneously the rigid transformation (rotation R, translation T) between the data and the model in such a way that the distances between them are minimized. The objective function to be minimized is defined as follows:

$$f = \sum_{i=1}^{D} \min_{1 \leq j \leq M} \|d_i - m_j\|^2 \tag{3.9}$$

where m_j is the transformed set; D the number of data points; and d_i the i^{th} data point.

To minimize f an algorithm is used which combines a simulated annealing technique with the downhill simplex algorithm in order to find a near-global minimum. This requires an initial guess for the rigid-body transformation, which is obtained by rigid points to surface registration, using the Iterative Closest Point (ICP) algorithm.

SSM is also used to reconstruct a 3-D model of the bone surface intraoperatively, using percutaneous ultrasound [8]. CT scans of the femur from a database are aligned to one target CT scan using a non-rigid registration algorithm. The femur surface from the target

scan was then propagated to each of the subjects and used to produce an SSM. In the study, a cadaveric femur not used in the shape model construction was scanned using freehand 3-D ultrasound. The ICP algorithm was used to match points corresponding to the bone surface derived from the ultrasound with the statistical bone surface model. The first five modes of variation of the shape model were used. In this study, results are good in the region of accessible ultrasound scanning and the error occurred most in the femoral neck area.

Pose estimation and shape reconstruction of 3-D bone surfaces was developed by Naka et al. [4] with a new method that combines a 3-D distance-based objective function with automatic edge selection. This approach uses an SSM based on two (or more) calibrated X-ray images taken from different orientations for the reconstruction of a patient-specific femur. The proposed method is based on the optimization of an objective function E that contains both a data fitting term E_{fit} and a shape prior term E_{prior}:

$$E = E_{fit} + \lambda E_{prior} \tag{3.10}$$

where λ is a weighting factor.

The point distribution model is built from N training shapes segmented from CT data. PCA is performed to find the mean shape and the main modes of variation of the aligned shapes. To penalize improbable shapes during optimization, the Mahalanobis distance of the shape to the model mean is utilized as the shape prior to the objective function. The data fit term E_{fit} is a function that has a low value when the current 3-D shape accurately matches the edges in the X-ray images. All optimizations were performed using preconditioned conjugate gradients in a trust region approach and the results show an accuracy of 1.68 mm, which is comparable to methods in recent literature.

3.3.2 Octree Spline Transformations

Szeliski and Lavallèe [40] presented a new method to determine the minimal non-rigid transformation between two 3-D surfaces. This process uses a precomputed distance map represented with an octree spline, whose resolution increases near the surface, to compute distances between the points on the two surfaces, and a second octree spline to compute the deformation function. Many applications can be related to this technique, including model-based segmentation of 3-D medical images.

Given a model object in a coordinate system Refmodel and sensed data in a coordinate system Ref_{model}, the main goal is to estimate the transformation $\mathbf{T}$ parametrized by a vector $\mathbf{p}$ which relates Ref_{sensor} to Ref_{model}. The sensed data are represented as a collection of points $\{\mathbf{q}_i i = 1 \ldots N\}$ and the model surface S is represented arbitrarily. The task is to find the geometric transformation $\mathbf{T}$ such that the transformed coordinates $\mathbf{r}_i = \mathbf{T}(\mathbf{q}_i; \mathbf{p})$ lie on the surface S. The simplest representation for $T(q_i; p)$ is a rigid body transformation which can be parametrized by six degrees of freedom (three for translation and three for rotation). More general classes of transformations are the affine transformation, which can be parametrized with twelve degrees of freedom; the trilinear transformations, which

added another twelve degrees of freedom for a total of twenty-four; the quadratic family of transformation and so on. Increasing the order of the polynomial, a wider range of more flexible deformations is obtained, but this will cause instability. A solution is found by modeling the transformation using a family of volumetric tensor product splines.
The 3-D distance map is a function that gives the minimum distance to S from any point **r** inside a volume V that encloses S. This new kind of distance map gives more detailed information near the surface than far away from it.

3.3.3 Iterative Closest Point

The most popular algorithm for surface matching is called the "Iterative Closest Point" (ICP) algorithm. It is used in the Fleute et al.'s method, but also to match points corresponding to the bone surface derived from other sources (for example, from ultrasound images in [8] or in the automatic landmark detection in spine surface CT images [12]). Although this algorithm is often used, it is developed for the construction of 2-D shapes, and the iterative structure adopted makes the algorithm itself very slow [45]. The ICP algorithm was introduced by Besl and McKay [5] and it is the most widely used surface-based registration method because of its simplicity and guarantee of convergence in the presence of good initial conditions. It requires only a procedure to find the closest point on a geometric entity to a given point and the rate of convergence is rapid during the first few iterations. Given a 3-D "model" shape and a "data" shape, they can be matched through an initial translation and a relatively small set of rotation. The alignment is calculated with a minimization of the distance between the shapes via a mean-square distance metric. The distance from a given point p to a parametric entity E is:

$$d(\mathbf{p}, E) = \min_{\mathbf{r}(\mathbf{u}) \in E} d(\mathbf{p}, \mathbf{r}(\mathbf{u})) \tag{3.11}$$

where $\mathbf{r}(\mathbf{u})$ represents a parametric curve or surface ($\mathbf{u} \in \mathrm{R}^1$ for parametric curves, while $\mathbf{u} \in \mathrm{R}^2$ for parametric surfaces). The point-to-parametric-entity distance problem is treated with Newton's minimization approach when a starting point is available. The scalar objective function that must be minimized is:

$$f(\mathbf{u}) = \|\mathbf{r}(\mathbf{u}) - \mathbf{p}\|^2 \tag{3.12}$$

In the description of the algorithm, a data shape P is moved to be in the best alignment with a model shape X. The data shape must be decomposed into a point set if it is not already in point set form.
The distance metric d between an individual data point p and a model shape X, will be denoted:

$$d(\mathbf{p}, X) = \min_{\mathbf{x} \in X} \|\mathbf{x} - \mathbf{p}\| \tag{3.13}$$

The closest point in X that yields the minimum distance is denoted y such that $d(\mathbf{p}, X) = d(\mathbf{p}, \mathbf{y})$, where $\mathbf{y} \in X$.

Thus, given two corresponding point sets:

$$X = \{x_1, ..., x_n\} \tag{3.14}$$

$$P = \{p_1, ..., p_n\} \tag{3.15}$$

we want to find a translation T and a rotation R that minimizes the sum of the squared error:

$$E(R, t) = \frac{1}{N_p} \sum_{i=1}^{N_p} \|(x_i - Rp_i - t)\|^2 \tag{3.16}$$

Where x_i and p_i are corresponding points. If correct correspondences are not known, it is generally impossible to determine the optimal relative rotation and translation in one step. As its name implies, ICP is an iterative algorithm, that can be stated as follows:

- the point set P with N_p points $\{p_i\}$ from the data shape and the model shape X with N_x points are given
- the iteration is initialized by setting $P_0 = P$ and $k = 0$
- the closest point on the target surface is computed:

  $$y_k = C(P_k, X) \tag{3.17}$$

  where C denotes the closest point operator.
- for all the corresponding points, a rigid transformation from source to target is computed so that it minimizes the root mean square (RMS) distance between the points. The least-square operation is calculated and denotes as:

  $$(\mathbf{q}_k, d_k) = Q(P_0, Y_k) \tag{3.18}$$

  where q denotes the points P after the transformation and d is the mean square point matching error.
- each point is replaced by the transformed one and the steps are repeated iteratively until the change in RMS distance meets a certain stopping criterion

  $$P_{k+1} = \mathbf{q}_k(P_0) \tag{3.19}$$

- the iterations terminate when the change in mean-square error falls below a pre-set threshold $\tau > 0$, specifying the desired precision of the registration: $d_k - d_{k+1} < \tau$

3.3.4 Minimum Description Length

Davies et al. [9] proposed another method to find point correspondences in automatically building statistical shape models from a training set of 3-D surfaces. The Minimum Description Length (MDL) based objective function is used in this case to balance the training errors and generalization ability and to quantize the quality of the point correspondences.

Given a set of shapes and a set of known point correspondences, PCA is computed on the set of shapes, and the computed eigenvalues, $\{\lambda_k\} \mid k = 1, \dots N$, are used to calculate F:

$$F = \sum_{k=1}^{N} L_k = \begin{cases} 1 + \log \frac{\lambda_k}{\lambda_{cut}} & \lambda_k \geq \lambda_{cut} \\ \frac{\lambda_k}{\lambda_{cut}} & otherwise \end{cases} \tag{3.20}$$

λ_{cut} is a parameter that determines the point where we effectively switch between the determinant-type term and the trace-type term. The determinant-type terms measure the volume of the training set after correspondence in shape space, which favors compactness. On the other hand, the trace-type terms measure the similarity of each pair of training shapes after correspondence via Euclidean distance. Thus, λ_{cut} represents the expected noise in the training data. Given the above MDL-based objective function, an efficient method for manipulating point correspondences and an optimization algorithm that minimizes the objective function are required in order to find optimal point correspondences.
Motivated by the fact that MDL criterion pays more attention to global consistency, a recent work carried out at Politecnico di Milano [45] introduced a new constraint that enforced the local shape similarity. The constraint is based on the local linear regularization and enforces that the local shape geometry is similar to the corresponding landmark on different shapes. By combining the standard MDL criterion with this new approach, the objective function enforces the correspondence from both global and local points of view. The algorithm was tested over 24 MRI images and it showed slightly slower computational time, but an improved construction for femur and patella SSM, compared with the original MDL method.
Bone Morphing is an effective method to reconstruct the patient's morphology and it is already used in some of the CAS systems currently available on the market. Despite its robustness, the bibliographic research was not limited to this. Since the definition of the points of interest to define the cutting planes in the BLU-IGS® system is unrelated to any pre-operative scanning of the patient's bone and given the potential high variability between the bones' morphology, other strategies were sought to find a simpler but powerful method that could be applied to the eighty (or less) points digitized during the intervention by the orthopaedic surgeon.

3.3.5 Active Shape Models

Active Shape Models (ASM) method for volumetric segmentation [25] represents a method to detect and handle outliers, used particularly in medical images.
In most of the biomedical imaging applications, data can contain noisy, incomplete or confusing image features and can be affected by the presence of outliers, when a proportion of the generated feature points lie on incorrect boundary positions.
The ASMs are used to define principal shape variations across different individuals and over time from a set of examples based on a point distribution model or used as a deformable template to fit the model. The method is invariant to scaling, rotation, and translation since

it uses the ratio of inter-landmark distances. In ASMs, shapes in 3-D can be represented from a set of landmarks by using a concatenated vector

$$x = (x_1, y_1, z_1, ..., x_i, y_i, z_i, ..., x_n, y_n, z_n)^T \tag{3.21}$$

The main modes of variation are extracted from the training samples by applying the PCA. The method allows the identification of outliers independently of the model fitting procedure. The effect of the outliers on the segmentation accuracy is directly linked to their percentage as well as their extremity. Some example of the impact of the outliers on the ASM search is shown in Figure 3.11.

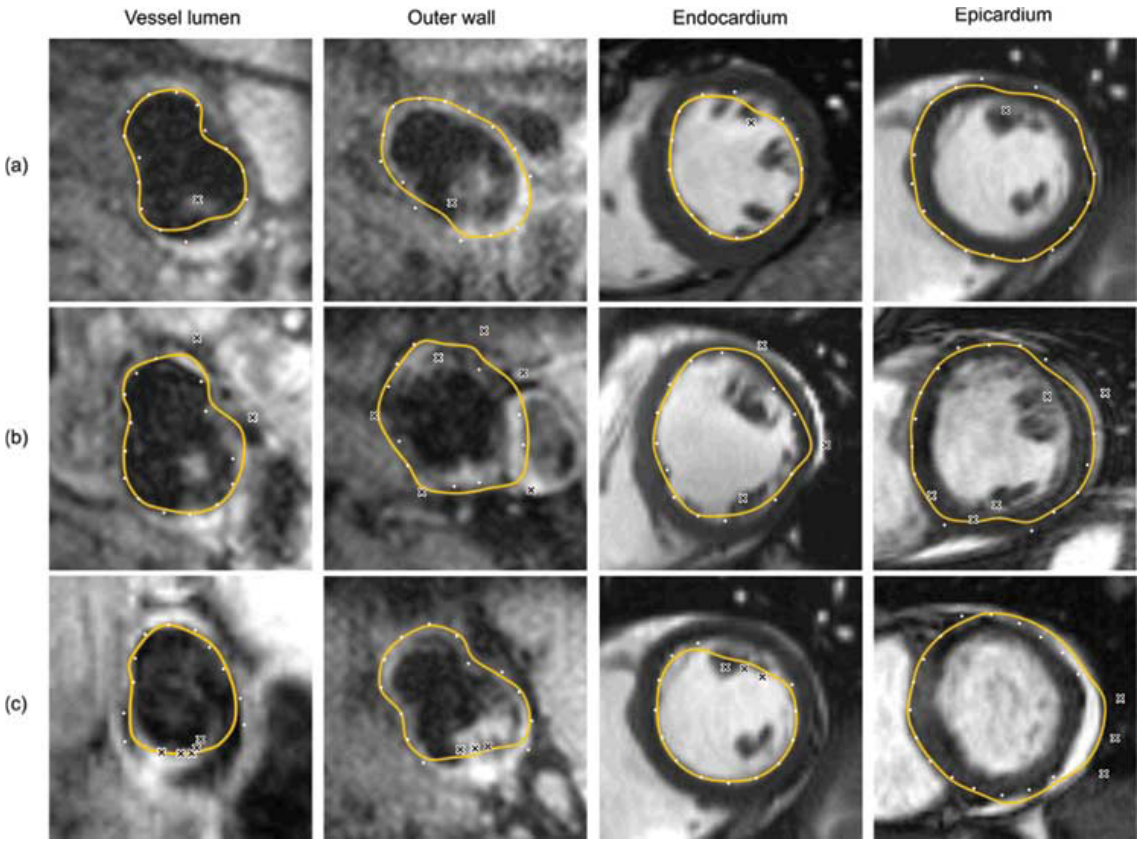

Figure 3.11: 2-D examples illustrating the effect of the outliers (shown as crosses) on the ASM search. (a) shows examples with a single outlier, (b) with multiple outliers, and (c) with clustered outliers. [25]

The ratio of inter-landmark distances is calculated from any triplet of points as follows:

$$r_{ijk} = \frac{\|P_i - P_j\|}{\|P_j - P_k\|} = \frac{d_{ij}}{d_{jk}} \tag{3.22}$$

r_{ijk} represents the relative geometrical configuration of landmark points so that each point can be analyzed with regard to the position of other points in the shape and it also allows a subdivision of the shape into subsets of points, intending to distinguish the subset of erroneous points from the inliers. The idea behind the proposed method is that the outliers

are inconsistent with the corresponding landmark points in the training samples and thus some of the associated ratios are invalid. The first step of the process is, therefore, to find a suitable definition for extreme or invalid ratios, which can be achieved by using tolerance analysis. Statistical tolerance intervals are calculated from the training samples and any ratio found outside of the interval is considered as an extreme value, which indicates the presence of an outlier. By using the tolerance interval, a likelihood measure is calculated for each ratio to detect extreme values due to potential outliers. Typically, this measure is equal to 1 if the ratio is within the tolerance interval and 0 otherwise. The next step is to perform an iterative procedure for outlier detection. At each iteration, the point with the lowest likelihood measure is rejected as an outlier and the likelihood measures of the remaining points are updated by subtracting the contribution of the rejected point. The procedure is repeated until the lowest likelihood measure is close to 1, suggesting all the remaining points are likely to be inliers. The output of this procedure results in two sets of points representing inliers and outliers. Once the outliers are detected, their positions must be adjusted to eliminate their effect on the ASM model fitting.

By analysing all the previous methods in the literature to reconstruct the surface of interest and detect the outliers, it has been found that the best solution for our task, could be represented by another solution: the Random Sample Consensus (RANSAC), a learning technique used to estimate parameters of a model by random sampling of observed data. The simplicity and, at the same time, the accuracy of the RANSAC algorithm have been judged as an optimal solution, avoiding the addition of computational complexity for the software and leading to good results. The algorithm method and the current applications are explained in detail in the next chapter.

Chapter 4

Random Sample Consensus

Many techniques for registration and the problem of correspondence determination use statistics and probabilistic approaches in order to handle datasets with noise, outliers and missing data [41]. Random sample consensus (RANSAC) is a robust algorithm for fitting models affected by many outliers. It follows a hypothesis-and-test paradigm. Given two point-sets P and Q, RANSAC finds the largest subset $P^{'} \subset P$ such that the error between $T(P^{'})$ and Q is less than some predefined threshold, where T is a rigid transformation.
It was firstly introduced by Fischler and Bolles [15] in 1987 as a paradigm for fitting models to experimental data, with applications to image analysis. Interpretation of sensed data in terms of a set of predefined models involves two problems: finding the best match between the data and one of the available models and the problem of computing the best values for the free parameters of the selected model. These two problems are correlated: a solution to the parameter estimation problem is often required to solve the classification problem. The RANSAC procedure is opposite to that of conventional smoothing techniques: rather than using as much of the data as possible to obtain an initial solution and then attempting to eliminate the invalid data points, RANSAC uses the smallest feasible initial data set and enlarges it with consistent data when appropriate. The Fischler and Bolles statement is as follows: [15]

"Given a model that requires a minimum of n data points to instantiate its free parameters, and a set of data points P such that the number of points in P is greater than n, randomly select a subset S_1 of n data points from P and instantiate the model. Use the instantiated model M_1 to determine the subset $S_1{}^*$ of points in P that are within some error tolerance of M_1. The set $S_1{}^*$ is called the consensus set of S_1.
If the dimension of S_1 is greater than some threshold t, which is a function of the estimate of the number of gross errors in P, use $S_1{}^*$ to compute (possibly using least squares) a new model $M_1{}^*$.
If the dimension of S_1 is less than t, randomly select a new subset S_2 and repeat the above process. If, after some predetermined number of trials, no consensus set with t or more members has been found, either solve the model with the largest consensus set found, or

terminate in failure."

4.1 Medical Applications

Many applications of the RANSAC algorithm applied to medical purposes can be found in the literature. Some of them are summarized below:

- Surgical Tool Localization in 3-D Ultrasound Images: Uherčik et al. [44] proposed a method to localize thin surgical tools such as needles and electrodes, inserted into biological tissue, in 3-D ultrasound images. The method performs model fitting using random sample consensus for robust localization of the instruments and the determination of their precise position. In this case, the input of the RANSAC procedure is a set of thresholded voxels and a classification function. The RANSAC outputs are the curve parameters and a corresponding set of points consistent with this model.

- Determination of an accurate venous tree from CT angiography for preoperative planning and intraoperative navigation in hepatic surgery: Yan Z. et al. [49] used RANSAC for modeling the vessel intersection and to conduct the venous tree separation. When performing tumor resection, relative Residual Liver Volume (RLV) must be kept at a certain level and the surgeon must maintain enough blood supply from both hepatic and portal venous systems. To do so, detailed information from both veins are required. Furthermore, during the preoperative path planning for tumor ablation, doctors need to know the positions of nearby vessels, especially the locations of venous vessels, in order to avoid the burning of these vessels, which may cause haemorrhage.

- Detecting and labeling the planar surface generated by the cutting saw in bone tumor resection: this surface area labeling is fundamental to track the path that the cutting saw took during the surgery and compare it to the planned cutting plane. An algorithm presented by Milano et al. [28] compared the 3-D reconstruction of the surgical specimen CT scan against the 3-D reconstruction of the preoperative patient CT scan, and the cutting plane defined during surgical planning. In this method, the RANSAC algorithm was used to distinguish the points that belong to the computed cutting surface from the ones that do not. The application of the algorithm has the purpose to estimate the parameters of the ideal plane described by the cutting saw, returning the largest inlier set of points found.

- Analyze the shape of the arteries localized from ultrasound images: to precisely define the location of the arteries, it could be necessary to delete some misclassified points, as shown in Figure 4.1

- Identification of the central long axis of the radius bone in fractured wrists from 3-D CT images: the algorithm proposed by Hast et al. [20] in a collaboration between

Sweden and Italy is useful to find the optimal set for heavily contaminated sets, even for an inlier ratio under 5%. Its application to assess the displacement of wrist fractures consists of various steps: segmenting the radius bone and computing a surface mesh, selecting a part of the radius shaft located beneath the fracture, calculating per-vertex normal for the selected surface, mapping the surface normals to points on a unit-sphere and using RANSAC to robustly fit a plane to the dense band formed on the points cloud. The normal of that plane will correspond to the direction of the long axis.

- Locating the centre of the femoral head: Jian Wu and Ang Li [26] proposed a method to use the RANSAC algorithm for defining accurately the location of the femoral head (and thus the mechanical axis), which is a key factor for a successful TKA. Indeed, a slight deviation in the mechanic axis can lead to post-procedure aches and shorten the life of the prosthesis. Since it is an inaccessible point, to determine where the centre of the femoral head is located, an infrared tracker is placed on the distal end of the femur and through the rotation of the bone, the movement is tracked. Thus, the centre of the femoral head can be determined, assuming that the surface can be represented with a sphere. During this process, erroneous or invalid data may be collected along with useful data. To solve this problem, this study used data screening to rule out abnormal data.

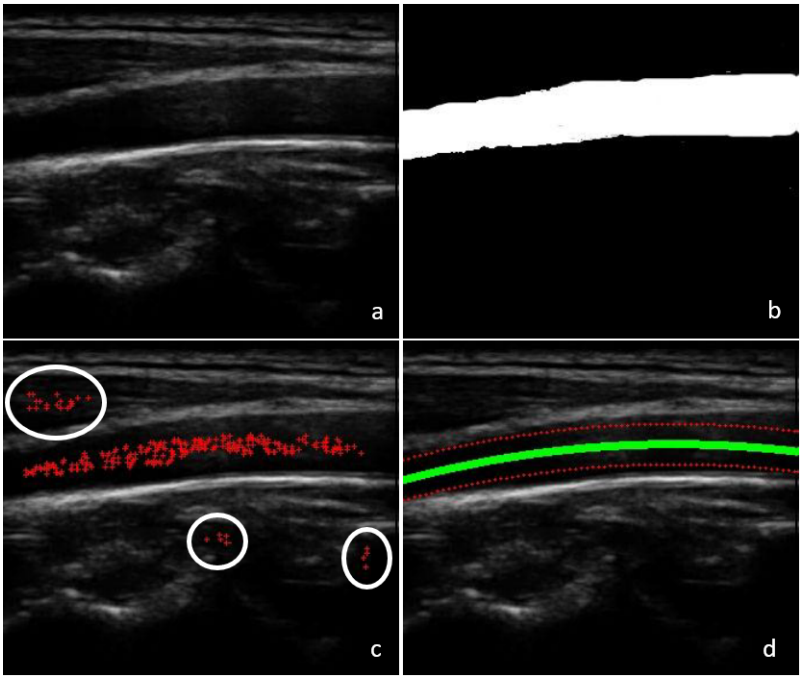

Figure 4.1: a) Input image of an artery from ultrasound images. b) Appropriate mask that defines the precise location of the artery. c) Points classified as “artery points” depicted in the original image. Misclassified points are highlighted. d) Correct localization of the artery, after the application of the RANSAC algorithm. [33]

4.2 RANSAC General Features

The generic application of the RANSAC algorithm to a set of acquired points assume the realization of the following steps:

1. a random selection of points is picked out from the collected data: these points are assumed to be inliers (valid data);
2. the selected data are used in parameter fitting to form a model;
3. the model acquired is used to evaluate other data: if the distance between a data point and the model is less than a certain threshold, then the point is judged as valid, otherwise, it would be judged as invalid;
4. steps 1-3 are repeated: every new model is compared with the last saved model and if the new model contains more valid data, it will be considered as better, and will be saved replacing the old one; if not, the new model will be abandoned.

After repeating this process for a predetermined number of times, it can be assumed that the last model remained after the loop, is the best one. The main idea, however, is to generate a hypothesis from random samples (estimating a model) and then verifying it using all the data (scoring). An example of the application of the RANSAC algorithm over a generic data set affected by outliers is represented in Figure 4.2 [50].

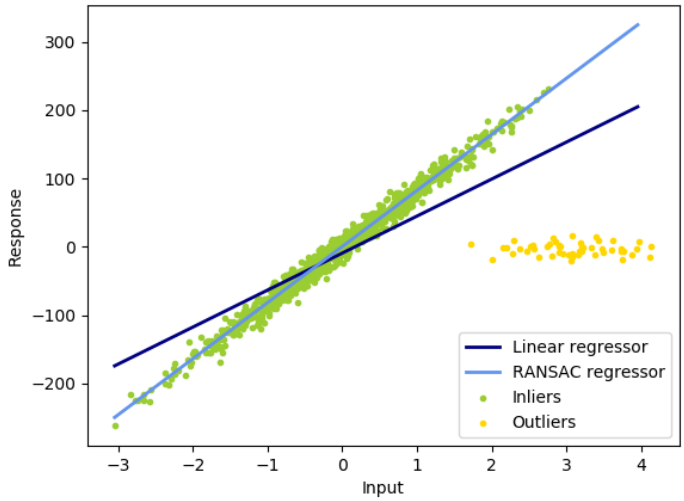

Figure 4.2: Example of the application of the RANSAC algorithm, comparing the Linear regressor with the RANSAC model. *https://scikit-learn.org/stable/auto_examples/linear_model/plot_ransac.html*

Before applying the algorithm to our data set of acquired points on the surface of the patient's bone, a description of all the required parameters is necessary.

Iteration number

Due to its random nature, it is important to state the number of iteration that the algorithm must perform, to reduce the possibility to find contaminated solutions. When the probability to find a better model becomes lower than some threshold, the algorithm terminates, otherwise, it will start again. Generally, N iterations are needed to find an outlier free set, with a probability p (usually set to 99% or more). To calculate N, the following equation can be applied:

$$N = \frac{\log 1 - p}{\log 1 - \gamma^s} \tag{4.1}$$

where γ is the inlier ratio (or the supposed inlier ratio, when it is not known) and s is the number of samples drawn each time at step 1, i.e. the minimum number of samples to define the model. Alternatively, one can also run the algorithm several times and then choose the solution which gives the largest set of inliers.
It could be a common thought that using more data samples (s) would be advantageous, as a more accurate estimate of the model could be obtained. However, having more samples in the sample subset would increase the search space for the subset selection. Thus, in order to keep the probability of finding the optimal model at the same level, we would need to try more sample subset, thus increasing the number of iterations. This will cause an increase in computational complexity [11]. In Figure 4.3 the relationship of sample subset size and number of iterations is shown.

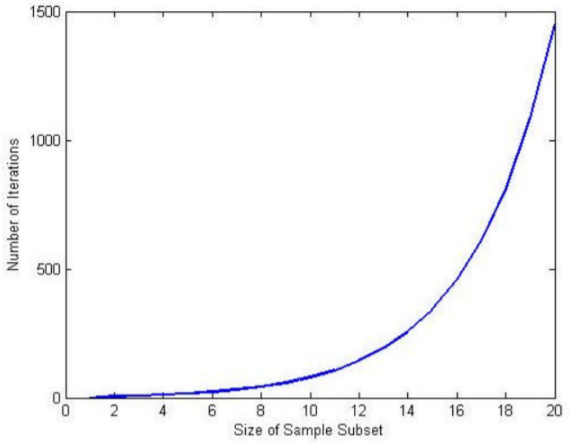

Figure 4.3: Relationship between the size of the sample subset s and the number of iterations N. From: Universitè Paris Descartes courses' material.

Chum et al. [11] proposed a version of the algorithm, called LO-RANSAC, in which the set of tentative inliers already found is resampled, as the set might contain several inliers but also some outliers that must be removed. Resampling is shown in Figure 4.4, where two points of possible inliers (blue) are chosen to construct a line (black). This line is used to compute the new inliers (blue and green ones). All the new inliers are used to construct the line in the right image. This line fits the set better than the previous one.

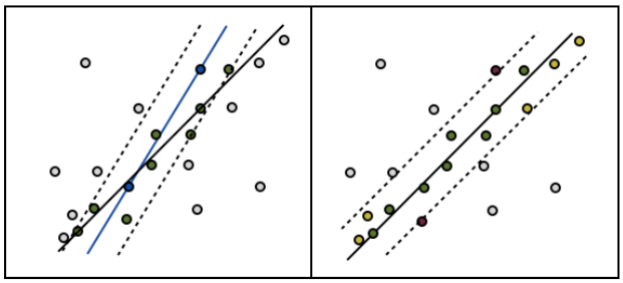

Figure 4.4: Left: A line is constructed from two points (blue). All tentative inliers (green and blue) are used to construct a new line (black). The tentative inliers now fit the set better (right) and include some new points (yellow) and some others are excluded (red). [20]

Minimum Consensus Threshold

Minimum Consensus Threshold (MCT) is the minimum number of samples that would be accepted as a valid consensus to generate a final model for that iteration. If MCT has a low value, some random line that fits a portion of the samples would be considered as a valid consensus. On the contrary, if MCT is too large, even a good estimate would not be accepted, and no final model results would be found.

Threshold distance

Once the model of each iteration is found, we must compute the distance (d) between every point a of the data set and the model (M):

$$d_M(a) = \min_{a^* \in M} dist(a, a^*) = dist(a, a^{\perp}) \tag{4.2}$$

where a^* represents all the points which constitute the model space M, $a^{\perp}$ is the orthogonal projection of a over the model space M, and $dist$ is an appropriate distance function. Given the initial data set:

$$A = \{a_1, \ldots, a_N\} \tag{4.3}$$

the Consensus Set is defined as follows:

$$CS = \{a \in A | d_M(a) < \epsilon\} \tag{4.4}$$

where ϵ is the threshold, i.e. the maximum distance between the point and the model. If $d_M(a)$ is less than ϵ, a is an inlier, otherwise, it is an outlier.

4.3 Non-linear RANSAC

Finding a model to fit the acquisitions taken on a bone surface is not as simple as fitting a linear distribution of data, which contains some outliers. In this case, we deal with

non-linear models, that could be represented in different ways.
Beneš et al. [33] improved the RANSAC algorithm with a suitable method for utilization with a nonlinear data set, for which the classical algorithm could be inappropriate. The new strategy was proposed to be applied for the localization of curved arteries taken from ultrasound images, in which there are some misclassified points. Non-linear mathematical model in this implementation is represented by an explicit polynomial curve (second-order):

$$y = p_2x^2 + p_1x + p_0 \tag{4.5}$$

The first step that they carried out was the construction of the polynomial model, starting from three points, as shown in Figure 4.5.

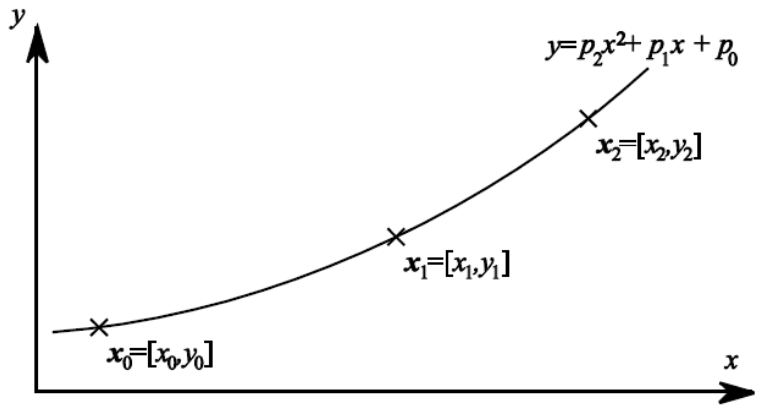

Figure 4.5: Construction of the non-linear model (second order polynomial). [33]

The distance between an arbitrary point $x_0 = (x_0, y_0)$ and the polynomial curve is defined as a distance between point x_0 and the nearest point on the curve x_m (Figure 4.6). Generally, the Euclidean distance $l = \sqrt{((x - x_0)^2 + (y - y_0)^2)}$ is used.

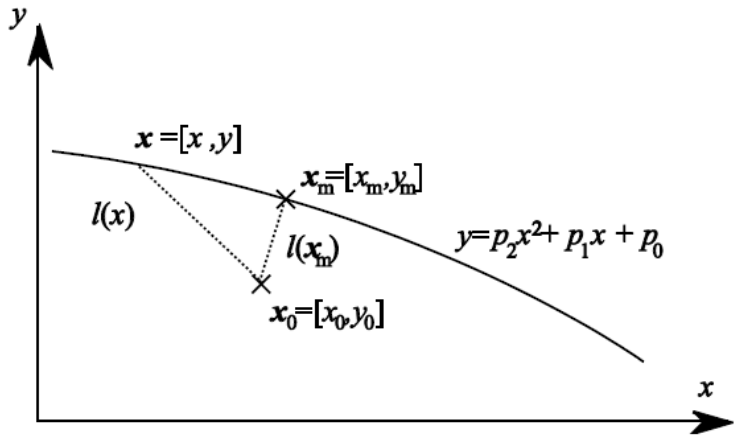

Figure 4.6: Computation of the distance between points and a polynomial curve. [33]

Since the points on the curve have coordinates $x = (x, y) = (x, p_2x^2 + p_1x + p_0)$, the distance would be $l = \sqrt{((x - x_0)^2 + (p_2x^2 + p_1x + p_0 - y_0)^2)}$.

The RANSAC algorithm finds the best mathematical model and appropriate inliers. The final step of the proposed algorithm is the re-computation of the best model, considering all the inliers found. Therefore, the proposed method must fit the polynomial curve through more than three points (Figure 4.7).

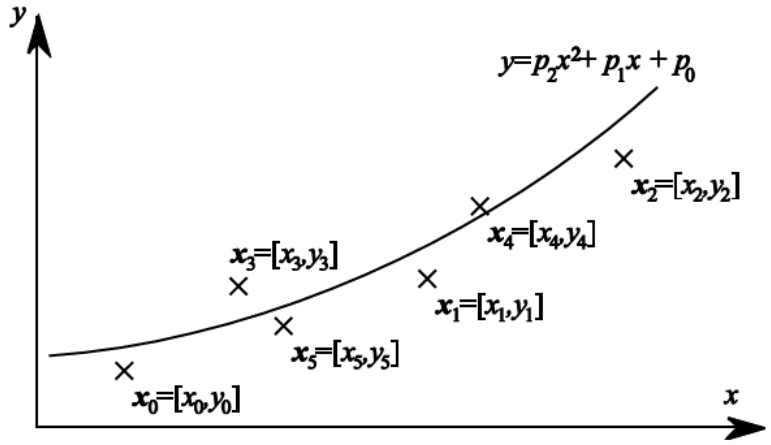

Figure 4.7: Approximation of polynomial curve through more than three points. [33]

Since it is unlikely that the fitting matches more than three points, we have to perform an approximation, which is the process of searching the best model with minimal error. All approximated points must satisfy the equation of mathematical model with a minimal error:

$$y_i + e_i = p_2 {x_i}^2 + p_1 x_i + p_0 \tag{4.6}$$

This approach paves the way to construct an algorithm which is suitable for our purpose, representing a proper model for the surface fitting and thus managing possible outliers.

Chapter 5

Materials: Experimental set-up

After having studied different pathways to model the bones' surfaces and detect possible outliers, the research of the best method to fit the data acquired with BLU-IGS® has been carried out, considering all the previous studies and using a trial-and-error method. As a guideline, "Ockham's razor" was used to build the model: the idea was to not abuse the possibility to add complexity to the model when not strictly necessary.

5.1 Mathematical function

In order to describe the morphology of each patient's bone, a mathematical function that could be adopted in every case must be found. In this section, the strategy used to find the best fitting mathematical function is explained, with some mention on the results obtained from time to time and which then determined the choice of the model. Several models have been tested, until the optimal one has been found, always considering the need not to increase excessively the computational times.

5.1.1 Second-order polynomial model

The research of the model started with the femur distal condyles (medial and lateral), so all the following statements are referred to the distal compartment. At the beginning, a 2-D mathematical model was used to reconstruct the shape of the condyles using intra-operative navigation data, collected from surgeons performing TKA with the BLU-IGS® system. In Matlab® environment, these data were used to reconstruct the patient anatomical RS (as described in chapter 2.1.2). In this way, all the acquired points were translated into this RS, so that they could represent the patient-specific morphology. The first model to be used was a second-order polynomial, since the shape of the points cloud, plotted on the sagittal plane, seems to fit the data with a parabola (Figure 5.1, right image). The fitting was done using 'polyfit' and 'polyval' functions: $p = polyfit(x, y, n)$ returns the coefficients for a polynomial $p(x)$ of degree n that is the best fit (in a least-squares sense) for the data in y. The coefficients in p are in descending powers, and the length of p is $n + 1$; vector p becomes the argument of the 'polyval' function $y = polyval(p, x)$, which

evaluates the polynomial p at each point in x.

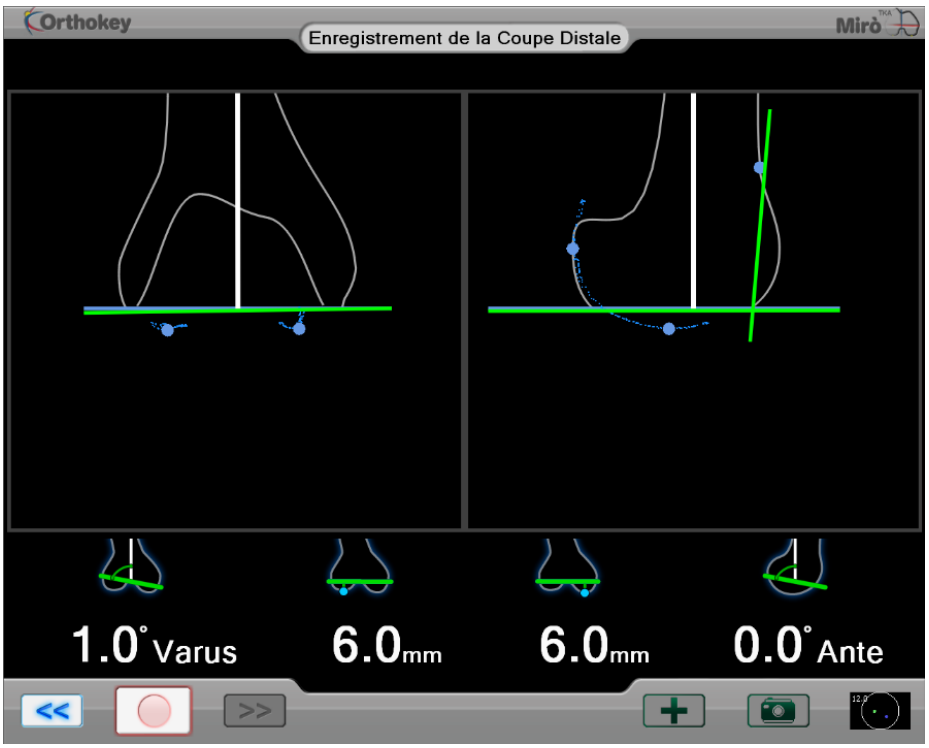

Figure 5.1: Intra-operative acquired data screened on the computer interface. In the right view, the distribution of the points acquired on the femur condyles is similar to a parabola (sagittal plane).

In Matlab® a code for the application of the RANSAC algorithm was implemented. Since the inlier ratio is not known a-priori, and it could vary a lot, it has been chosen not to apply the equation described in chapter 4.2 to set the iteration number, but to impose a pre-defined value. This number of iterations is the result of a series of tentative to find the best compromise between accuracy, repeatability and low computational costs. Other parameters used for this implementation are the threshold distance, the maximum distance between the model and the point, to consider it as an inlier, and the number of samples used to construct the model. The distance was firstly set to 1.5 mm and then changed to compare the results with different threshold, and the number of samples was chosen as the lowest to construct a second-order polynomial, that is three. The resampling method was used with $MCT = 3$, that is the minimum number of inliers found at the first step to construct a second model. The result of this first fitting is shown in Figure 5.2, where the concavity is due to the right limb, which has z-axis oriented distally. The model fits perfectly the outliers' free data, with a coefficient of determination $r = 0,98$. A trial was conducted also with a fourth-order polynomial, but it showed no better results than the second-order model.

The 2-D model fits well the data acquired in a "narrow" portion of the surface (data in Figure 5.2 have a 7,95 mm range along the x-axis), but if the probe covers the entire

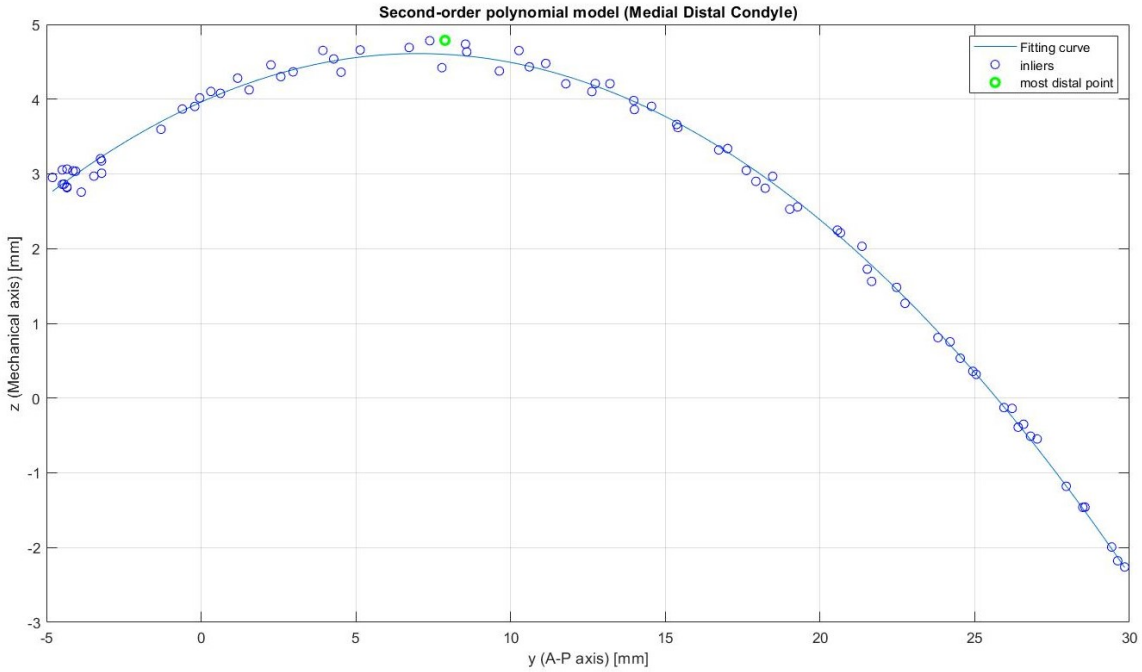

Figure 5.2: Second-order polynomial model fitting the medial distal condyle points. The green point is the most distal point.

condyle area, some of the acquired points could have coordinates along the A-P axis that deviate from the model, since they belong to different planes in the ML direction. This could lead the algorithm to consider some points as outliers when they are not. Figure 5.3 shows a 2-D model in which the acquisition range along the x-axis is 16,1 mm wide and the fitting curve does not fit all the data acquired in different planes. The coefficient of determination is $r = 0,93$ and the red dots are classified as outliers, even if they are not. A 3-D model would fit the data considering also the ML direction.

5.1.2 Paraboloid model

To overcome this issue, a 3-D model should be constructed. In this way, all the acquired points will be plotted in the corresponding planes and matched with the closest point of the model in the 3-D space. To construct the model, we should have a clear idea of the shape of the condyles in a 3-D sense. In the sagittal view, it could be approximated with a parabola, but also in the frontal plane, the shape is similar to a second-order polynomial, with a tighter curvature. A parabolic projection over two orthogonal planes represents a surface called paraboloid. The paraboloid could be either elliptic or hyperbolic, depending on whether the concavity of the polynomial in the two planes are concordant or not (every plane section of a hyperbolic paraboloid is a hyperbola, while every nonempty plane section of an elliptic paraboloid is an ellipse). The shape of the femur condyle approximates an elliptic paraboloid, shown in Figure 5.4.

The mathematical expression of the paraboloid surface is as follows:

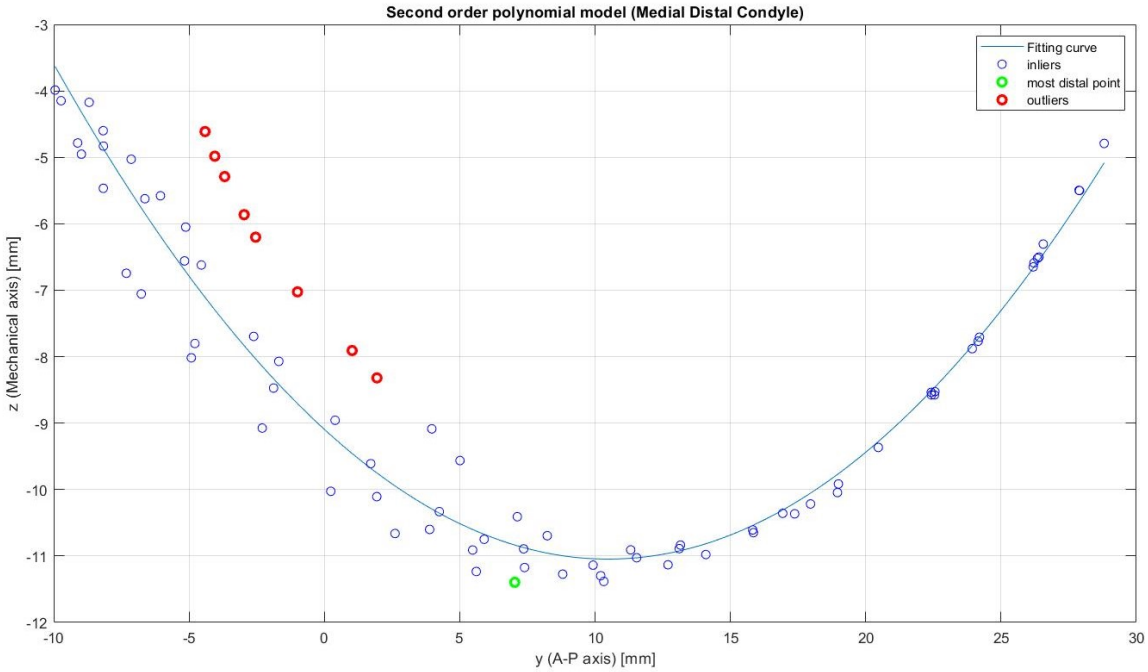

Figure 5.3: Second order polynomial model fitting the data acquired over the medial distal condyle surface. The points which are considered outliers (with a distance to the model > 1.5 mm are represented in red; the most distal point is the green one. The outliers are real points acquired on the bone surface, but they belong to different planes in the ML direction, that is why they have lower y absolute values.

$$S = p_{00} + p_{10}x + p_{01}y + p_{20}x^2 + p_{11}xy + p_{02}y^2 \tag{5.1}$$

The approximation with an elliptic paraboloid is first done via Matlab®, using 'fit' function. This function creates the fit to the data in input, given as vectors, with the model specified, that is 'poly22' to represent a linear polynomial surface of degree two in both the projection planes. The output of the function is the vector representing the coefficient of the mathematical equation, as given in Equation 5.1, with 95% confidence bounds. To construct such surfaces, a minimum of six points is required to solve the system. A boundary condition has to be set on p_{02} and p_{20} to have an elliptic paraboloid. Only positive values are accepted for a left limb and negative values for the right limb, due to the conventional orientation of the mechanical axis.

The algorithm is then built by taking randomly six points from the data set and applying the 'fit' function to these points so that a first model is found. The Euclidean distances from each acquired point and the model are computed and all the points which have a distance to the model lower than the threshold (1,5 mm) are considered as inliers. The inliers are used to build a second model and compute the new distances from the real points and the surface. This process is repeated for several times (N) unless a model produces a number of outliers equal to 0. In this case, the iterations stop and the model

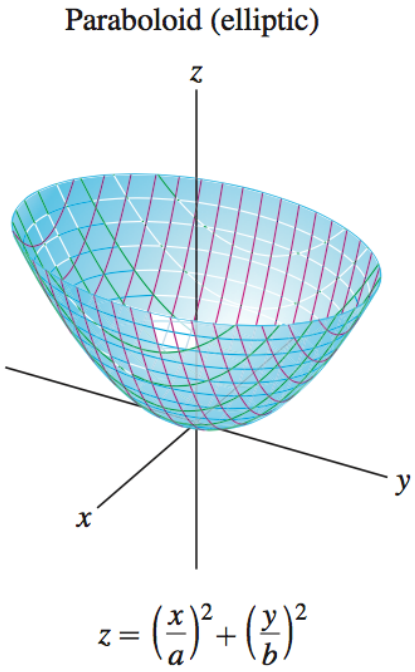

Figure 5.4: Elliptic paraboloid. From: *https://www.slader.com/discussion/question/state-whether-the-given-equation-defines-an-elliptic-paraboloid-a-hyperbolic-paraboloid-or-an-elli-4/*

which returns no outliers is chosen as the best fitting model. This 3-D strategy gives a better representation of the data acquired on the bone surface. The main advantage of this model is that with the 2-D representation, points belonging to the surface of the bone could be considered as outliers, while with the 3-D model this does not happen. The result of the application of the algorithm with a 3-D model is shown in Figure 5.5: the data used to fit the paraboloid are the same of Figure 5.3. In this case, the algorithm does not find any outliers and each point matches the model in the different planes.

5.1.3 Hybrid model

This 3-D approach shows more precise performances but implies higher computational costs. For this reason, it has been decided to apply it only when strictly necessary. When the acquisition on the bone surface is done by spacing the entire area, the 3-D model is used, and when the data acquired show little difference in the ML direction, the 2-D approach is performed. The difference along the x-axis is called delta (δ), and defined as follows:

$$\delta = (\max_{i^* \in [1, N_p]} x_i - \min_{i^* \in [1, N_p]} x_i) \tag{5.2}$$

where N_p is the number of the acquired points, each one represented in the anatomical RS (x_i, y_i, z_i), with $i = 1 \dots N_p$.
If δ is lower than some defined threshold, the 2-D RANSAC starts, otherwise, the 3-D

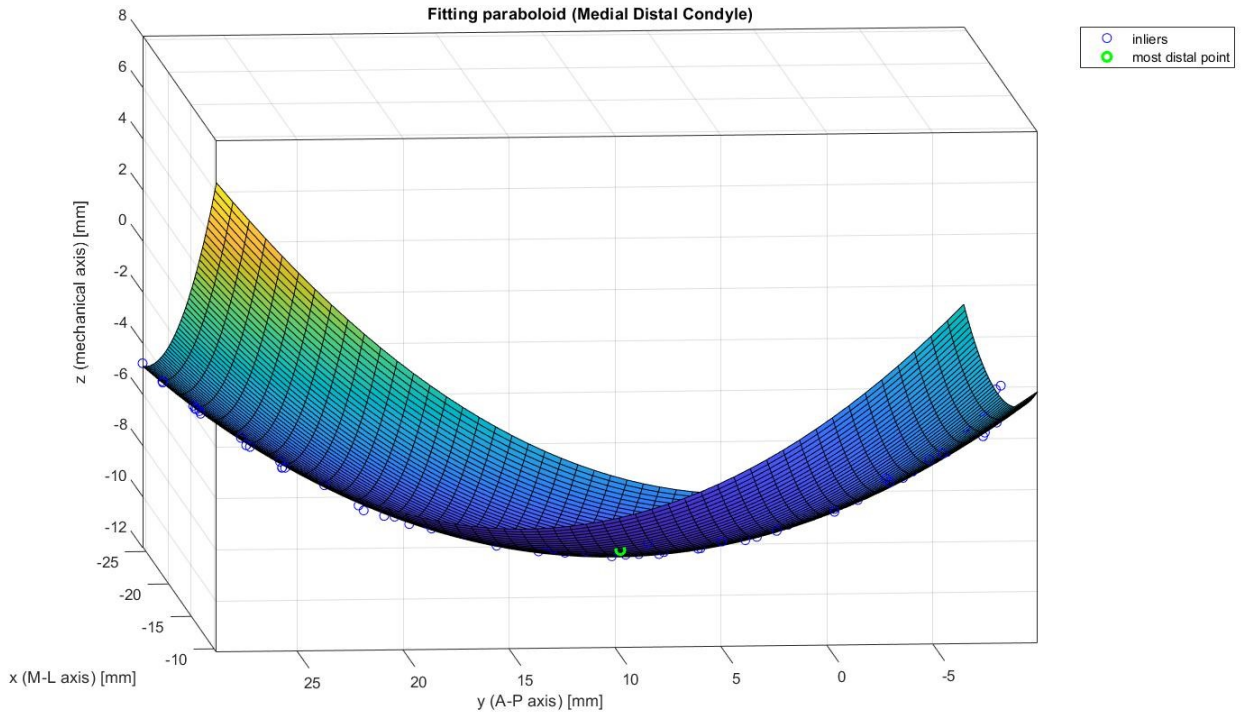

Figure 5.5: Paraboloid model fitted with the acquired data (blue dots). The green dot represents the most distal point on the surface of the medial distal condyle.

RANSAC is applied. At first, this parameter is set equal to 5 mm and then changed to compare results and find the best model.

5.1.4 Spline model

A surface fitting model using splines curves has been tested, to understand if it could be a better model to find outliers. The 'cftool' on Matlab® was used, setting «thin-plate Spline», as the fitting surface type and the result can be seen in Figure 5.6.

With the spline interpolation, the shape of the surface is more realistic: it reflects the real morphology of the bone with all the defects which are not identified by the polynomial model (smooth shape). The disadvantage of using a spline interpolation is that the surface fits also the outliers and cannot detect them. As can be seen in Figure 5.7, the outliers are used to construct the model which results to have deformations. The model was tested with an acquisition affected with an outlier point, and, in this case, the result goes in the opposite direction to the objectives of this work, that is why it was abandoned.

5.1.5 Density function

Another idea was to use a function that computes the density of the acquired points. We assume that the points acquired outside the surface of the condyle have a lower density than those acquired on the surface. The strategy would be to count how many points fall

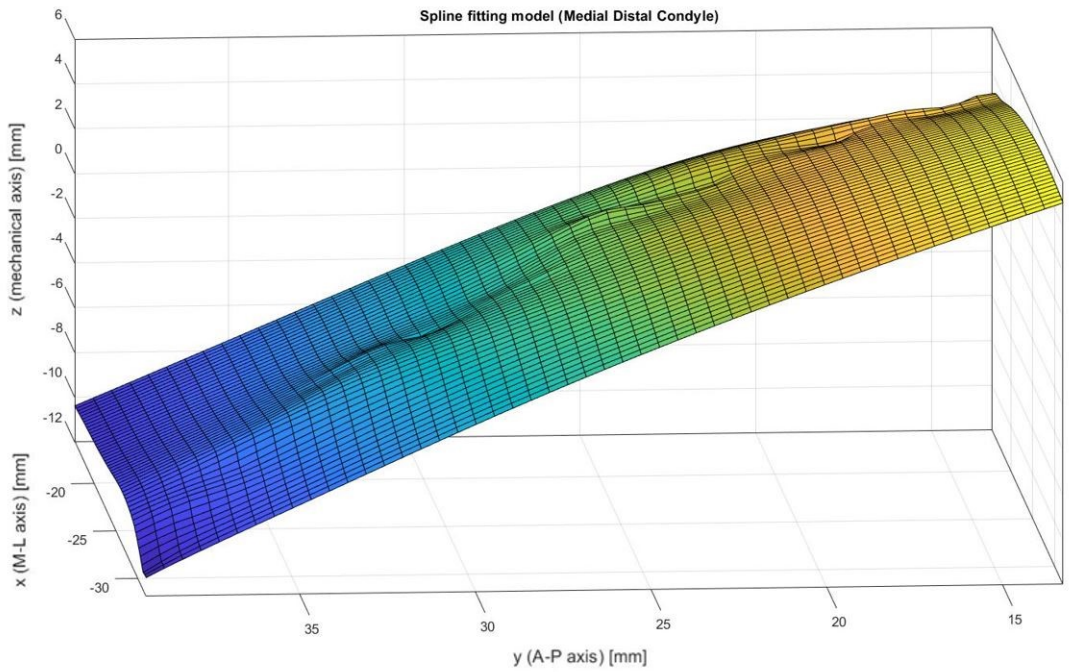

Figure 5.6: Model surface using a spline interpolation.

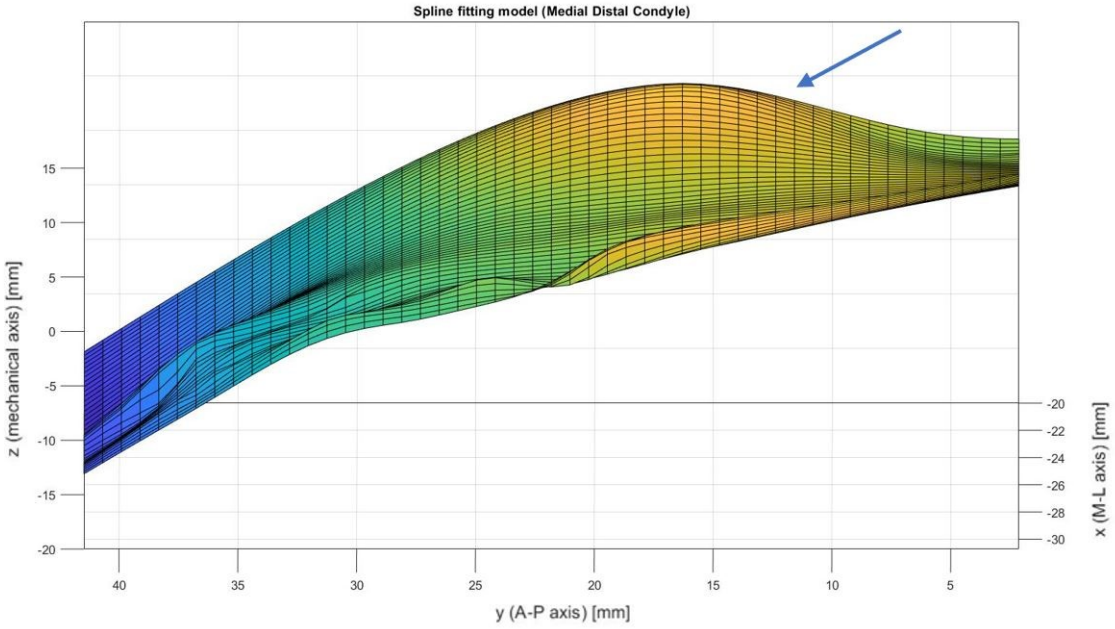

Figure 5.7: Spline fitting model with outliers. The deformation induced by the outliers is indicated by the arrow.

within the neighbourhood of each acquisition. If the number of points is higher than an established value, the density is high, and the point must be kept. If the acquired point is isolated, then it can be considered as an outlier. This method can be applied as an alternative to RANSAC, but also as a further check, thus taking as outliers the subset

consisting of the points detected as outliers by RANSAC and the density function.

This function was implemented by choosing as neighbourhood a cube with side equal to 4 mm and the limit value to consider the acquisition as an outlier was set to 4: less than 4 acquisitions falling into a cube centred on the current point, make that point an outlier.

The application showed no satisfying results for those acquisitions in which the surgeon does not insist on the most distal portion of the distal condyle: qualitatively analysing Figure 5.8, it can be seen that the pink dots are accounted to be outliers, but probably the most distal point, necessary for the cut planning, is within those points. This strategy was then abandoned.

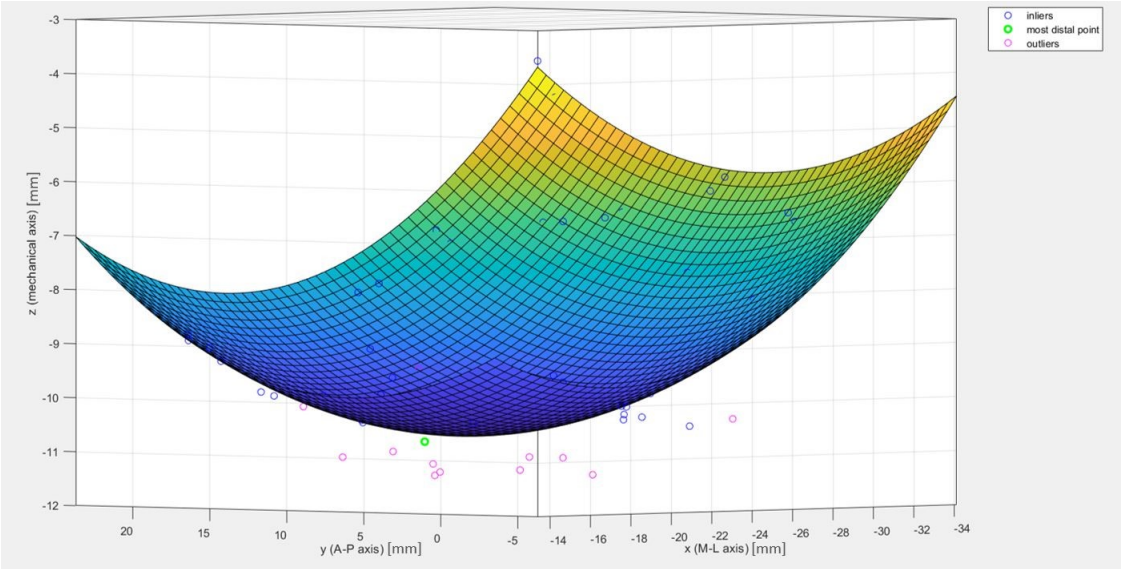

Figure 5.8: Application of the density function on a dataset free of outliers: the most distal points on the surface of the bone are not characterized by high density and they are considered as outliers (purple points).

5.1.6 Other compartments

The previous statements are relative to the medial and lateral distal condyles, so the next step was to find a model for the posterior condyles and the tibial plateaux. As regards the posterior condyles, the shape could be approximated to a paraboloid as well, but the axes which define the orientation of the surface are different from the distal compartment. The main axis which describes the paraboloid constructed on the distal condyle is the mechanical axes (z), and the paraboloid forms parabolic projections over the sagittal (yz) and frontal (xz) plane. The posterior condyle could match a paraboloid with the A-P direction as the main axes (y) and parabolic projections over the transverse (xy) and sagittal (zy) planes (see Appendix A.1). The functions used are thus the same for the distal and posterior condyles, with the only exception that the data are organized and

handled considering different orientation axes:

- 2-D model
  - Distal compartment: $polyfit(y, z)$
  - Posterior compartment: $polyfit(z, y)$
- 3-D model
  - Distal compartment: $fit([x, y], z)$
  - Posterior compartment: $fit([x, z], y)$

where the last vector given as input in the functions is the parabolic/paraboloid axis.

The tibial compartment could be considered as a planar surface, but the slight curvature allows us to treat the surface as for the distal compartment, with which the tibial plateau articulates, using a paraboloid as well. Unlike distal condyles, the paraboloid for the tibial compartment describes a concave surface, in which the point to be identified is the most distal one. The main axis for the tibial paraboloid is the mechanical axis (z), as for the distal compartment. Since the tibial plateaux surface is close to a plane, we expect that the coefficients which describe the paraboloid are close to zero.
In this way, we have a unique model that describes the three landmark surfaces: distal condyles, posterior condyles, and tibial plateaux.

5.1.7 Additional constraints

To avoid coarse acquisitions, in which the surgeon may take points which are far from the surface of the bone, some additional constraints are added into the algorithm implementation, deleting all the acquired points which have coordinates very far from the physiological values.

This is a tricky passage that must be handled with the right caution: each patient's bone has its own characteristics and morphology and the presence of unusual coordinates is not to be excluded. Some points could be out of range if they belong to the surface of exceptionally large, small, or deformed bones. The values which define the "normal" ranges have been round up, considering anomalous but real cases.

The RANSAC algorithm takes as input all the acquired points which are within the following ranges, divided into parts and relative to a left limb (mechanical axis oriented proximally, with origin in the intercondylar notch and tibial spine, respectively for the femoral and tibial RS):

- Tibial Medial Emiplateau: [-10 mm; 5 mm] in z-direction;
- Tibial Lateral Emiplateau: [-10 mm; 5 mm] in z-direction;

- Medial Posterior Condyle: [30 mm; 50 mm] in y-direction;
- Lateral Posterior Condyle: [25 mm; 50 mm] in y-direction;
- Medial Distal Condyle: [-25 mm; 5 mm] in z-direction;
- Lateral Distal Condyle: [-25 mm; 5 mm] in z-direction.

5.1.8 Best fitting model

Different fitting models are evaluated by varying the parameters δ, ϵ, and N_{iter} and testing several combinations of values. δ was varied from 5 mm to 6,5 mm; N_{iter} was increased starting from 10 iterations; ϵ was varied until a value of 1,5 mm, since the surgeon accounts a 2 mm error to be appreciable at a clinical level (so it can lead to negative consequences on the operation) and considering the system accuracy to be 0,5 mm. The results obtained from every model are compared to find the most appropriate one. After having tested different model parameters, the results relative to each combination were collected and compared so that the best model was found. The model characteristics are explained below, with a detailed description of how the algorithm works.

1. The data acquired are transformed from the cameras RS to the anatomical reference system (see Appendix B for changing the RS of a set of points) and organized into coordinates x, y, and z for each acquisition point.
2. The reference direction of each compartment acquired with STREAM mode is analysed (z for distal condyles and tibial emiplateaux; y for posterior condyles): if the data do not fall within the reasonable ranges, they are deleted.
3. The remaining acquisitions are counted: if the total number is less than 15, the RANSAC algorithm is not applied. This passage was added to avoid that the algorithm is applied also when the acquisition is not made in STREAM mode, but just one point (or a few points) is acquired on the precise landmark region. In this case, the reconstruction of the surface would be complex and useless. This number was chosen since the system acquisition frequency is about 15-20 frames per second, and the acquisition of a single point requires approximately 1 s.
4. δ is then examined: if the acquisition spaces the bone surface along the x-axis with a $\delta > 6,5$ mm, the 3-D model is applied, otherwise, the 2-D model would be sufficient to describe the curvature of the compartment.
5. If $\delta > 6,5$ mm the 3-D algorithm starts to find the best matching surface from the points (>15) which have passed step 2, with the constraint to find an elliptic paraboloid. For any reason due to the particular distribution of the points acquired, it could happen that the algorithm cannot find an elliptic paraboloid that fits the data, but only finds hyperbolic paraboloids. In this case, since the only surfaces found do not describe well the bone morphology, the 2-D model is applied.

6. $\delta < 6,5$ mm or if the condition in step 5 occurs, the 2-D model is applied, and the parabolic fitting line is constructed from the points (>15) which have passed step 2.

7. The output of the algorithm are the best fitting surface and the outliers indexes if case they are found.

8. The inliers can now be used to compute the reference points to determine the planning of the cut and the prosthesis size.

Going deeply into step 5 and 6, the description of the algorithm is given below in both the versions, 2-D and 3-D.

- 3-D model

    1. Six random points are selected;
    2. A paraboloid model is constructed with these six possible inliers;
    3. The coefficients of the surface are examined: if the requirements of the elliptic paraboloid are satisfied, the algorithm goes on, otherwise, step 1 is performed again and the number of iterations increases by one;
    4. The distance from each point and the model is computed;
    5. Each point which has a distance from the model inferior to 1,2 mm is considered as an inlier and (if the number of inliers is ≥ 6) used to construct a second (more precise) model;
    6. The coefficients of the new surface are examined again: if the paraboloid is elliptic, the algorithm goes on, otherwise, step 1 is performed again and the number of iterations increases by one;
    7. The distance from each point and the new model is computed again;
    8. Every point that has a distance higher than 1,2 mm is considered as an outlier;
    9. If the number of outliers is less than the previous iteration, the current model is saved as the best one, otherwise, it is discarded;
    10. If the number of outliers is equal to zero, the algorithm stops without any other iteration: the best model is the current one with no outliers found;
    11. If the number of outliers is not zero, the number of iterations increases by one and the algorithm starts again from step 1;
    12. When the number of iterations is equal to 40, the algorithm stops.

- 2-D model

    1. Three random points are selected;
    2. A parabolic model is constructed with these three possible inliers;
    3. The distance from each point and the model is computed;

Table 5.1: Best model parameters.

Variable name	Description	Value set
N_{iter}	Number of iterations	40
s (3-D model)	Number of samples drawn at each iteration	6
s (2-D model)	Number of samples drawn at each iteration	3
MCT (3-D model)	Minimum number of inliers found with the first model, to construct the second model (resampling)	6
MCT (2-D model)	Minimum number of inliers found with the first model, to construct the second model (resampling)	3
δ	Maximum difference along the data in ML direction to apply the 2-D model	6,5 mm
ϵ	Maximum distance from a point to the model to consider the point as an inlier	1,2 mm

4. Each point which has a distance from the model inferior to 1,2 mm is considered as an inlier and (if the number of inliers is ≥ 3) used to construct a second (more precise) model;
5. The distance from each point and the new model is computed again;
6. Every point that has a distance higher than 1,2 mm is considered as an outlier;
7. If the number of outliers is less than the previous iteration, the current model is saved as the best one, otherwise, it is discarded;
8. If the number of outliers is equal to zero, the algorithm stops without any other iteration: the best model is the current one with no outliers found;
9. If the number of outliers is not zero, the number of iterations increases by one and the algorithm starts again from step 1;
10. When the number of iterations is equal to 40, the algorithm stops.

A summary of the model parameters is given in Table 5.1:

5.2 Log file

The algorithm is applied on a set of points acquired on a plastic specimen with the BLU-IGS® system, provided by the company Orthokey s.r.l. After the acquisition, the software creates a folder for each patient, containing the information needed:

- *Report of the surgery* with patient's and doctor's information, details of the implanted prosthetic components and pre- and post-operative values of the degree of varus-valgus deformity;

- *Log file* in text format containing the roto-translation matrices of the navigated instruments, in the reference system of the cameras, relative to all the recorded surgical passages (called scenes). The file is organized as follows (see also Figures 5.9 and 5.10 as an example):
  - label relative to the acquired scene "@label '*name*'";
  - the first column represents the acquired frame, thus the index increases progressively with the acquisition time;
  - the second column represents the objects' index (0, 1 or 2 respectively for femoral star, tibial star, probe): in a scene, more than one object can be detected;
  - the third column is an indicator that reports whether the acquisition is going on or not;
  - from the fourth column onwards, the roto-translation matrix, which described the orientation of the object in the cameras RS, is reported;

```
/*
 * @label Hip Joint
 */

0 0 1 123.599998 -21.330000 -1718.209961 -0.932007 0.101558 -0.347922 -0.049406 -0.986578 -0.155635 -0.359058 -0.127863 0.924515

1 0 1 123.970001 -21.059999 -1718.170044 -0.931969 0.102845 -0.347644 -0.050865 -0.986527 -0.155489 -0.358951 -0.127228 0.924644

2 0 1 124.540001 -20.860001 -1717.130005 -0.932986 0.105587 -0.344077 -0.053243 -0.985972 -0.158192 -0.355953 -0.129271 0.925520

3 0 1 124.930000 -21.379999 -1714.400024 -0.934432 0.108296 -0.339277 -0.053282 -0.984435 -0.167479 -0.352133 -0.138420 0.925658

4 0 1 124.730003 -22.150000 -1712.459961 -0.935749 0.108579 -0.335537 -0.051827 -0.983434 -0.173702 -0.348839 -0.145151 0.925874

5 0 1 122.959999 -25.299999 -1707.339966 -0.937510 0.105651 -0.331532 -0.041740 -0.980056 -0.194288 -0.345447 -0.168309 0.923222

6 0 1 121.120003 -27.879999 -1704.729980 -0.938814 0.099971 -0.329597 -0.032489 -0.978386 -0.204216 -0.342889 -0.181013 0.921771

7 0 1 115.529999 -34.540001 -1700.229980 -0.940025 0.082071 -0.331086 -0.005617 -0.974217 -0.225544 -0.341060 -0.210157 0.916249

8 0 1 112.160004 -38.330002 -1699.199951 -0.939818 0.069680 -0.334495 0.011000 -0.972307 -0.233450 -0.341498 -0.223080 0.913025

9 0 1 104.690002 -45.959999 -1700.319946 -0.937830 0.042023 -0.344542 0.045148 -0.969442 -0.241130 -0.344147 -0.241694 0.907274

10 0 1 101.150002 -49.240002 -1702.630005 -0.935412 0.028197 -0.352433 0.060987 -0.969005 -0.239397 -0.348260 -0.245428 0.904699
```

Figure 5.9: Log file example relative to the first 10 scenes of the acquisition of the hip joint. In this case, only the femoral star (0) is present and the STREAM mode is used.

```
/*
 * @label Tibial Spine
 */

0 1 1 99.250000 132.300003 -1724.020020 0.473786 -0.541534 -0.694455 0.577493 0.786405 -0.219247 0.664853 -0.297167 0.685319
0 2 1 -23.459999 -6.180000 -1727.900024 0.289173 -0.895535 0.338226 -0.060434 0.335537 0.940086 -0.955367 -0.292288 0.042908
```

Figure 5.10: Log file example relative to the only scene of the acquisition of the tibial spine. In this case, the tibial star (1) and the probe (2) are present and the landmark is acquired as a single point.

5.3 C++ Application

Although the optimization process was achieved and checked in Matlab® environment, the application to the BLU-IGS® system was to be performed in C++, in order to insert the algorithm into the software. A research was carried out to look for a library that gives the same output of the function used in Matlab®, and the most suitable was found to be the "Geometric Tools" library. It is a collection of source code for computing in the fields of mathematics, graphics, image analysis and physics.

5.3.1 3-D Model

The fit options relative to the 'poly22' type in Matlab® allow to identify the method by which the fitting is carried out, that is the 'Linear Least Squares'. The Geometric Tools library presents the possibility to "Fitting a Paraboloid to 3-D Points of the Form $(x; y; f(x, y))$, using the same minimization method. The mathematical background is here presented, referring to the documentation "Least Squares Fitting of Data by Linear or Quadratic Structures".

Given a set of samples $\{(x_i, y_i, z_i)\}_{i=1}^m$ and assuming that the true values lie on a paraboloid

$$z = f(x, y) = p_1x^2 + p_2xy + p_3y^2 + p_4x + p_5y + p_6 = \mathbf{P} \cdot \mathbf{Q}(x, y) \tag{5.3}$$

where $\mathbf{P} = (p_1, p_2, p_3, p_4, p_5, p_6)$ and $\mathbf{Q}(x, y) = (x^2, xy, y^2, x, y, 1)$, we must select $\mathbf{P}$ to minimize the sum of squared errors

$$E(\mathbf{P}) = \sum_{i=1}^{m} (\mathbf{P} \cdot \mathbf{Q}_i - z_i)^2 \tag{5.4}$$

where $\mathbf{Q}_i = \mathbf{Q}(x_i, y_i)$. The minimum occurs when the gradient of E is the zero vector,

$$\nabla E = 2 \sum_{i=1}^{m} (\mathbf{P} \cdot \mathbf{Q}_i - z_i)\mathbf{Q}_i = 0 \tag{5.5}$$

With algebraic rearrangements one can convert the Equation 5.5 to a system of six equation in six unknowns, as follows:

$$\left(\sum_{i=1}^{m} \mathbf{Q}_i \mathbf{Q}_i^T \right) \mathbf{P} = \sum_{i=1}^{m} z_i \mathbf{Q}_i \tag{5.6}$$

$\mathbf{Q}_i\mathbf{Q}_i^T$ is the product of the 6×1 matrix $\mathbf{Q}_i$ with the 1×6 matrix $\mathbf{Q}_i^T$, and the result is a 6×6 matrix.
One can define the 6×6 symmetric matrix $\sum_{i=1}^m \mathbf{Q}_i\mathbf{Q}_i^T$ and the 6×1 vector $B = \sum_{i=1}^m z_i\mathbf{Q}_i$. The choice for $\mathbf{P}$ is the solution to the linear system of equation $A\mathbf{P} = \mathbf{B}$. The entries of A and $\mathbf{B}$ indicate summations over the appropriate product of variables. For example $s(x^3y) = \sum_{i=1}^m x_i^3 y_i$.

$$\begin{bmatrix} s(x^4) & s(x^3y) & s(x^2y^2) & s(x^3) & s(x^2y) & s(x^2) \\ s(x^3y) & s(x^2y^2) & s(xy^3) & s(x^2y) & s(xy^2) & s(xy) \\ s(x^2y^2) & s(xy^3) & s(y^4) & s(xy^2) & s(y^3) & s(y^2) \\ s(x^3) & s(x^2y) & s(xy^2) & s(x^2) & s(xy) & s(x) \\ s(x^2y) & s(xy^2) & s(y^3) & s(xy) & s(y^2) & s(y) \\ s(x^2) & s(xy) & s(y^2) & s(x) & s(y) & s(1) \end{bmatrix} \begin{bmatrix} p_1 \\ p_2 \\ p_3 \\ p_4 \\ p_5 \\ p_6 \end{bmatrix} = \begin{bmatrix} s(zx^2) \\ s(zxy) \\ s(zy^2) \\ s(zx) \\ s(zy) \\ s(z) \end{bmatrix} \tag{5.7}$$

An implementation of this system is given in GteApprParaboloid3.h, which was used to construct the paraboloid surface in the 3-D space and match the data point. The function gives as output the coefficients of the mathematical model, as in Matlab®. The results were compared, and it was verified that the coefficients obtained with both the programmes were the same. From the coefficients, it is possible to reconstruct the surface and compute the distances between each acquired point and the model surface.

5.3.2 2-D Model

As regards the 2-D model, the "Fitting with Standard Polynomials" is performed from the library Geometric Tools. The mathematical background is here presented, referring to the documentation "Least-Squares Fitting of Data with Polynomials". Given a set of n points $\{(x_k, y_k)\}_{k=0}^{n-1}$ with $x_{k+1} > x_k$ for all k, the goal is to fit the data with a polynomial of degree d:

$$y = \sum_{i=0}^{d} c_i x^i \tag{5.8}$$

The least-squares method selects the coefficients c_i to minimize the squared error function

$$E(c_0, \ldots, c_d) = \sum_{k=0}^{n} \left(\sum_{i=0}^{d} c_i x_k^i - y_k \right)^2 \tag{5.9}$$

This is a nonnegative quadratic function regarding the coefficients and obtains its global minimum when the gradient of E is zero; this means that the partial derivatives of E must be zero:

$$0 = \frac{\partial E}{\partial c_j} = 2 \sum_{k=0}^{n-1} \left(\sum_{i=0}^{d} c_i x_k^i - y_k \right) x_k^j \tag{5.10}$$

For $0 \leq j \leq d$. The equation simplifies to:

$$\sum_{i=0}^{d} \left(\sum_{k=0}^{n-1} x_k^{j+i} \right) c_i = \sum_{k=0}^{n-1} x_k^j y_k \tag{5.11}$$

This is a linear system of $d+1$ equations in $d+1$ unknowns and is of the form

$$A^T A\mathbf{c} = A^T y \tag{5.12}$$

where $A = [a_{ki}]$ is an $n \times (d+1)$ matrix whose general entry is $a_{ki} = x_k^i$, $\mathbf{c} = [c_j]$ is a $(d+1) \times 1$ column vector, and $\mathbf{y} = [y_k]$ is an $n \times 1$ vector.
The coefficient matrix of the system is:

$$A^T A = \begin{bmatrix} \sum_{k=0}^{n-1} 1 & \sum_{k=0}^{n-1} x_k & \cdots & \sum_{k=0}^{n-1} x_k^d \\ \sum_{k=0}^{n-1} x_k & \sum_{k=0}^{n-1} x_k^2 & & \sum_{k=0}^{n-1} x_k^{d+1} \\ \vdots & \vdots & \ddots & \vdots \\ \sum_{k=0}^{n-1} x_k^d & \sum_{k=0}^{n-1} x_k^{d+1} & \cdots & \sum_{k=0}^{n-1} x_k^{2d} \end{bmatrix} \tag{5.13}$$

The assumption that the x_k are increasing guarantees that $A^T A$ is invertible, so the coefficients of the polynomial are

$$c = (A^T A)^{-1} A^T \mathbf{y} \tag{5.14}$$

The implementation of the code, both for the 2-D and 3-D model is given in Appendix D.

Chapter 6

Methods: Data Analysis

Many acquisitions are performed in vitro with plastic bone specimens, using the BLU-IGS® system and the outcomes relative to the best model are shown in this section. The registrations are made trying to mimic the surgeon's movements in the operating room and thinking about the possible errors that can occur in the manoeuvres. The modalities of acquisitions used are:

- space the entire surface with "zigzag" movements;
- space the whole surface with random movements;
- space the entire surface with small circles;
- acquire concentrated points near the most distal/proximal point depending on the compartment;
- acquisition of a point;
- single swipe (for condyles surfaces);
- repeated swipe (for condyles surfaces).

A list of possible sources of outliers is given below:

- slightly detaching from the bone surface during the acquisition;
- starting the acquisition before the probe is on the bone surface;
- ending the acquisition when the probe has already detached from the bone surface;
- sliding with the probe sideways.

The different combinations of modalities and errors in the acquisition are tested. The points cloud is elaborated in Matlab®, where the acquired points are represented in the anatomical RS and the algorithm is applied. For each compartment, the relative reference point (RP) is identified, as the point that the software uses to generate the cut planning or to compute the suitable prosthesis size (Table 6.1).

To quantify the goodness of each model, the following strategy is carried out.

Table 6.1: Reference points relative to the different compartment acquired with the STREAM mode.

Compartment	**Abbreviation**	**Reference Point (RP)**
Medial Posterior Condyle	MPC	Most posterior point ($y = y_{max}$)
Lateral Posterior Condyle	LPC	Most posterior point ($y = y_{max}$)
Medial Distal Condyle	MDC	Most distal point ($z = z_{min}$ for left limb; $z = z_{max}$ for right limb)
Lateral Distal Condyle	LDC	Most distal point ($z = z_{min}$ for left limb; $z = z_{max}$ for right limb)
Tibial Medial Emiplateaux	TME	Most distal point ($z = z_{min}$ for left limb; $z = z_{max}$ for right limb)
Tibial Lateral Emiplateaux	TLE	Most distal point ($z = z_{min}$ for left limb; $z = z_{max}$ for right limb)

1. A set of good acquisitions is performed;
2. The right coordinates of the RP are saved as the average coordinates;
3. Acquisitions affected by outliers are performed;
4. RP of each acquisition in step 2 is saved;
5. RPs of step 4 are compared to the right location found at step 1;
6. The algorithm is applied to all the acquisitions and the outliers are removed from every points cloud.
7. The RP of all the acquisitions gone through the algorithm is saved and compared to the right locations found at step 1;
8. The difference between the right location of the RP and their current coordinates is saved for both the cases (with and without the application of the algorithm) as an error quantification;
9. The errors relative to the set of points to which the algorithm is applied and not are compared, to verify the effectiveness of the algorithm itself. Thus, the difference between the errors before and after applying the algorithm is computed as follows (Equation 6.1):

$$\Delta = |e_{nonRANSAC}| - |e_{RANSAC}| \tag{6.1}$$

If Δ is positive, the algorithm lead to improvement, while a negative Δ means that the application of the algorithm was not proper.

6.1 Dataset

Different datasets were used for validating the algorithm. The first one was taken from intra-operative data collected from earlier surgeries, while other two datasets were recorded on plastic bones.

6.1.1 Intra-operative dataset

A first test is tried on a dataset of acquisitions made by different surgeons in the operating room, about which there was no information neither on the modality used for the registration nor on the presence/absence of outliers. The dataset contains 133 acquisitions and it is briefly described below:

- Most of the acquisitions are well-done especially by the surgeons that have used the system for a long time. The 3-D and 2-D plots of the acquisitions in the anatomical RS perfectly describe the bone morphology and the algorithm does not find any outlier.
- A small group of acquisition contains disordered data, probably coming from trials made by the product specialists. This hypothesis is confirmed by looking at the duration of the intervention, that suggests these acquisitions come from demos. This subset of acquisitions is deleted.
- A specific case affected by outliers. The acquisition was taken from a surgery in which the surgeon found out that the output of the software was not compliant with the patient's bone. Looking at the software interface in Figure 6.1, it can be easily seen that during the registration, some wrong points have been acquired, thus leading to improper results. Figure 6.1 also shows the gap between the planned cut (blue line) and the surgeon's final choice (green line).

Since there is no certain information about the acquisition mode or relative to the possible presence of outliers in the entire dataset, the validation is made on a set of data acquired on a plastic specimen. The acquisition modality and the presence or not of outliers has been denoted, so that the results of the algorithm application can be compared with the real cases, with a feedforward control.
Two recording sessions have been performed: in the first one, the acquisitions are made by one single person, who had the complete control on how the algorithm works; in the second session, the acquisitions are recorded by three different people, who knew the system and the main purpose of the algorithm, but not every single step that constitute it. As specialists, two of them (later called Operator 2 and Operator 3) know the surgeons' attitudes and the movement they make during the registration of the bone's surface as well as the possible source of errors during the acquisitions phase. From here on, the first recording session will be identified as "validation 1" and the second one as "validation 2". Within the same validation dataset, the RS must not change, thus the landmarks that

Figure 6.1: Screenshot of the software interface during a TKR surgery in which the acquisition is affected by outliers. The most distal point lies on a different plane compared to the expected bone surface. The planning of the cut is represented in a blue line, while the green line represents the real cut made by the surgeon.

constitute the RS are acquired once and maintained the same for every acquisition of all the compartments.

6.2 Validation 1: features

The six compartments (MPC, LPC, MDC, LDC, TME, TLE) were acquired in the following way, using the modalities acquisitions previously listed:

- The first 20 acquisitions are made without outliers: this subset has been used to locate the right RPs by computing the averaged position.
- 15 acquisitions with outliers are collected by starting the acquisition before the probe is on the bone surface;
- 15 acquisitions with outliers are collected by slightly detaching from the bone surface during the acquisition;

When acquiring the condylar surface, the following modality is added:

- 5 acquisitions with outliers are collected by sliding with the probe sideways.

Table 6.2: 'Validation 1' dataset.

Tot acquisitions	**329**
Not valid	2
With outliers	202
Without outliers	125

Table 6.2 reports some information about the numbers and characteristics of the acquired surfaces. Within the data set, two acquisitions were considered not valid, since the acquisitions were made in a wrong compartment, thus leading to invalid coordinates and the inability to examine correctly the data.

6.2.1 Validation 2: features

In the second recording session, twenty acquisitions were collected for each compartment, by each of the three operators, as follows:

- Femoral condyles
  - 5 acquisitions without outliers
    1. space the entire surface with "zigzag" movements;
    2. space the whole surface with random movements;
    3. single swipe;
    4. repeated swipe;
    5. acquire concentrated points near the most distal/proximal point depending on the compartment;
  - 5 acquisitions with outliers
    1. space the entire surface with "zigzag" movements, slightly detaching from the bone surface during the acquisition;
    2. space the entire surface with random movements, starting the acquisition before the probe is on the bone surface;
    3. single swipe, ending the acquisition when the probe has already detached from the bone surface;
    4. repeated swiping, detaching slightly from the bone surface during acquisition;
    5. acquire concentrated points near the most distal / proximal point, sliding with the probe laterally;
  - 5 acquisitions without outliers, recording the surface at will
  - 5 acquisitions with outliers, recording the surface at will
- Tibial emiplateaux

- 5 acquisitions without outliers
  1. space the entire surface with “zigzag” movements;
  2. space the whole surface with random movements;
  3. space the entire surface with small circles;
  4. acquire concentrated points near the most distal point;
  5. acquire a single point;
- 5 acquisitions with outliers
  1. slide down anteriorly;
  2. slide down laterally;
  3. space the entire surface, detaching slightly from the bone surface during the acquisition;
  4. space the entire surface, starting the acquisition before the probe is on the bone surface;
  5. acquire concentrated points near the most distal point, ending the acquisition when the probe has already detached from the bone surface;
- 5 acquisitions without outliers, recording the surface at will
- 5 acquisitions with outliers, recording the surface at will

At the end of the registration phase made by the three operators, 5 good acquisitions, free of outliers were acquired for every compartment. These acquisitions were used as reference to compute the points that will be recorded as ideal RPs. Table 6.3 reports some information about the numbers and characteristics of the acquired surfaces. Within the data set two non-valid acquisitions relative to the MPC were found, since the software reported non logical values in the coordinates of the femoral star (inf), as reported in Figure 6.2. This situation occurs when the cameras do not have the femur within their field of vision.

```
11796 0 0 inf inf inf inf inf inf inf inf inf inf inf inf
11796 2 1 -108.629997 -149.820007 -1847.829956 -0.046791 -0.416981 -0.907710 -0.722566 -0.613308 0.318987 -0.689717 0.670806 -0.272599

11797 0 0 inf inf inf inf inf inf inf inf inf inf inf inf
11797 2 1 -109.089996 -149.869995 -1847.050049 -0.041530 -0.410916 -0.910727 -0.724227 -0.615565 0.310766 -0.688310 0.672479 -0.272032

11798 0 0 inf inf inf inf inf inf inf inf inf inf inf inf
11798 2 1 -109.139999 -150.419998 -1846.500000 -0.056804 -0.420193 -0.905655 -0.721901 -0.609330 0.327987 -0.689661 0.672424 -0.268726

11799 0 0 inf inf inf inf inf inf inf inf inf inf inf inf
11799 2 1 -107.540001 -150.919998 -1845.439941 -0.058362 -0.418727 -0.906235 -0.713950 -0.616989 0.331059 -0.697761 0.666327 -0.262941

11800 0 0 inf inf inf inf inf inf inf inf inf inf inf inf
11800 2 1 -106.070000 -151.619995 -1844.979980 -0.054848 -0.418102 -0.906743 -0.712030 -0.620260 0.329074 -0.700003 0.663677 -0.263681

11801 0 0 inf inf inf inf inf inf inf inf inf inf inf inf
11801 2 1 -104.300003 -152.820007 -1845.459961 -0.063938 -0.418950 -0.905755 -0.706443 -0.622064 0.337600 -0.704876 0.661450 -0.256191
```

Figure 6.2: Log file relative to one of the non-valid acquisition.

Table 6.3: 'Validation 2' dataset.

Tot acquisitions	**402**
Not valid	2
With outliers	168
Without outliers	232

6.3 Errors quantification

The effectiveness of the algorithm is evaluated by comparing the real coordinate of the RPs with the computed ones, both for the case in which the algorithm was applied and not. The errors were evaluated at first considering their sign, thus knowing if the computed point was found in the proximal/distal or anterior/posterior direction. Then the following indicator:

- Mean Absolute Error (MAE)

$$\frac{1}{N}\sum_{N}|e| \tag{6.2}$$

- Root mean squared error (RMSE)

$$\left(\sum_{N}\frac{e^2}{N}\right)^2 \tag{6.3}$$

- Maximum Error

$$\max_{N} e \tag{6.4}$$

6.4 Data distribution

The distribution of the data is analysed before and after the application of the algorithm with histograms and with the Normal (Gaussian) Distribution Function relating to errors in acquisitions affected by outliers, providing the values of the mean (μ) and standard deviation (σ) of the samples.

Histograms are useful to give an approximate representation of the distribution of the errors and their frequency, through 1,5 mm wide intervals. The Normal Distribution Function describes the dispersion of the data and its equation is the following:

$$f(x) = \frac{1}{\sigma\sqrt{2\pi}}e^{\frac{-(x-\mu)^2}{2\sigma^2}} \tag{6.5}$$

where x is the variable (error expressed in mm). The distribution is symmetric about the mean value and the smaller the standard deviation, the higher is the peak value of $f(x)$ at the mean.

Chapter 7

Results

The present chapter presents the results obtained with the chosen model described in Chapter 5.1.8 applied both for the intra-operative dataset, 'validation 1', and 'validation 2'.

7.1 Intra-operative dataset

As regards the acquisitions which are supposed to be free of outliers, the algorithm returns a number of outliers equal to 0, thus indicating that with good registrations, the method does not alter the system performances (Figure 7.1).

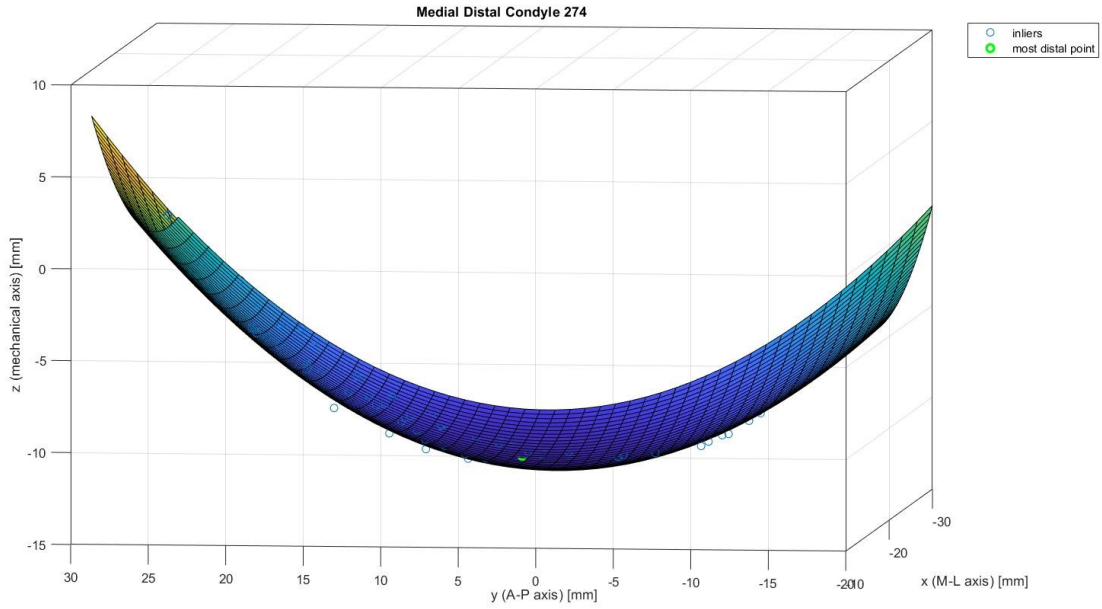

Figure 7.1: Model applied to a set of points with no errors: outliers are not found.

As regards the specific case affected by outliers, the algorithm highlights the presence of outliers in the region near the most distal point. A 2-D and 3-D representation of the acquired points and the results of the application of the algorithm is shown in Figure 7.2 and 7.3. The outliers found (red dots) have been deleted, finding a new most distal point

(green dot) which it is supposed to be closest to the right RP. The different planned cuts are represented in the 2-D plot, supposing a 9 mm thick cut starting from the distal end of the bone.

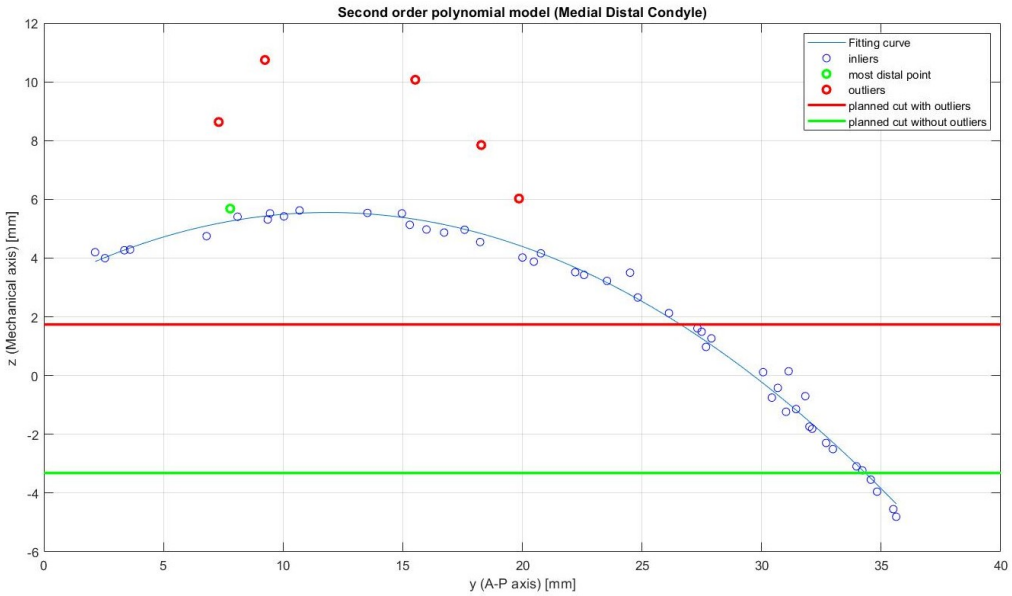

Figure 7.2: Application of the 2-D model to the real case affected by outliers. Blue dots represent the inliers; red dots are the outliers found; the red line is the planned cut considering all the acquired points; green dot is the new most distal point found after the application of the algorithm; the green line is the planned cut considering the outliers deletion; the blue fitting curve is the best inlier matching parabola.

7.2 Validation 1

The results are reported as a measure of the error between the computed RP coordinate along the principal axis (A-P for posterior condyles and mechanical axis for distal condyles and tibial plates) and the ideal one. As regards 'validation 1', the ideal coordinate is calculated as the average of the first twenty acquisitions, that were free of outliers. Errors are calculated before and after applying the algorithm, so that a comparison can be made. In the following plots (Figures 7.4, 7.5, 7.6, 7.7, 7.8 and 7.9), the errors are reported for each acquisition: the blue line represents the measure of the error without the application of the algorithm, while the pink line represents the error after the RANSAC algorithm has deleted the outliers. An ideal situation is represented with a green line, constantly null, which means that the coordinate of the RP is equal to the averaged good coordinates. In the figures, there is evidence that the first acquisitions are good, since the errors are close to zero, both before and after applying the algorithm. In all the graphs, the blue line represents the errors computed without the application of the filtering algorithm; the pink line represents the errors computed after the removal of the outliers with the RANSAC algorithm; the green line represents the ideal situation.

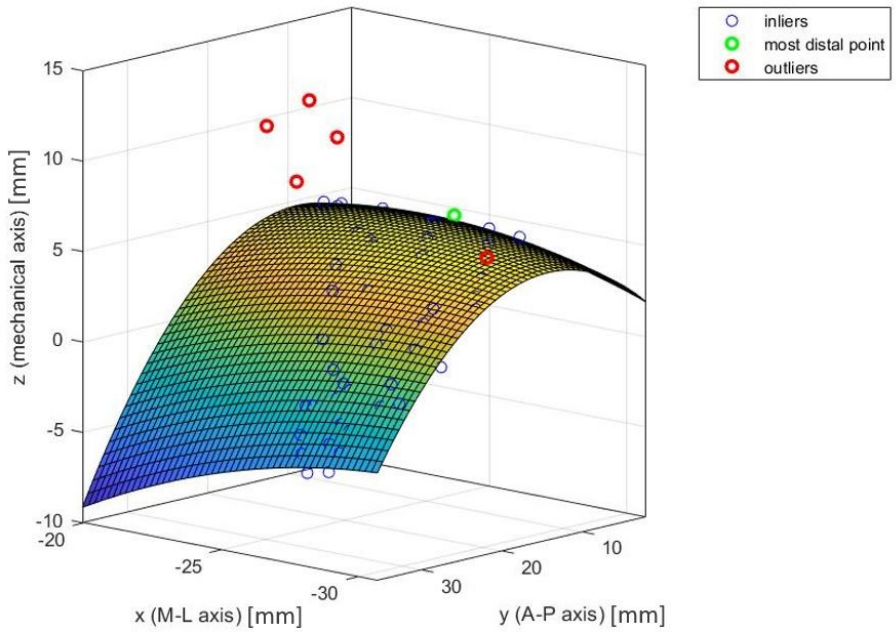

Figure 7.3: Application of the 3-D model to the real case affected by outliers. Blue dots represent the inliers; red dots are the outliers found; green dot is the new most distal point found after the application of the algorithm; the fitting surface is the best inlier matching paraboloid.

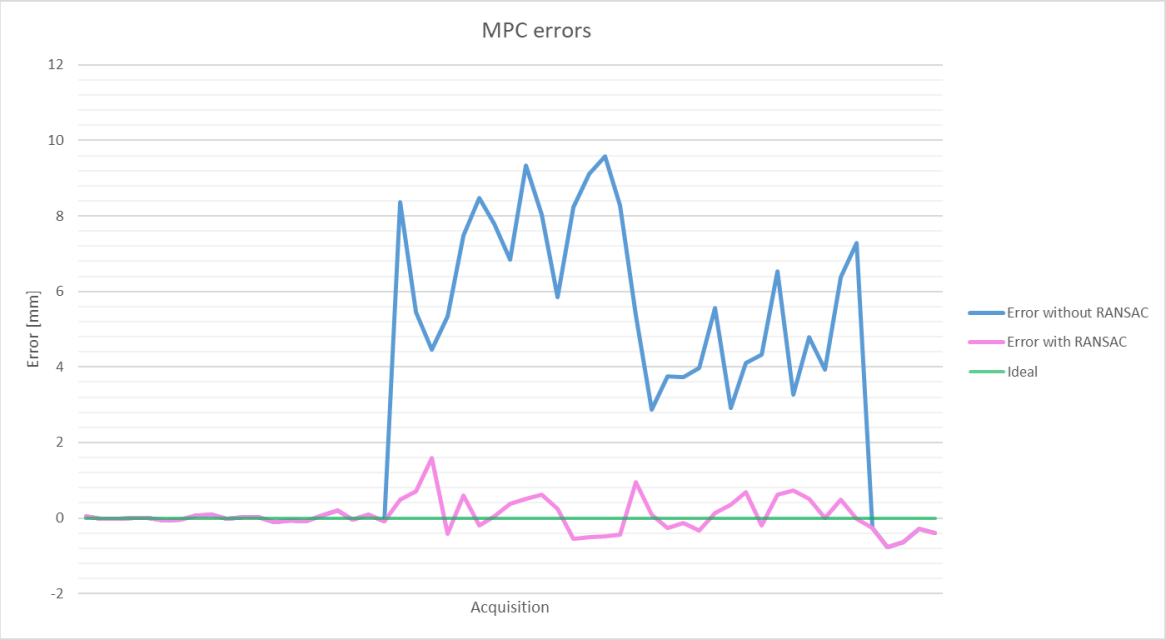

Figure 7.4: Errors in the acquisitions of the Medial Posterior Condyle (MPC).

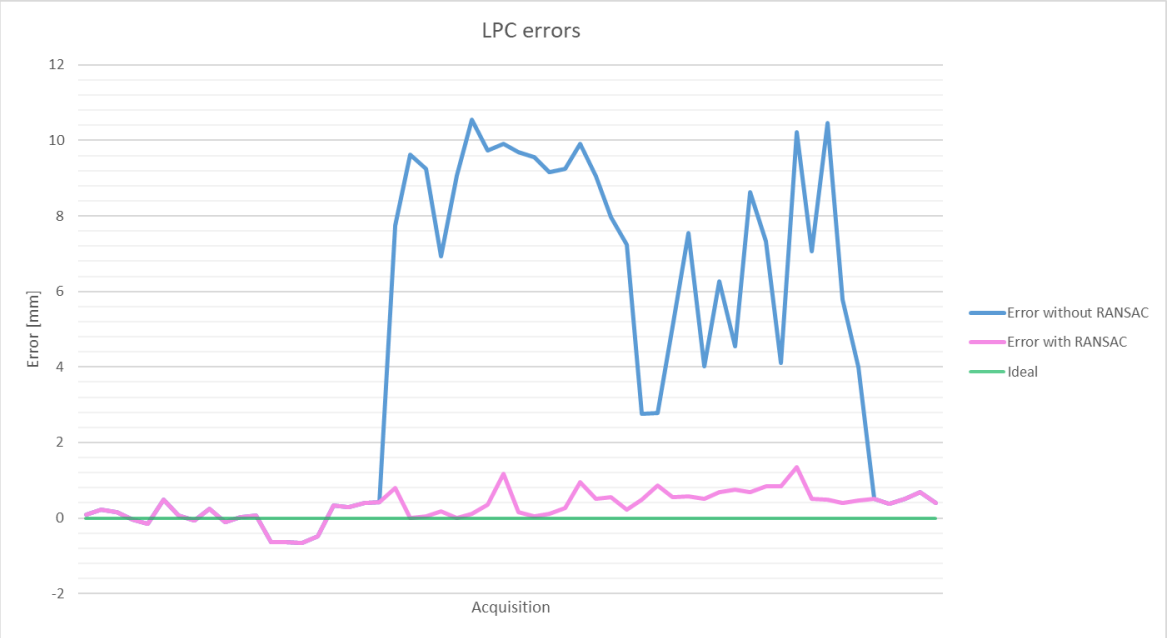

Figure 7.5: Errors in the acquisitions of the Lateral Posterior Condyle (LPC).

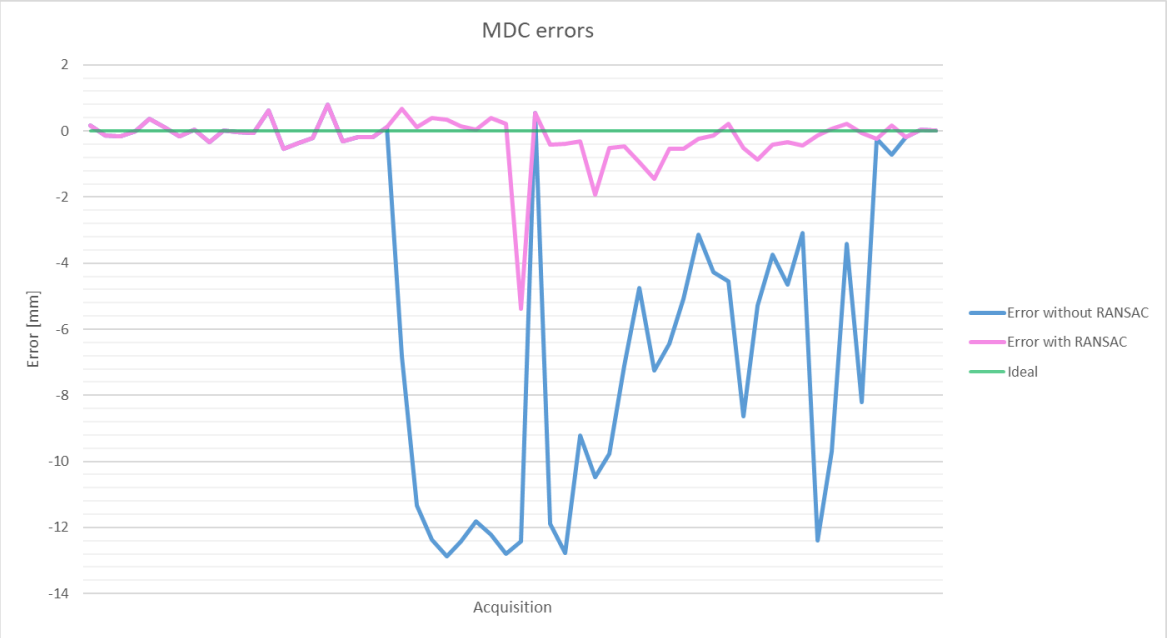

Figure 7.6: Errors in the acquisitions of the Medial Distal Condyle (MDC).

Making an overall analysis, the plots show high values in the blue line for errors relative to the acquisitions with outliers (after the reference vertical line) that are not filtered with RANSAC. The reduction in errors' values as a result of the application of RANSAC is tangible (the difference between the blue and pink line). The first twenty acquisitions are characterized by low errors, equal in both the cases, that means that RANSAC does not make any changes in good acquisitions.

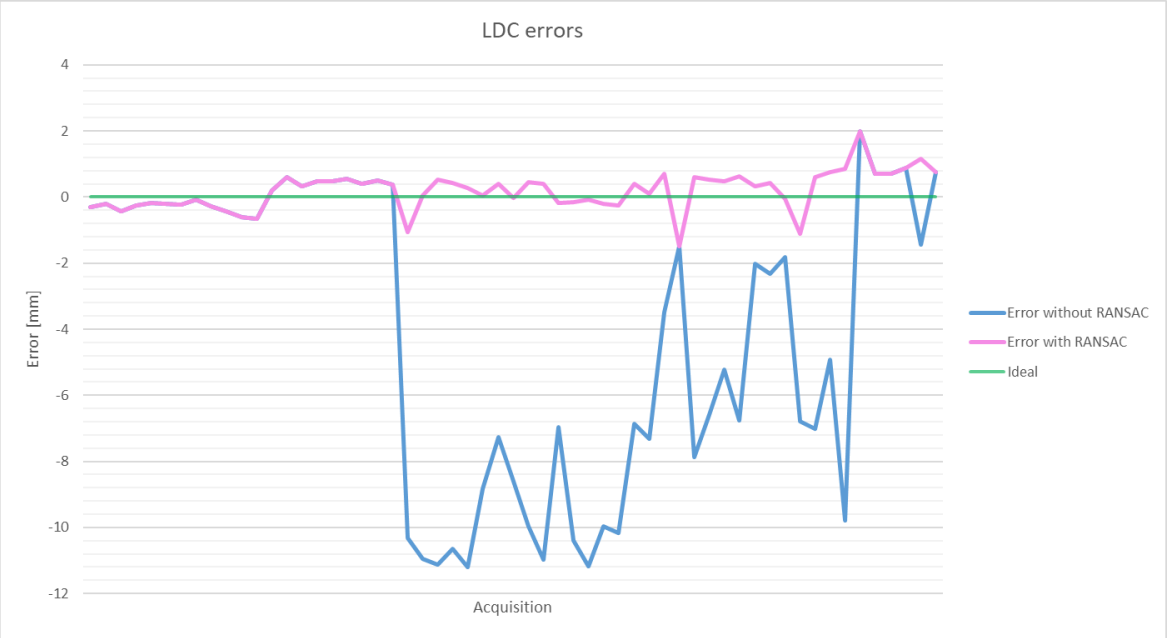

Figure 7.7: Errors in the acquisitions of the Lateral Distal Condyle (LDC).

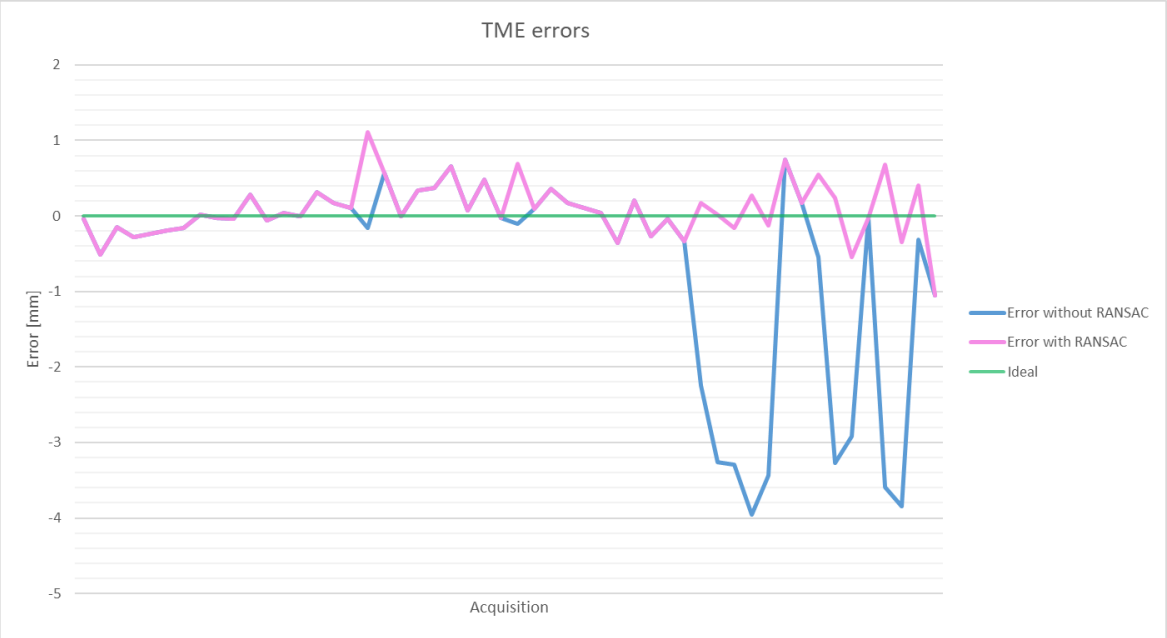

Figure 7.8: Errors in the acquisitions of the Tibial Medial Emiplateau (TME).

For the posterior compartments (Figures 7.4 and 7.5) the last acquisitions do not show differences between applying or not the algorithm, so the errors' values are coincident. These samples are all characterized by an acquisition made sliding sideways with the probe. As regards the medial compartments, most of the errors have negative values due to the RS in left limbs with the mechanical axis oriented proximally. In one case the error after the application of the algorithm in MDC is still high (5,37 mm in absolute value), but

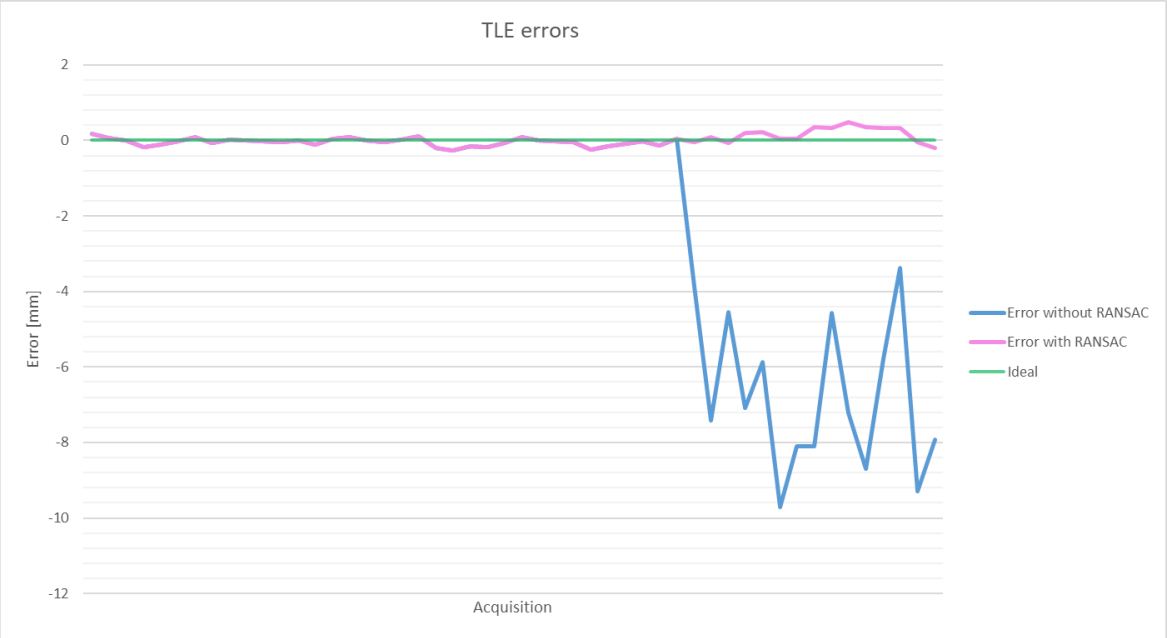

Figure 7.9: Errors in the acquisitions of the Tibial Lateral Emiplateau (TLE).

lower than the correspondent error without RANSAC (12,4 in absolute value).
As regards the tibial compartments, results are shown in Figures 7.8 and 7.9, where it can be noticed that many kinds of acquisitions do not provide high errors even without RANSAC (blue line). In this case, it is more difficult for the surgeon to acquire wrong points, because of the anatomy of the tibia, that is slightly convex. The RP to be identified by the software is the most distal one, and it is rare that the probe goes distally in that area. This situation only occurs when there is a sliding down movement.

Tables 7.1 and 7.2 show MAE, RMSE, and the maximum error respectively divided for all the compartment analysed and globally for all the compartments.

The distribution of the data is analysed with histograms and the Normal (Gaussian) Distribution Function showed in Figures 7.10, 7.11, 7.12, 7.13, 7.14, 7.15.

Errors after the RANSAC application (Figure 7.10) are distributed around zero, showing high frequencies for low values of the errors ($|e| < 1,5$ mm) and very low frequencies for high errors ($|e| > 1,5$ mm).

Before the application of the algorithm (Figure 7.11) there is a wider distribution of the errors, showing higher errors committed.

The difference in the distribution of the errors comparing the two histograms (Figure 7.12) is substantial: without RANSAC, the occurrences with $|e| < 1,5$ mm) are much less compared with the ones relative to the filtering algorithm applied and the occurrences with $|e| > 1,5$ mm are more frequent if RANSAC is not applied.
Figure 7.13 shows the Gaussian Distribution of the errors after the application of the algorithm. The bell is centred in the mean value, which is close to zero, and the distribution is tighter if we compare it with the distribution in Figure 7.14, relative to the errors without

Table 7.1: MAE, RMSE and Maximum values of the acquisitions relative to 'validation 1'.

		MAE [mm]	**RMSE [mm]**	**Max error [mm]**
MPC	*RANSAC*	0,45±0,30	0,54	1,59
	No filter	5,35±2,75	5,91	9,57
LPC	*RANSAC*	0,50±0,32	0,59	1,35
	No filter	6,60±3,28	7,37	10,55
MDC	*RANSAC*	0,53±0,87	1,02	5,37
	No filter	6,75±4,50	8,11	12,88
LDC	*RANSAC*	0,55±0,42	0,69	1,98
	No filter	6,54±3,69	7,50	11,21
TME	*RANSAC*	0,32±0,25	0,40	1,05
	No filter	1,17±1,41	1,83	3,96
TLE	*RANSAC*	0,16±0,12	0,20	0,48
	No filter	3,44±3,60	4,98	9,71

Table 7.2: MAE, RMSE, and Maximum values of the overall acquisitions relative to 'validation 1'.

	RANSAC	*No filter*
MAE [mm]	0,43±0,48	5,14±3,93
RMSE [mm]	0,51	5,14
Max error [mm]	5,37	12,88

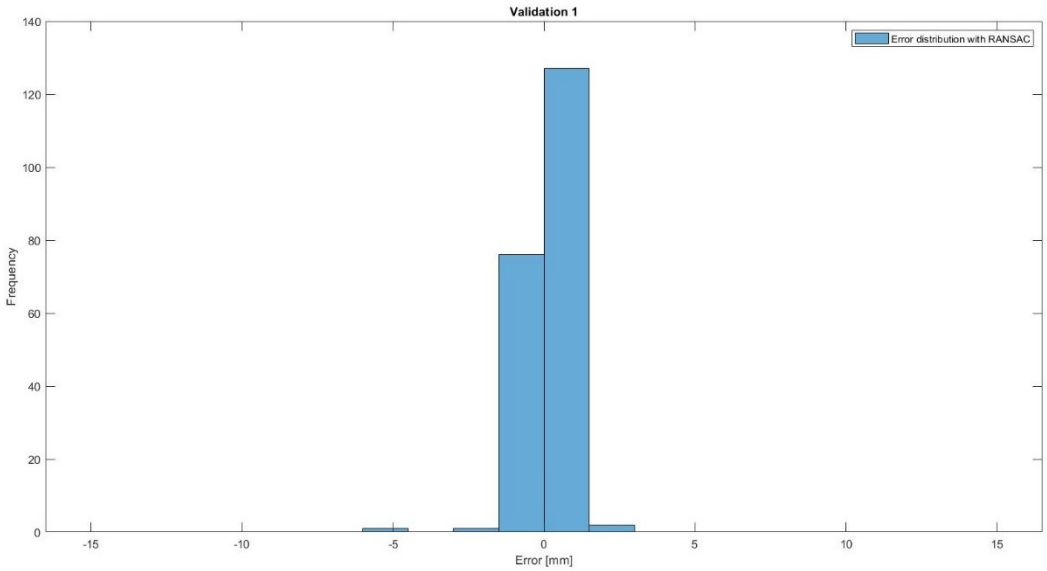

Figure 7.10: Histogram representing the distribution of the errors after the application of RANSAC algorithm.

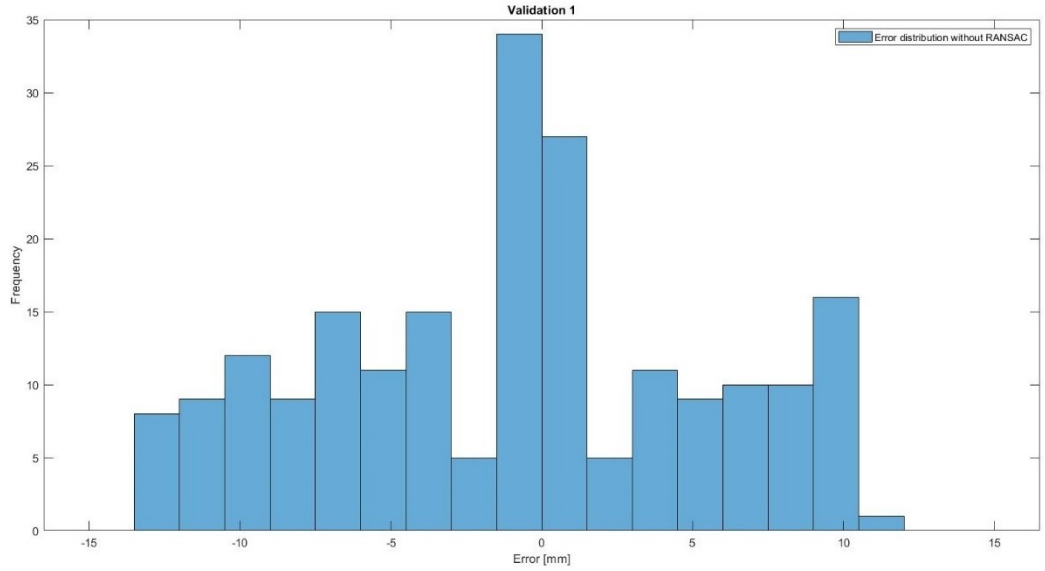

Figure 7.11: Histogram representing the distribution of the errors with no filtering algorithm applied.

the application of the algorithm. The two distribution are compared in Figure 7.15.

μ and σ are reported in Table 7.3.

7.3 Validation 2

Results for 'validation 2' are reported in the same way of 'validation 1', by comparing the errors between the entire data set and the filtered one. The ideal situation (green line in the following plots) is now computed as the average of the RP coordinate along the

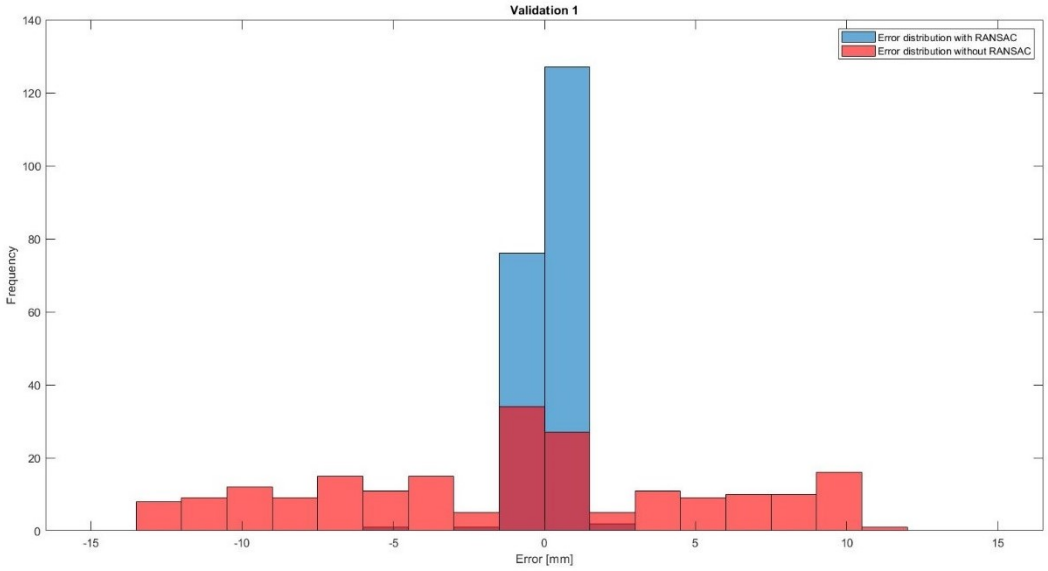

Figure 7.12: Distribution of the errors compared between the two cases: with the application of the algorithm (blue) and without the application of the algorithm (red).

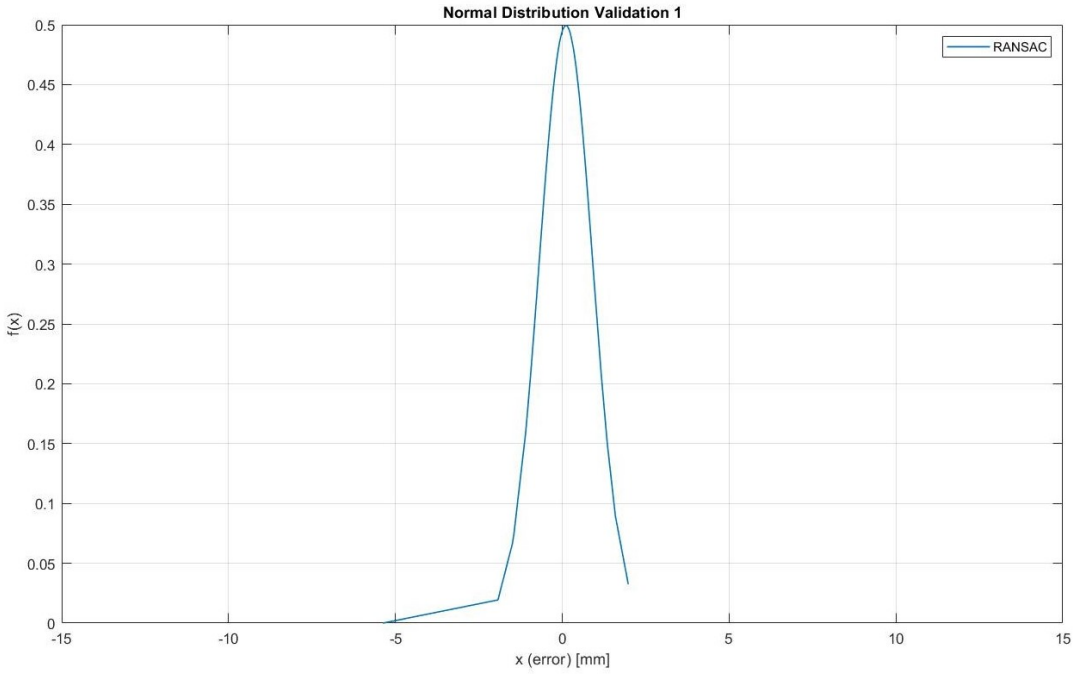

Figure 7.13: Normal Distribution Function after the application of the algorithm.

principal axis for the last five acquisitions (after the reference vertical line), which were free of outliers. Figures 7.16, 7.17, 7.18, 7.19, 7.20 and 7.21 represent the obtained results for each acquisition, divided for the different operators (Operator 1, Operator 2, Operator 3) and from the last five good acquisitions (Reference).

In the graphs representing the errors, the blue line represents the errors computed

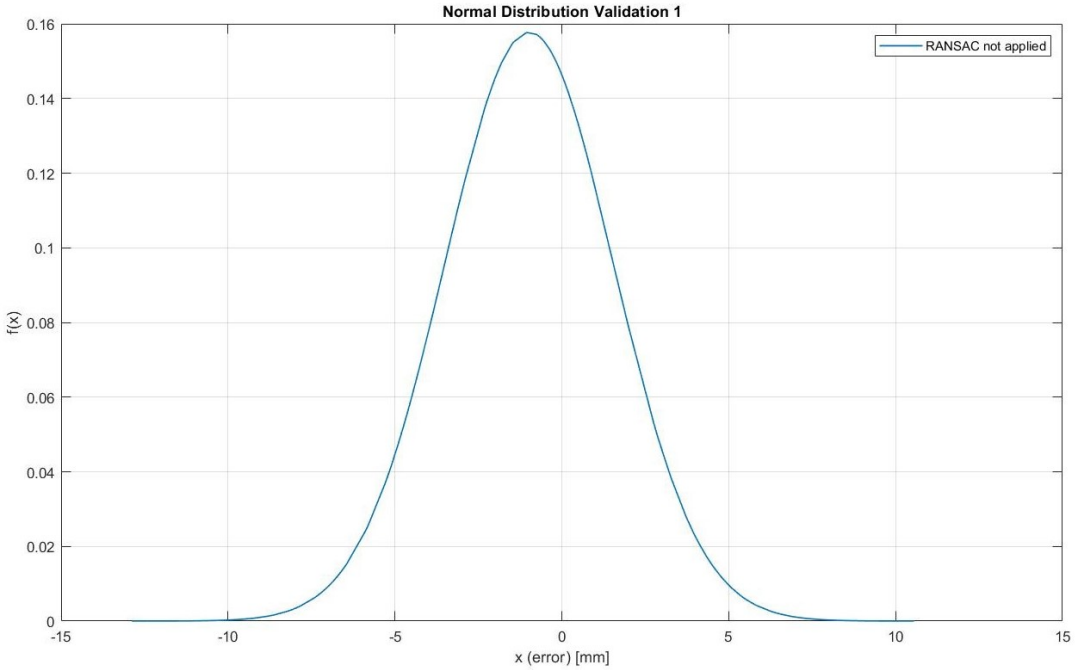

Figure 7.14: Normal Distribution Function without the application of RANSAC.

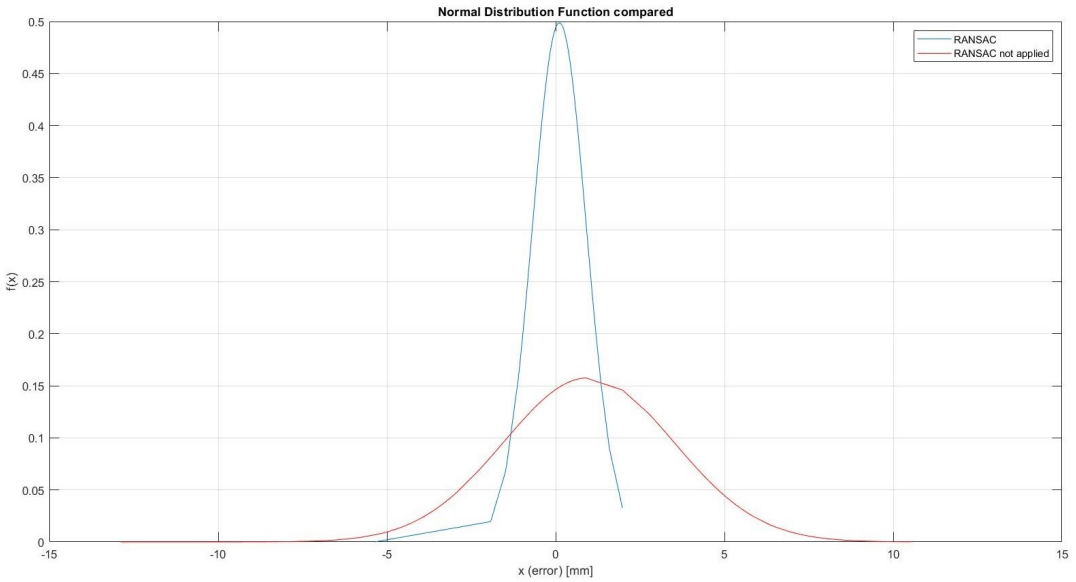

Figure 7.15: Normal distribution function compared when RANSAC is applied and not.

without the application of the filtering algorithm; the pink line represents the errors computed after the removal of the outliers with the RANSAC algorithm; the green line represents the ideal situation.

The plots show some peaks in the blue line which belong to the acquisitions with outliers. The correspondent value of the pink line is most of the time lower, thus determining the improvement in the system's performances after the application of the algorithm. In some acquisitions, the error continues to be higher despite the application of the RANSAC

Table 7.3: Mean value and standard deviation for 'validation 1', comparing the two models (with and without RANSAC).

Validation 1	*RANSAC*	*No filter*
μ [mm]	0,11	0,98
σ	0,64	6,39

algorithm, that does not bring any correction. In the remaining cases, the difference in the trend is easily appreciable.

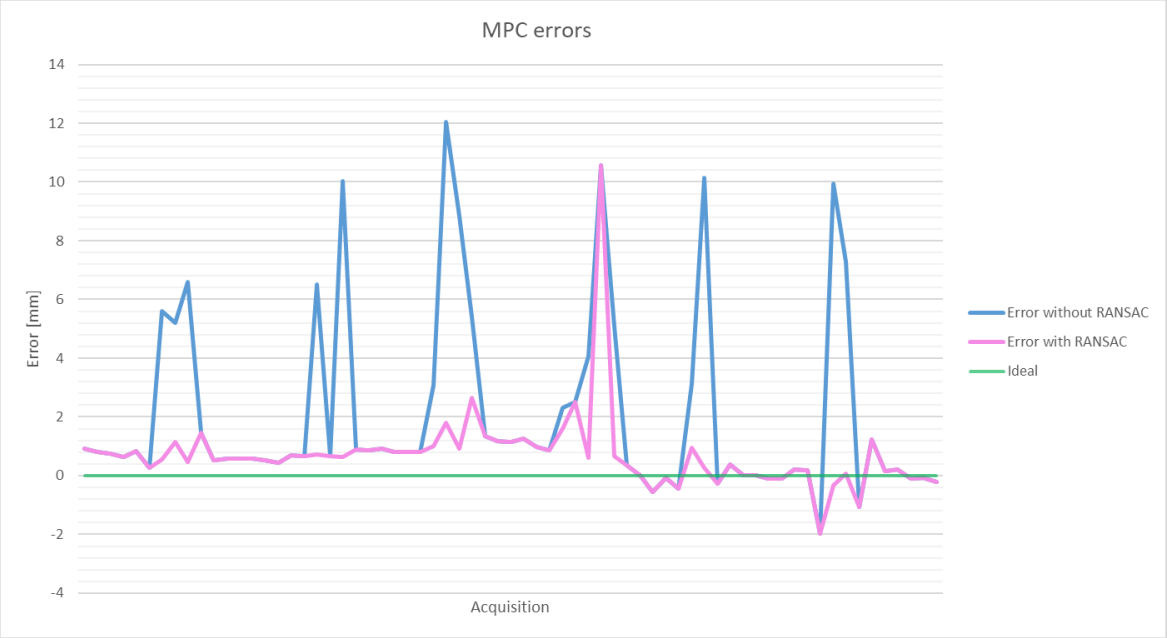

Figure 7.16: Errors in the acquisitions of the Medial Posterior Condyle (MPC).

Table 7.4 and 7.5 show MAE, RMSE, and the maximum error respectively divided for all the compartment analysed and globally for all the compartments.

The distribution of the data is represented, as for 'validation 1', with histograms and the Normal (Gaussian) Distribution Function showed in Figures 7.22, 7.23, 7.24, 7.25, 7.26, 7.27.

The histograms show again a wider distribution of the errors with no filtering algorithm applied, with respect to the errors after the application of RANSAC. The frequencies of $|e| < 1,5$ mm in Figure 7.22 are higher than the ones obtained in Figure 7.23. The histograms compared show the improvement induced by the algorithm (Figure 7.24).

The Normal Distribution Functions are showed in Figures 7.25, 7.26 and 7.27. In this case, the difference between the two bells is not so evident as the 'validation 1' set (see a comparison in Figure 7.15).

μ and σ are reported in Table 7.6.

Table 7.4: MAE, RMSE and Maximum values of the acquisitions relative to 'validation 2'.

		MAE [mm]	**RMSE [mm]**	**Max error [mm]**
MPC	*RANSAC*	1,31±1,96	2,35	10,57
	No filter	4,80±3,64	6,03	12,04
LPC	*RANSAC*	1,97±1,73	2,62	9,89
	No filter	3,31±2,81	4,34	10,54
MDC	*RANSAC*	1,16±1,57	1,95	8,67
	No filter	3,18±3,21	4,52	10,13
LDC	*RANSAC*	1,15±1,43	1,84	7,24
	No filter	3,53±2,86	4,54	8,76
TME	*RANSAC*	0,62±0,60	0,86	1,97
	No filter	1,05±0,92	1,40	2,60
TLE	*RANSAC*	0,67±1,13	1,31	5,97
	No filter	2,37±2,97	3,80	8,68

Table 7.5: MAE, RMSE, and Maximum values of the overall acquisitions relative to 'validation 2'.

	RANSAC	*No filter*
MAE [mm]	1,14±1,53	3,02±3,07
RMSE [mm]	1,28	2,90
Max error [mm]	10,57	12,04

Table 7.6: Mean value and standard deviation for 'validation 2', comparing the two models (with and without RANSAC).

Validation 2	*RANSAC*	*No filter*
μ [mm]	0,43	-0,22
σ	1,86	4,31

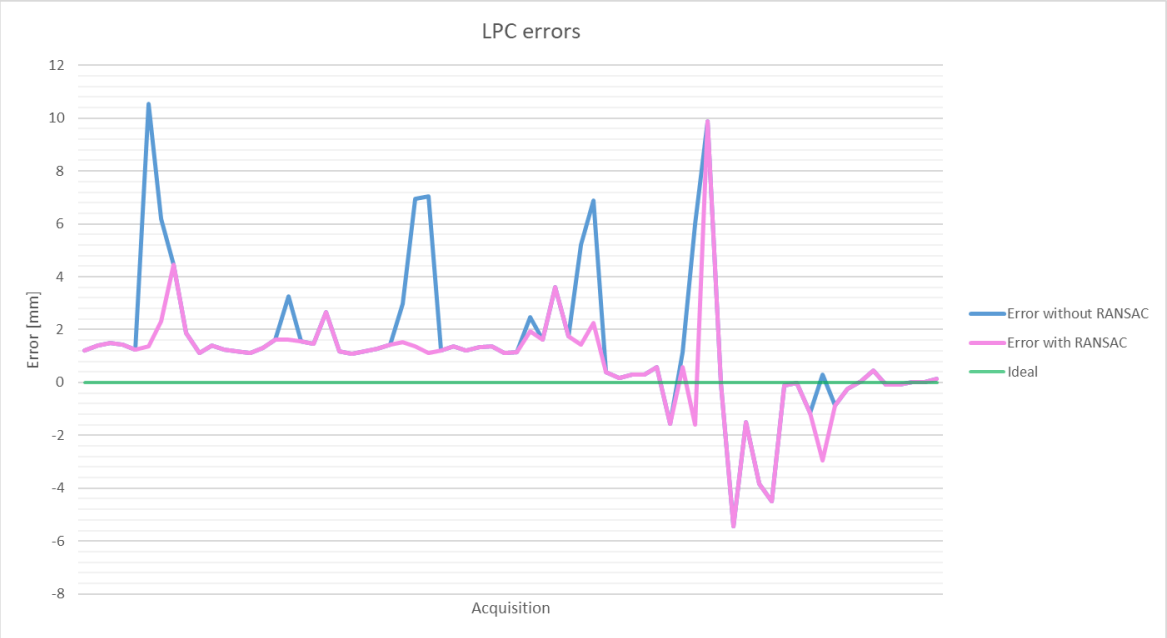

Figure 7.17: Errors in the acquisitions of the Lateral Posterior Condyle (LPC).

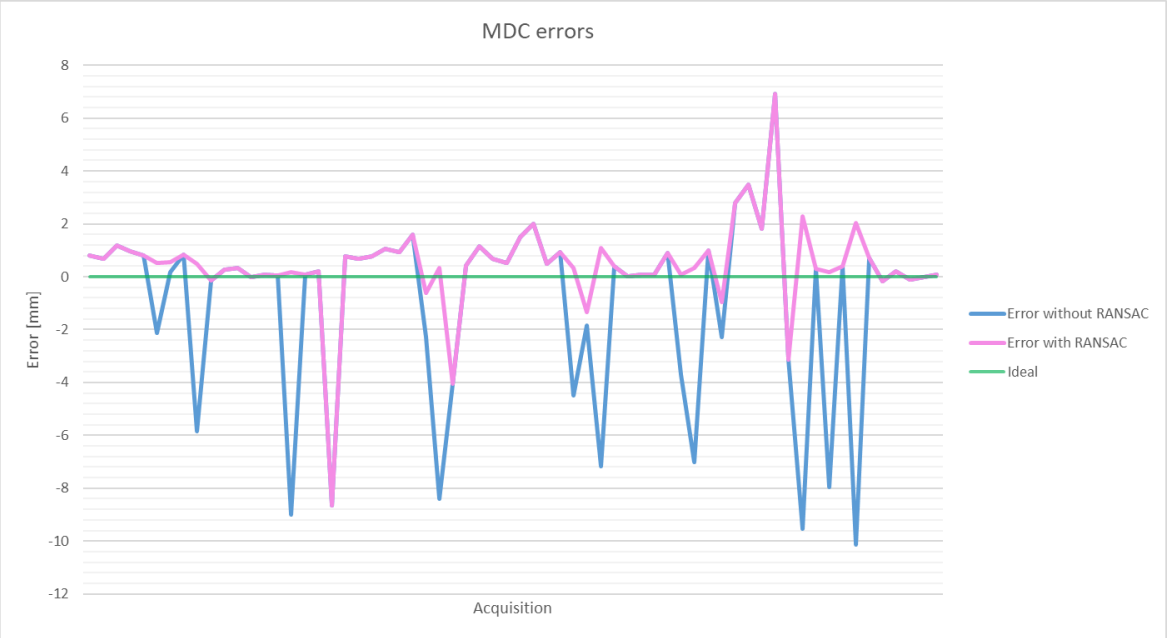

Figure 7.18: Errors in the acquisitions of the Medial Distal Condyle (MDC).

7.4 Computational costs

A factor to consider in the assessment of the algorithm is certainly the computational cost. An algorithm that works with optimal results, but taking a long time, is not a good algorithm. Surgeons in the operating room do not want to wait for minutes to get the perfect cut planning, because any waste of time has implication in the costs of the intervention, possibility to run into complications and loss of concentration of the surgical

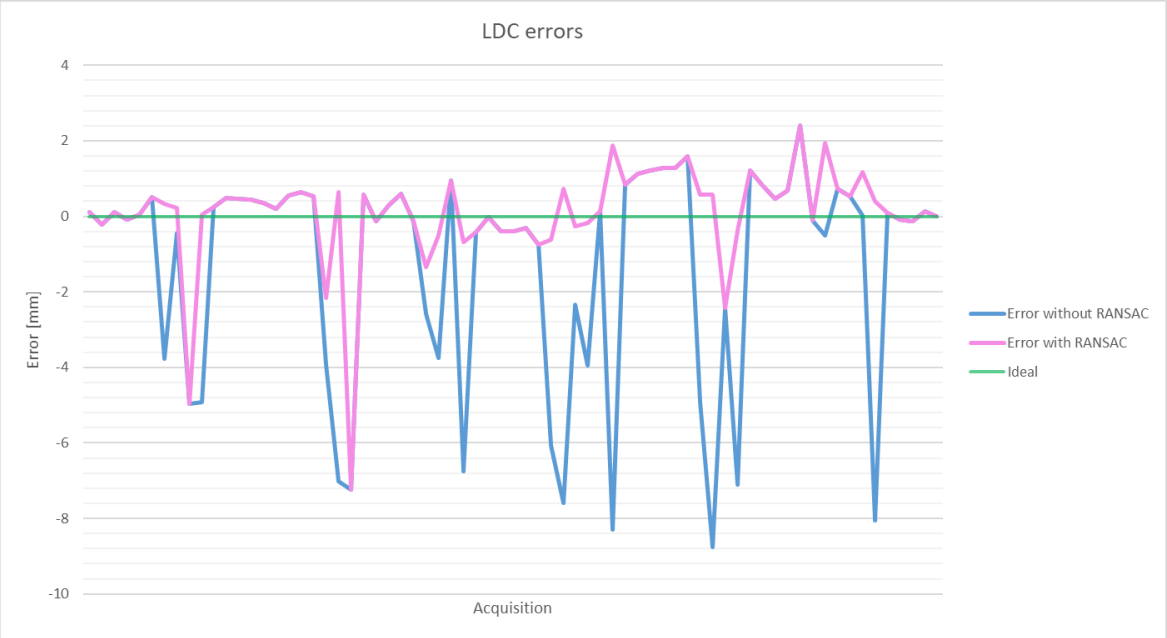

Figure 7.19: Errors in the acquisitions of the Lateral Distal Condyle (LDC).

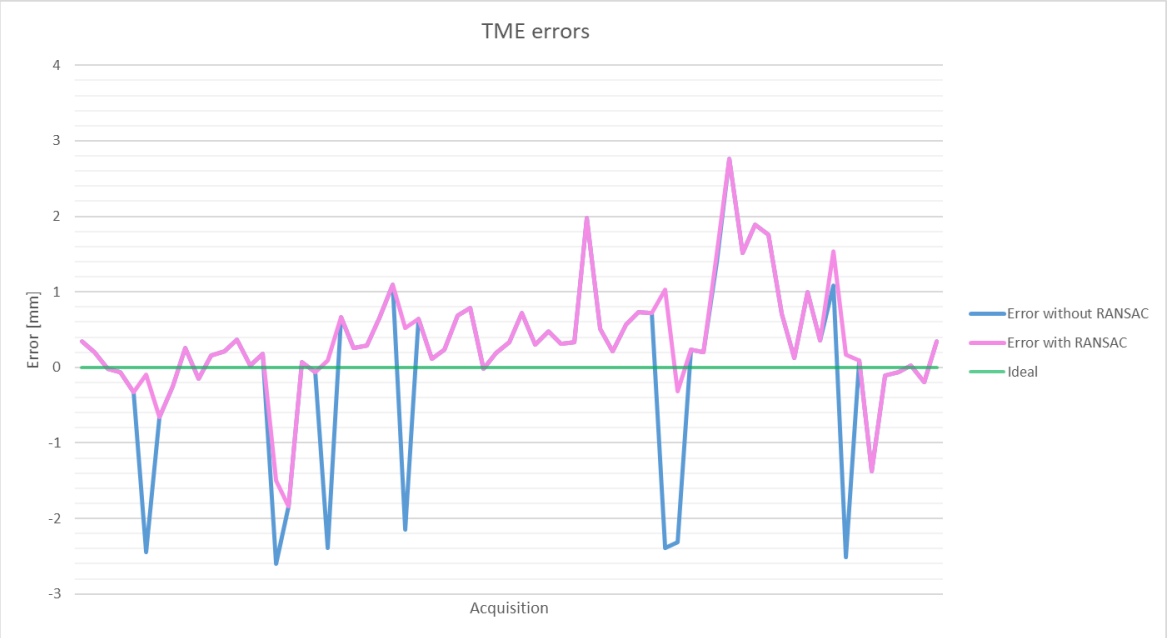

Figure 7.20: Errors in the acquisitions of the Tibial Medial Emiplateau (TME).

team, that is involved in long lasting surgeries. A good compromise between good results and short computational time is what makes a successful algorithm.
The computational times in C++ have been tested, considering different cases:

- the dataset is free of outliers or not
- the debug/release version

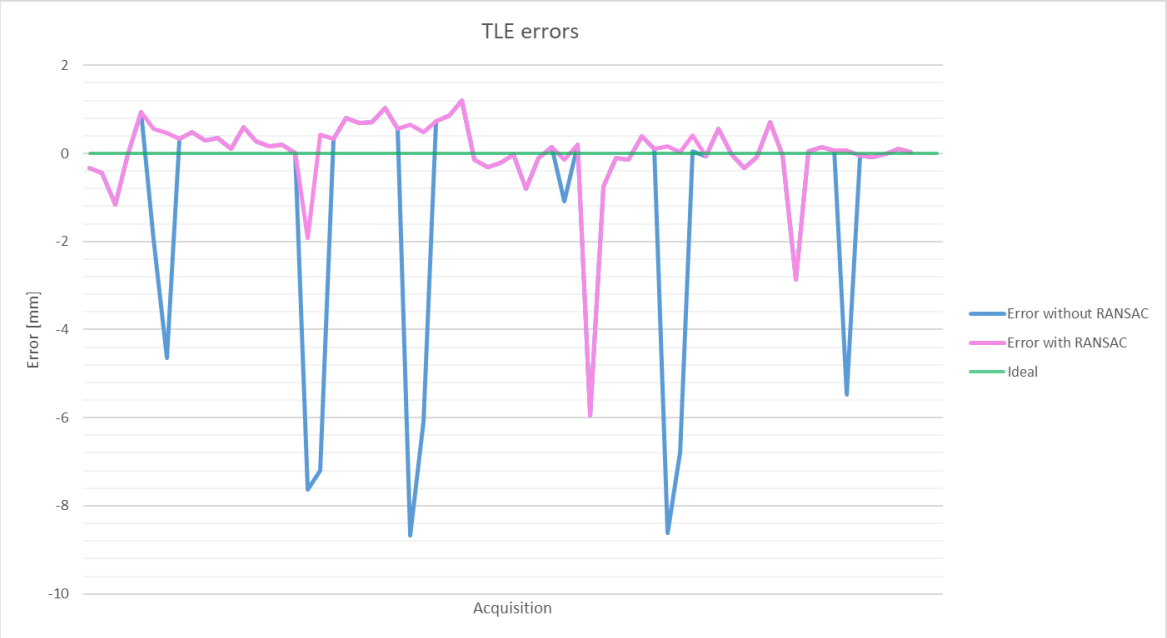

Figure 7.21: Errors in the acquisitions of the Tibial Lateral Emiplateau (TLE).

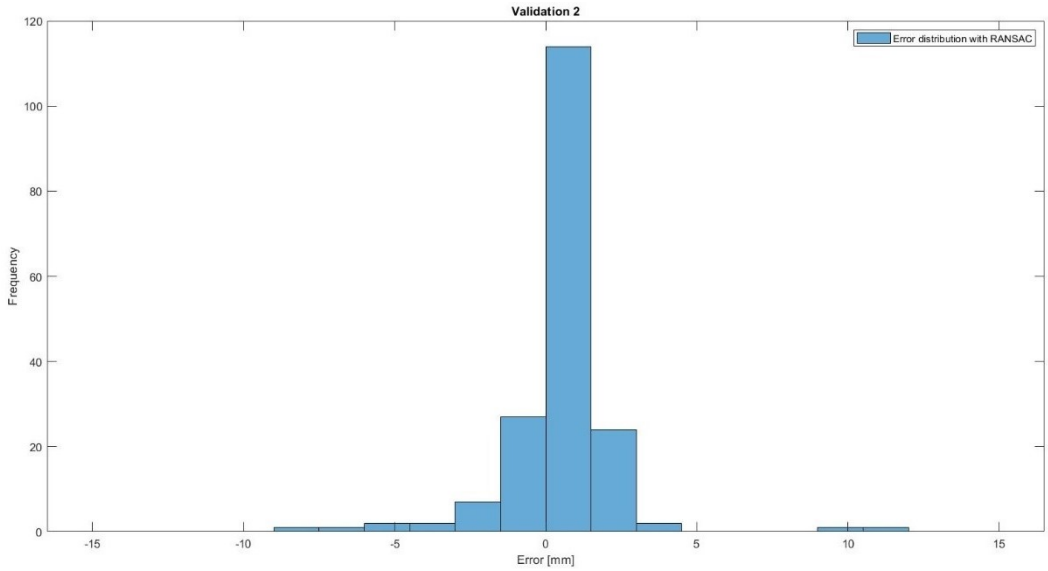

Figure 7.22: Histogram representing the distribution of the errors after the application of RANSAC algorithm.

- 2-D/3-D model

A summary of these conditions is given in Table 7.7.

Table 7.7: Computational times relative to the different situations in which the RANSAC algorithm is applied.

	Algorithm passages	Iterations	Computational time
3-D	The acquisition does not contain outliers, so the algorithm finds the surface which returns 0 outliers in a few iterations.	<5	t=19.87 ms
	The acquisition contains outliers and the algorithm cannot find a 3-D surface with the desired convexity, so both the iterations with the 3-D model and 2-D model are completed.	40+40	t=31.54 ms
	The acquisition contains outliers, so all the 40 iterations relative to the 3-D model are completed.	40	t=23.29 ms
2-D	The acquisition does not contain outliers, so the algorithm finds the curve which returns 0 outliers in a few iterations.	<5	t=18.03 ms
	The acquisition contains outliers, so all the 40 iterations relative to the 2-D model are completed.	40	t=30.17 ms

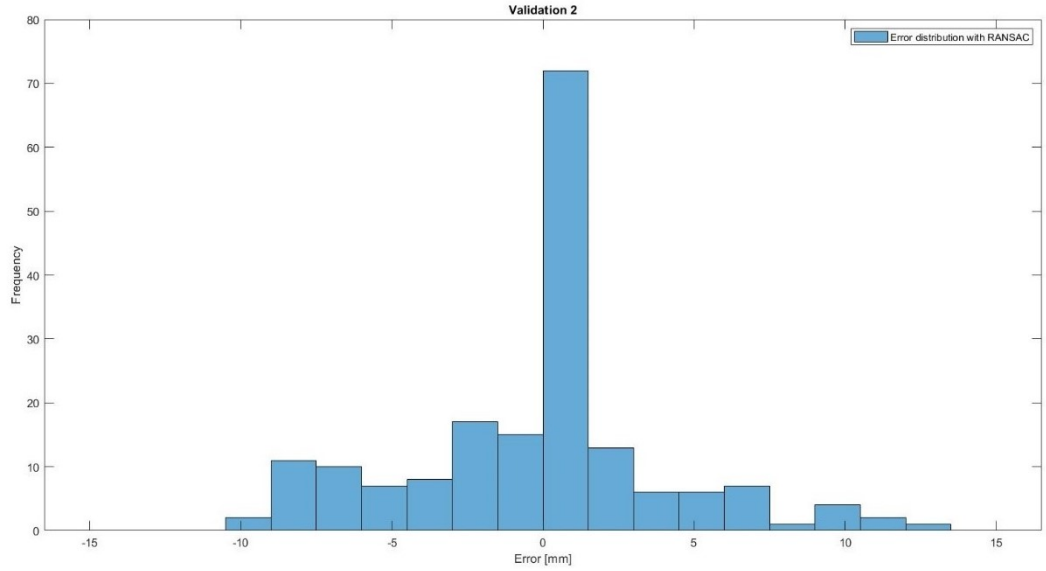

Figure 7.23: Histogram representing the distribution of the errors with no filtering algorithm applied.

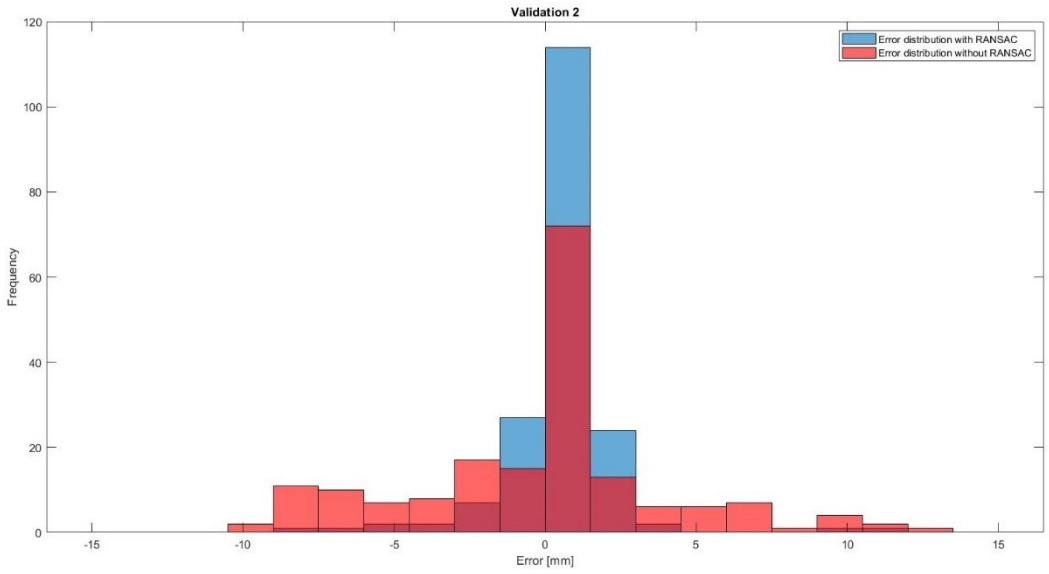

Figure 7.24: Distribution of the errors compared between the two cases: with the application of the algorithm (blue) and without the application of the algorithm (red).

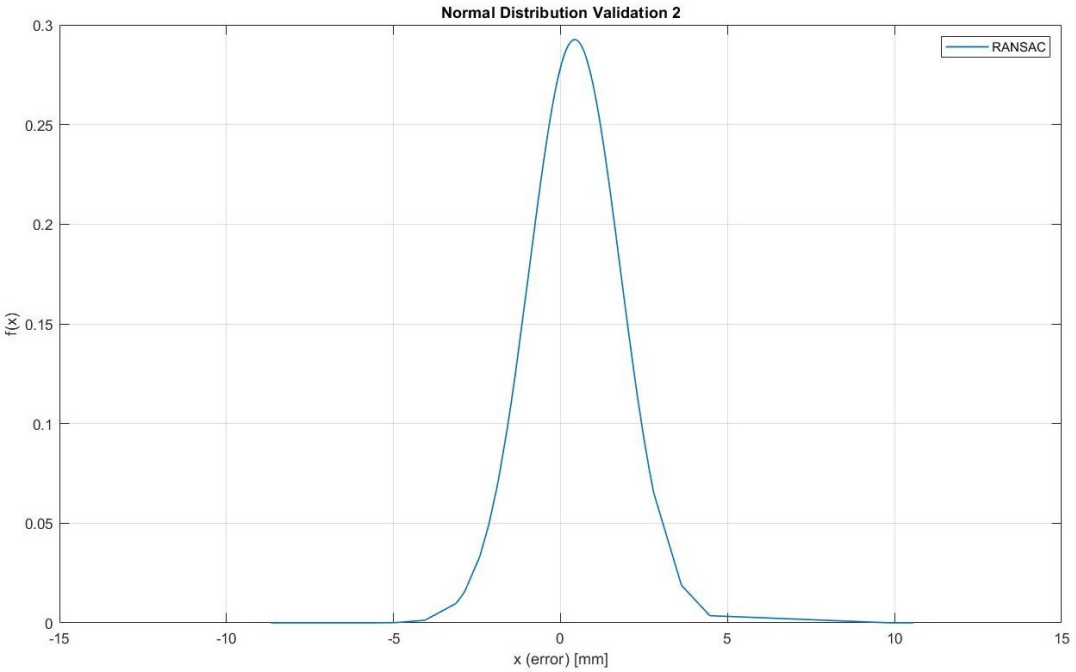

Figure 7.25: Normal Distribution Function after the application of the algorithm.

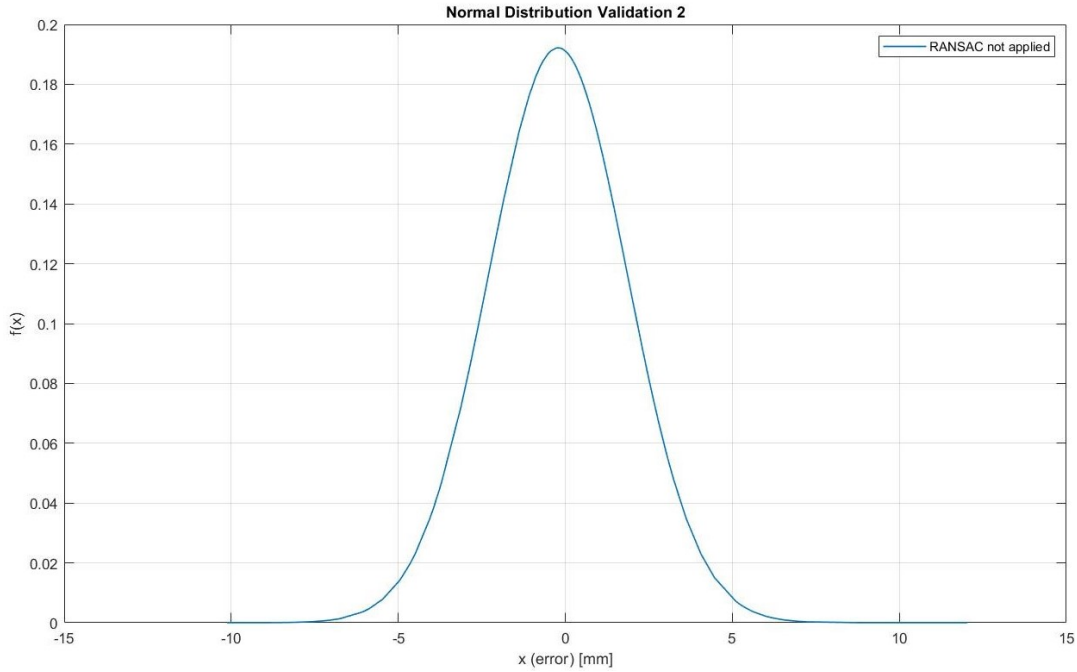

Figure 7.26: Normal Distribution Function without the application of RANSAC.

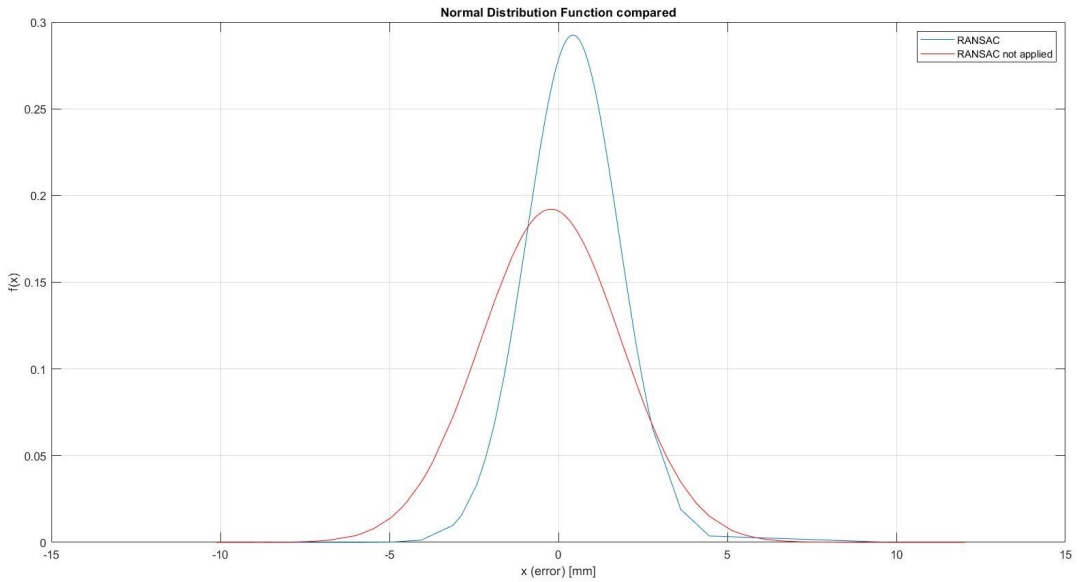

Figure 7.27: Normal Distribution Function compared with RANSAC and not.

Chapter 8

Discussion

8.1 Validation 1

The results relative to 'validation 1' show conspicuous differences between the application of the RANSAC algorithm and considering all the acquired data, without any deletion: by filtering the outliers, the errors decrease in most of the cases, leading to better results.
Without RANSAC, errors higher than 1,5 mm occur 147 times (73% over the total number of acquisitions affected by outliers) and appear to be reduced to 6 (2% over the total number of acquisitions affected by outliers) after the application of the algorithm, showing a 97% decrease. These six cases have been examined: four of them show an improvement in the performances of the system, since the errors decrease even if they still continue to be higher than 1,5 mm; in two cases the error does not change its value by comparing it before and after the application of the algorithm.
Sometimes, despite the improvements, the errors after the execution of RANSAC are still far from the ideal situation, but better than the previous though. In a few cases, the filtered result is worse than the result that is obtained without the application of RANSAC. To quantify the improvement/worsening, which is determined by this method, Δ (see Chapter 6) is computed: Table 8.1 shows the results for positive and negative Δ divided for compartment.

Δ is negative in 3 cases, showing a difference between the errors that is less than 1 mm:

$$|\Delta_1| = 0,96mm \tag{8.1}$$

$$|\Delta_2| = 0,59mm \tag{8.2}$$

$$|\Delta_3| = 0,10mm \tag{8.3}$$

All these 3 cases are relative to the Tibial Medial Emiplateau.
In 147 cases (73%), Δ is positive and in 145 cases (72%) the improvements are substantial, since $\Delta > 1,5$ mm.

The results obtained with 'validation 1', must be compared with the second blind validation, in order to better comprehend the effectiveness of the proposed method.

Table 8.1: Distribution of the positive and negative Δ in Validation 1

TOT	**MP**	**LP**	**MD**	**LD**	**TM**	**TL**	
147	30	31	32	30	9	15	$\Delta > 0$
3	0	0	0	0	3	0	$\Delta < 0$

Table 8.2: Distribution of the positive and negative Δ in Validation 2

TOT	**MP**	**LP**	**MD**	**LD**	**TM**	**TL**	
75	16	11	14	17	7	10	$\Delta > 0$
7	0	1	1	2	2	1	$\Delta < 0$

8.2 Validation 2

In this validation, the results show a different trend with respect to 'validation 1'. At first glance, the errors computed after the application of the RANSAC algorithm are higher than the previous ones, thus indicating a difference between blinded and non-blinded tests and between different operators.
Without RANSAC, errors higher than 1,5 mm occur 111 times (66% with respect to the total number of acquisitions affected with outliers) and appear to be reduced to 57 (34% with respect to the total number of acquisitions affected with outliers) after the application of the algorithm, showing a 49% decrease. Despite the filtering applied, the number of acquisitions with large error is still high.

The computation of Δ confirms that the results for 'validation 2' are noisier than the previous ones (see Table 8.2 for the results divided for compartment):

- Δ is positive for 75 cases (45% on the total number of acquisitions affected by outliers)
  - Substantial improvement ($\Delta > 1,5$) for 69 cases
- Δ is negative for 7 cases (4% on the total number of acquisitions affected by outliers)
  - Substantial worsening ($\Delta < -1,5$) for 1 case
- Δ is zero for the remaining cases

The highest negative value for Δ is relative to the Lateral Posterior Condyle ($|\Delta| = 2,66$).

The pie charts in Figure 8.1 and 8.2 show the mistakes made by the algorithm and their percentage with respect to all the acquisitions.

- Figure 8.1 shows the samples in which the acquisitions were affected by outliers
  - in 154 cases (92%) the outliers were found

  - in 14 cases (8%) the surface fits the outliers, which are not identified by the algorithm

- Figure 8.2 shows the samples in which the acquisition was good (with no outlier recorded during the registration phase)
  - in 226 cases (97%) the outliers were not found
  - in 6 cases (3%) some outlier was found, but not in the critical area: most of the time, this situation occurs when the acquisition area is particularly wide, and the fitting model does not cover the entire surface described by the points cloud. This leads to a high computed distance between the model and the most marginal points, which are classified as outliers. This is not a big issue, since these points are far from the RP to be identified.

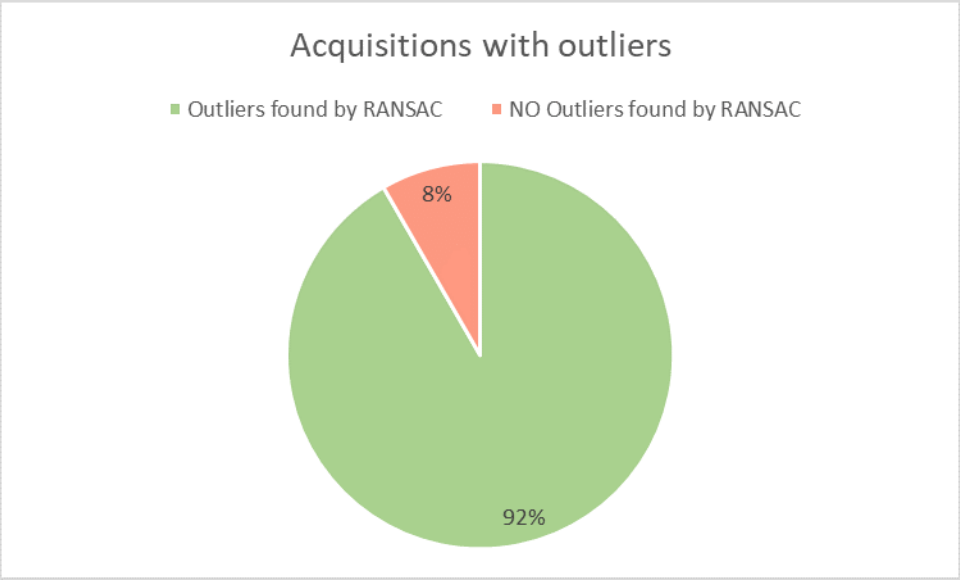

Figure 8.1: Pie chart relative to the acquisitions affected by outliers.

Since the gap between 'validation 1' and 'validation 2' is considerable, a deep study of this second test has been carried out, examining in detail every acquisition. In particular, the attention has been focused on all the cases which report high errors ($|e_{RANSAC}| > 1,5mm$) after the application of the algorithm, excluding the occurrences in which $|e_{nonRANSAC}|$ is much higher than $|e_{RANSAC}|$, which, however, remains greater than 1,5 mm. The critical situation involves 32 acquisitions that have been analysed:

- in 6 cases the algorithm deletes most of the outliers, but not all of them: the unrecognized outliers are then identified as RPs, giving high errors even with the application of the algorithm;

- in 6 cases the model fits the outliers, thus finding mistaken RPs, even if they are few in comparison with the total number of acquisitions: this is the most critical situation;

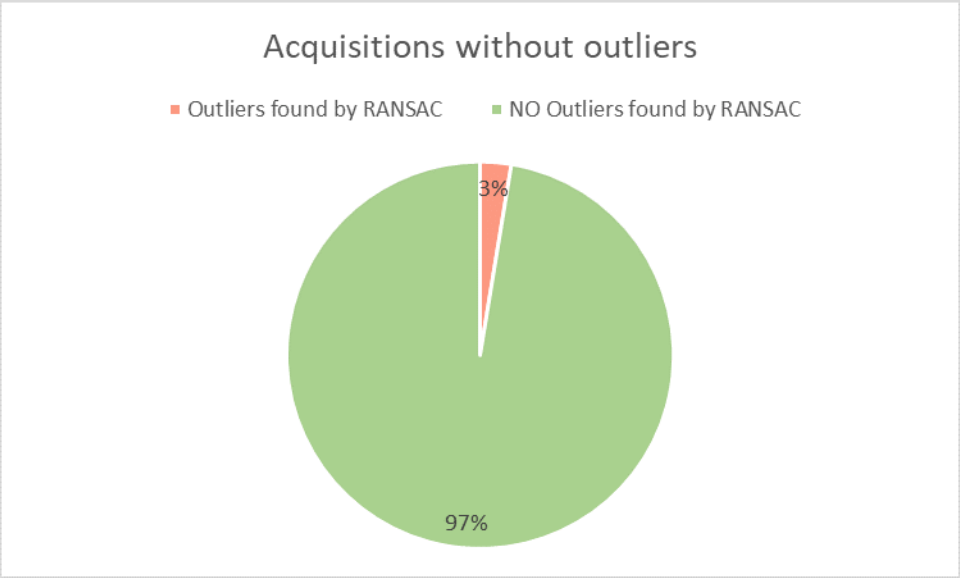

Figure 8.2: Pie chart relative to the acquisitions not affected by outliers.

- in 13 cases the acquisition is particularly bad made, thus leading to high errors: the number of outliers is really high, and the algorithm cannot distinguish them from inliers;
- in 2 cases the acquisitions appear to be well made, but still present high errors probably due to a bias in the RSs.
- in 5 cases, RANSAC algorithm is not applied because the number of acquired point is low: this is the case in which few points are collected, and for the most part, they are badly acquired

To understand if there is a particular factor that causes errors, some investigations have been made.
At first, the rate of occurrences between the different compartments has been studied, finding out that there is no great evidence that one compartment shows more errors compared to the others, but it can be stated that errors are less frequent for tibial plates. The acquisitions involve 4 MPC, 11 LPC, 6 MDC, 6 LDC, 3 TME, 2 TLE.
On the contrary, a dependence on the person that takes the acquisitions can be noticed, since the rate of errors between the three operators is as follows:

- Operator 1: 6 occurrences
- Operator 2: 8 occurrences
- Operator 3: 18 occurrences

Operator 3 has the higher rate of error occurrences, since 56% of the critical cases fall within his acquisitions. Furthermore, operator 3 has the tendency to acquire short

registrations, with less than 40 points (considering that the full acquisition provides 80 points). The length of the acquisition turns out to be an important factor which causes bad results: in these cases, the percentage of outliers on all the acquired points is higher and the chance to fit outliers arises for the algorithm. The acquisitions that have less than 40 points are 16 (50% of the total occurrences with bad results) and in 5 of them the RANSAC is not applied since the number of acquired point is less than the minimum number (15 points).
There is no evidence that the swipe or any other acquisition modality has a higher rate of errors compared with the other, so it can be stated that the errors do not depend on the particular movement done to acquire the surface.

Chapter 9

Conclusion

In conclusion, from the results, it can be state that the proposed method shows consistent results in terms of system performance improvements, following the application of the algorithm, and computational costs.
The worst cases are represented by the acquisitions in which the result, after the RANSAC application, is still far from the desired one. These results belong to really bad acquisitions, which, however, are reported by the system through warnings and can occur due to serious distractions from the surgeon. In some occasions, the algorithm manages to fit a proper surface, and the error decreases, while, in other cases, the error continues to be higher than 1,5 mm, used as a reference value to state if an error implies an appreciable alteration. The errors relative to the cases in which the algorithm is not applied, due to short acquisitions, cannot be handled: it is supposed that if the acquisition lasts less than 1 second, it should not contain outliers.
The rate of errors occurrences appears not to be related to the modality of acquisitions, but the length of the registration constitutes a factor of greater incidence of errors.
The presented method is optimal to correct dataset with few numbers of mistaken points, but has, as might be expected, low performances when the number of outliers increases.
The biggest limit of the algorithm is the operator-dependence, which means that the algorithm's performances are strictly connected to the knowledge of the system's functioning. It is therefore fundamental for a to know which are the wrong movements that will cause a bad planned cut. Since wrong movements are strictly connected with the wrong point's coordinate, it can be stated that the algorithm performances are related to the outliers' number and coordinates. However, this link cannot be unbound, since the acquired points are the input of the filtering function and the entry for the surgical cut planning computed by the software. This is the fundamental passage in the use of CAS systems. A bad acquisition would affect in any case the outcome of the surgery. Differences in results relating to the two validation datasets are a clear demonstration that the deeper the knowledge of how the system works, the more accurate the acquisition will be. A clear explanation of the functioning to surgeons that are going to use the software will lead to a more appropriate use of the system and better results.

Computational times are perfectly compatible with the needs of surgeons, who demand fast systems that do not cause wasted time during the operation.
The doctor's confidence remains an essential requirement to be met in order to maintain a trustful relationship with the customers. Results consistent with expectations increase the surgeon's assuredness in the system.

Chapter 10

Future works

The study presented could be improved in order to lead to better results regardless of the operator that takes the acquisitions and reducing the errors for blinded tests. Another limit of the model is that the results are not optimal when the acquisition, affected by outliers, is short, and thus the percentage of mistaken points on all the acquired points is higher. In this case, the algorithm recognizes the errors as inliers and fits the model over those points. Other constraints could be added to the current model, so that any modality of acquisition is considered and thus any source of outlier is eliminated.
Furthermore, the RANSAC algorithm is a potential tool, that could be used for other purposes to improve the performances of the system.

10.1 Prosthesis size

Studies to define joint surface geometries have been carried out also with the purpose to determine the type of prosthesis that more closely resembles the patient-specific joint anatomy. A proper fit between the prosthesis' component and the dimension of the patient's bone is fundamental for a successful surgery. The proper implant, including the correct size and implant type must be verified before being surgically inserted, in order to avoid any revision surgery in case of a wrong size has been implanted.
All the prosthetic implant companies offer knee prostheses in a variety of sizes, that were determined by designers that studied the anatomy of normal femoral and tibial bones. Subsequently, CT scans were used to compile a database of the "standard" sizes and shapes of the bone of patients who were going to undergo knee replacement.
Traditionally, the surgeon uses plastic overlay templates that are placed over the pre-operative x-rays. Comparing a variety of template sizes and shapes, the surgeon can get a valid suggestion of the implant that is needed. The final determination of size is made at surgery, when the surgeon decides how much bone is going to be removed. Trial components are provided to the surgeon to be put on the bone and assessed for proper fit and soft tissue balance. At that point, small changes to the bony cuts can be made. Finally, permanent implants the same size as the appropriate trial implants are chosen,

and these are then affixed to the bone ends. [24]
The BLU-IGS® system establishes the prosthesis size taking the length in the AP direction as reference dimensions, measuring the distance between the femoral shaft and the most posterior point on the posterior condyle surface. When the surgeon acquires the femoral shaft point, there is not a precise point where the probe should point to. This means that, depending on the surgeon's choice, the prosthesis size could vary, leading to a non-univocal solution.
The RANSAC algorithm could be applied to a set of points acquired on the shaft surface. In this way, a model that fits the bone's morphology in that compartment could be built and the proper point to determine the prosthesis size could be determined, unequivocally. To date, the shaft is acquired as a single point with the BLU-IGS® system: including the RANSAC to this passage would imply that the acquisition should be made in STREAM mode, acquiring a surface. The same strategy could be used to define the best matching surface, that would probably be approximated with a plane parallel to the mechanical axis. The complexity of the model would be reduced compared with the matching problem related to the tibial plates and femoral condyles, since the degree of the fitting surface is reduced both in the 2-D and 3-D approach. The algorithm would be able to remove all the possible outliers acquired during the registration phase and the final point determining the prosthesis size would be extrapolated.

10.2 Centre of the femoral head

The detection of the hip centre is accomplished with just the femoral star, fixed to the femur, and making a circular motion with the lower limb. During this motion, the positions of the femoral rigid body are identified by the cameras and stored in the localizer RS. To determine the centre of the femoral head, some assumptions must be made: the femoral head is a perfect sphere, the pelvic bone has no motion during the acquisition, and the localizer error is 0,0 mm. If these three statements were true, a sphere that best fits the cloud of points obtained during the motion realized by the surgeon would be stored and the centre determined, since any point on the femur would move on the spherical femora head surface.
Unfortunately, none of the assumptions is true and some noise must be taken into account because of the non-spheroid shape of the femoral head, the motion of the pelvic bone during the circular movements, and the limits of accuracy of the optical localizer.
Some approaches were studied to overcome this issue, for example searching for a point in the 3-D space that minimizes the following function [39]:

$$F(c) = \sum_{i=1}^{N} \|c_{i-1} - c_i\|^2 \tag{10.1}$$

where i is the position of the femur at time t and c_i is the corresponding calculated centre. The resulting point can be considered as the point in the 3-D space that has the

smallest trajectory during the acquisition motion.
Another study [27] was carried out to assess the accuracy of an imageless navigation system when localizing the hip centre and evaluate the effect of pelvic movement on the accuracy of this passage. An artificial leg was used to simulate the upper femur and the hip joint, and the centre of the sphere was calculated. Then, four levels of pelvic movements were tested: no movements, moderate movements, severe movements, and critical movements. For each of these types of acquisitions, the difference between the real centre and the computed one was calculated. The results show that the accuracy is not significantly affected by moderate pelvic movements (5 mm) during data acquisition.

As anticipated in Chapter 4, the RANSAC algorithm has already been applied to the localization of the centre of the femoral head in [26]. Due to the many factors that can occur during the surgery, a large amount of erroneous or invalid data may be collected along with useful data and that could cause errors in surface fitting. To solve this problem, the RANSAC algorithm was used in that study with the same steps used for our main purpose but using data from the acquisition of the hip joint and fitting them with a spherical surface. The points which appear to be far from the computed model over a defined threshold are deleted and considered as outliers and the procedure is repeated a number of times in order to find the best model (with the lowest number of outliers). An example is given in Figure 10.1, where the tracked dots are represented together with the sphere centre.

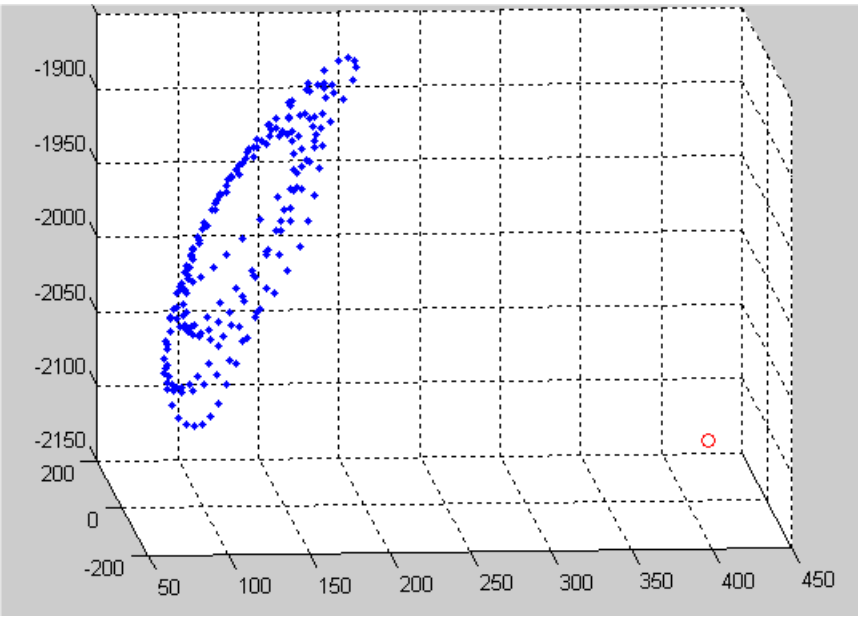

Figure 10.1: Representation of the points acquired during the circular movement of the leg: the blue dots describe the spherical surface of the femoral head, and the red dot is the computed centre. [26]

Since this strategy has already been tested and applied (Zimmer used the RANSAC algorithm for bone tracking with the ORTHOsoft® gyroscope guidance system sensor

in CAS), there is good evidence that the filtering algorithm would work even for the BLU-IGS® system, thus improving more and more the expected performances.

Appendix A

Anatomical planes and axes

Conventionally, to describe the relative movements and positions between different parts of the body, the standard anatomical position is defined as follows: (Figure A.1):

- Standing up position
- Heels joined
- Arms by the side of the body
- Palms facing forward

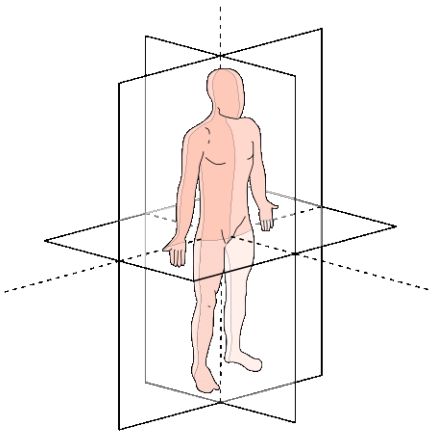

Figure A.1: Standard anatomical position.

According to this position, anatomical planes and axes are defined. Each of the plans divides the human body into two halves.

- Sagittal plane (or Median plane): divides the body into the right and left half
- Coronal plane (or Frontal plane): divides the body into the anterior and posterior half (dorsal and ventral)
- Transverse plane (or Axial plane): divides the body into the superior and inferior half (cranial and caudal)

The three reference axes are perpendicular to each of the anatomical plans (Figure A.2):

- Sagittal axis (antero-posterior): passes horizontally from posterior to anterior and it is perpendicular to the Frontal plane
- Frontal axis (horizontal): passes horizontally from left to right and it is perpendicular to the Sagittal plane
- Longitudinal axis (vertical): passes vertically from inferior to superior and it is perpendicular to the Transverse plane

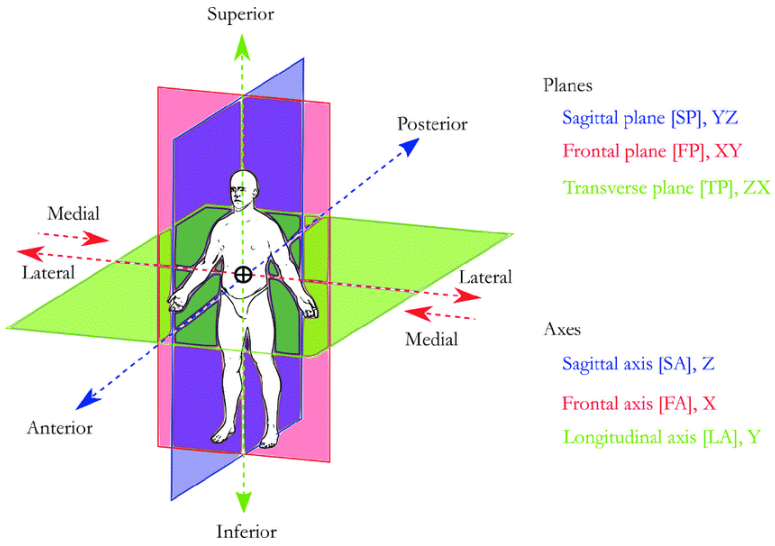

Figure A.2: Anatomical planes and axes.

To be able to make comparisons between different compartments, the following pairs of terms are used (and represented in Figure A.3):

- Superior/Inferior: equivalent to above and below along the longitudinal axis of a body in anatomical position.
- Proximal/Distal: equivalent to near and far, with respect to the longitudinal axis.
- Medial/Lateral: equivalent to towards the middle or towards the edge, with respect to the longitudinal axis.
- Anterior/Posterior: equivalent to the front and back of a body in anatomical position.
- Ventral/Dorsal: equivalent to belly-side and back-side of a body in anatomical position.
- Superficial/Deep: Equivalent to closer to the surface and farther from the surface.
- Cephalic/Caudal: Equivalent to closer to the head and closer to the tail.

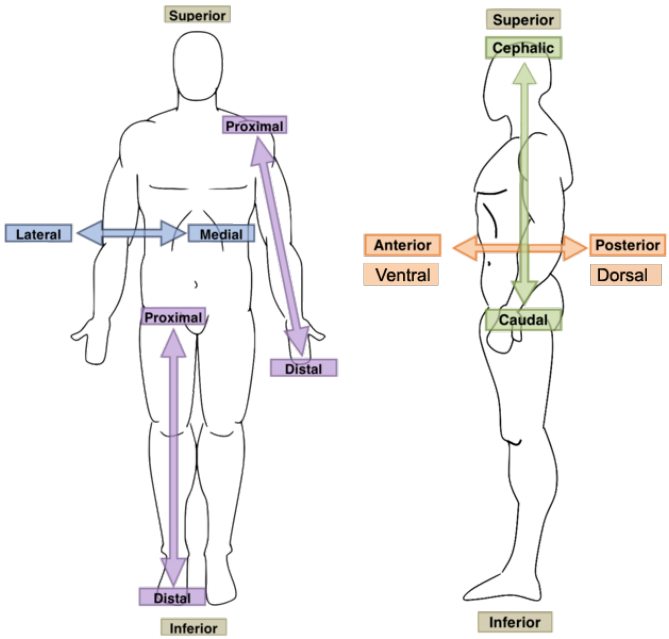

Figure A.3: Pairs of terms providing anatomical direction or orientation.

Appendix B

Position and orientation of rigid bodies in 3-D space

A rigid body can be described in the three-dimensional space by position and orientation of a tri-axial reference system (RS). It is possible to define the position and orientation of a local tri-axial system with respect to the global (fixed) one or with respect to other local reference systems, in case of a multiple body.

Orientation (or rotation) Matrix

With reference to the Figure B.1, we suppose that the triad $Oxyz$ with versors i, j, k corresponds to the absolute RS and that O_iuvw with versors λ, μ, ν is the local reference system associated with the i^{th} body. To determine just the relative orientation between the two systems, we can represent both with a common origin.

In 2-D, it would be as shown in Figures B.2 and B.3:

$$\begin{cases} \lambda = \cos\alpha \cdot i + \cos 90° - \alpha \cdot j = C_{ux} \cdot i + C_{uy} \cdot j \\ \mu = \cos 90° + \alpha \cdot i + \cos\alpha \cdot j = C_{vx} \cdot i + C_{vy} \cdot j \end{cases} \tag{B.1}$$

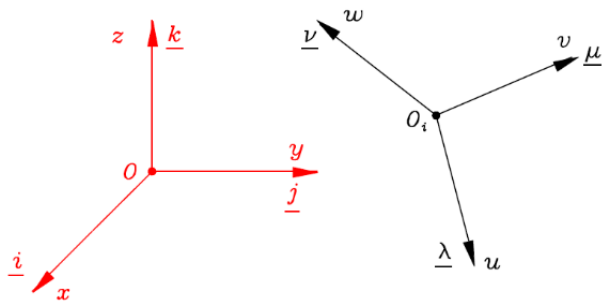

Figure B.1: Global Reference System (red) and local Reference System (black).

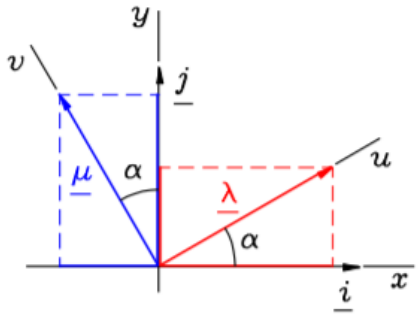

Figure B.2: Relative rotation between global and local Reference Systems.

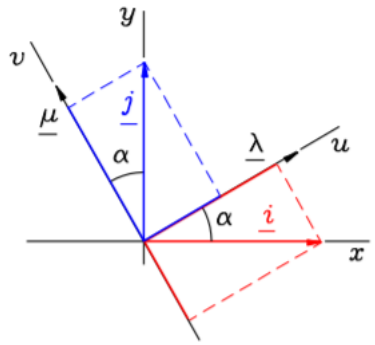

Figure B.3: Relative rotation between global and local Reference Systems.

$$\begin{cases} i = \cos\alpha \cdot \lambda + \cos 90° + \alpha \cdot \mu = C_{xu} \cdot \lambda + C_{xv} \cdot \mu \\ j = \cos 90° - \alpha \cdot \lambda + \cos\alpha \cdot \mu = C_{yu} \cdot \lambda + C_{yv} \cdot \mu \end{cases} \tag{B.2}$$

In 3-D, the local RS O_iuvw can be expressed with respect to the global RS $Oxyz$ as follows:

$$\begin{cases} \lambda = C_{ux} \cdot \mathbf{i} + C_{uy} \cdot \mathbf{j} + C_{uz} \cdot \mathbf{k} \\ \mu = C_{vx} \cdot \mathbf{i} + C_{vy} \cdot \mathbf{j} + C_{vz} \cdot \mathbf{k} \\ \nu = C_{wx} \cdot \mathbf{i} + C_{wy} \cdot \mathbf{j} + C_{wz} \cdot \mathbf{k} \end{cases} \tag{B.3}$$

where the components of each versor are called direction cosine, i.e. the projections of a versor along the different axes of the global reference system.

$$\begin{cases} C_{xu} = C_{ux} = \cos\alpha = \lambda \cdot i \\ C_{xv} = C_{vx} = \cos 90° + \alpha = \mu \cdot i \\ C_{yu} = C_{uy} = \cos 90° - \alpha = \lambda \cdot j \\ C_{yv} = C_{vy} = \cos\alpha = \mu \cdot j \end{cases} \tag{B.4}$$

Expressing the versors λ, μ, ν in compact formulation, we have:

$$\begin{bmatrix} C_{ux} & C_{vx} & C_{wx} \\ C_{uy} & C_{vy} & C_{wy} \\ C_{uz} & C_{vz} & C_{wz} \end{bmatrix} = \begin{bmatrix} \lambda & \mu & \nu \end{bmatrix} = {}^0A_i \tag{B.5}$$

The direction cosine matrix ${}^0A_i$ is called the orientation matrix and the terms of which it is composed have specific characteristics:

- each column is a versor, therefore it has a unitary module
- the versors are orthogonal to each other, therefore their scalar product is zero

The orientation matrix therefore expresses the rotation that must be carried out around an appropriate axis to overlap the axes of the local RS to the global one.

Positioning (or transformation) Matrix

The transformation matrices define both the relative position and the relative orientation between two different RS in a 3-D space, as represented in Figure B.4. The figure represents a point (R) attached to the local RS, which rotates and translates with respect to the global RS.

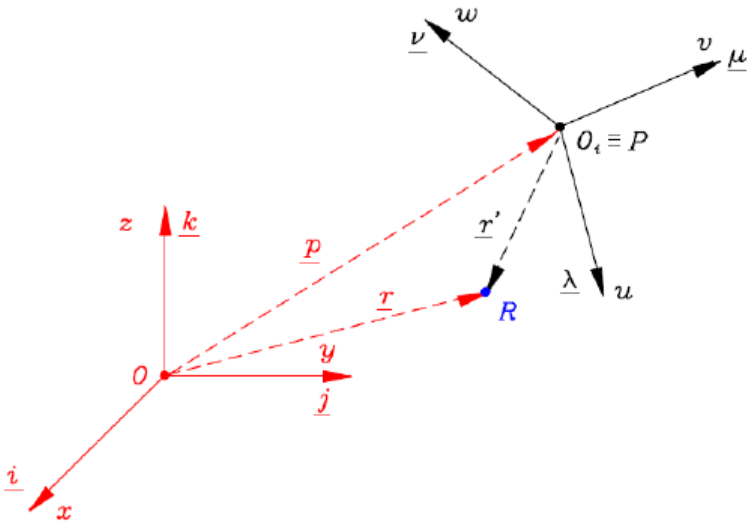

Figure B.4: Representation of a point R in three different coordinates systems: 1) r: position of R in the global RS; 2) r ': position of R in the local RS; 3) p: position of the origin of the local RS compared to the global one.

To express all the terms with respect to the global RS, we would have the following transformation:

$$r = r' + p = {}^0A_i \cdot {}^ir' + p \tag{B.6}$$

$$\begin{cases} r_x = C_{ux} \cdot r'_u + C_{vx} \cdot r'_v + C_{wx} \cdot r'_w + p_x \\ r_y = C_{uy} \cdot r'_u + C_{vy} \cdot r'_v + C_{wy} \cdot r'_w + p_y \\ r_y = C_{uz} \cdot r'_u + C_{vz} \cdot r'_v + C_{wz} \cdot r'_w + p_z \\ 1 = 0 + 0 + 0 + 1 \end{cases} \tag{B.7}$$

$$\begin{bmatrix} r_x \\ r_y \\ r_z \\ 1 \end{bmatrix} = \begin{bmatrix} C_{ux} & C_{vx} & C_{wx} & p_x \\ C_{uy} & C_{vy} & C_{wy} & p_y \\ C_{uz} & C_{vz} & C_{wz} & p_z \\ 0 & 0 & 0 & 1 \end{bmatrix} \cdot \begin{bmatrix} r'_u \\ r'_v \\ r'_w \\ 1 \end{bmatrix} \tag{B.8}$$

$$\begin{bmatrix} C_{ux} & C_{vx} & C_{wx} & p_x \\ C_{uy} & C_{vy} & C_{wy} & p_y \\ C_{uz} & C_{vz} & C_{wz} & p_z \\ 0 & 0 & 0 & 1 \end{bmatrix} = {}^0A_i \tag{B.9}$$

${}^0A_i$ is called positioning or transformation matrix. The first three columns represent the orientation of the local axes u, v, w in the global reference (0), the fourth column represents the coordinates of the origin of the uvw RS. It therefore represents the position and orientation of the local RS and of the points attached to it, with respect to the global RS; if the two systems have the same origin, the transformation matrix would become a simple rotation matrix.

Appendix C

Principal Component Analysis

Principal Component Analysis (PCA) is a statistical procedure that uses an orthogonal transformation to convert a set of observations of possibly correlated variables into a set of values of linearly uncorrelated variables called principal components. When the number of the variables is high and the relationship between them is not known, there is the risk of overfitting the model to the data and thus the need to reduce the dimension of the feature space.
The dimensionality reduction can be achieved through:

- Feature Elimination: the reduction of the feature space passes through the elimination of some of them
- Feature Extraction: a set of "new" independent variables are created, in which every new variable is a combination of the old ones

Principal component analysis is a technique for feature extraction, with which we can obtain a set of independent variables. The final aim is to identify the most important "directions", so that the data can be projected into a smaller space, reducing the dimensionality of the feature space.
The procedure is composed of the following steps:

1. Given the matrix of the features X, we subtract the mean from each entry, in order to centre it and standardize it, obtaining the new matrix Z.
2. The matrix of the covariance is constructed, as follows: $Z^T Z$.
3. The eigenvalues and eigenvectors of this matrix are evaluated and sorted: we obtain the new matrix of eigenvectors P^*. The eigenvectors are independent of one other.
4. We calculate the matrix $Z^* = ZP^*$. The columns of Z^* are independent of one other. This matrix represents the principal components of the system.
5. We can now decide to keep the first k features, by eliminating the remaining ones.
6. The transformation from the original n dimensional data points into k dimensions is done.

Let's consider a dataset in only two dimensions [47]. The dataset can be plotted as points in a plane, but if we want to tease out variation, PCA finds a new coordinate system in which every point has a new (x, y) value. In Figure C.1 we see the capacity of PCA to eliminate dimensions: with the transformation in another reference system, the data are represented along one dimension. It is now easy to deduct the principal component, which is the one with most variation. In this case, we don't lose much by dropping pc2 since it contributes the least to the variation in the data set. The difference is evident in Figure C.2, where the data are plotted along a pair of lines: one composed of the x-values and another of the y-values in the first case, one composed of the pc1-values and another of the pc2-values in the second one.

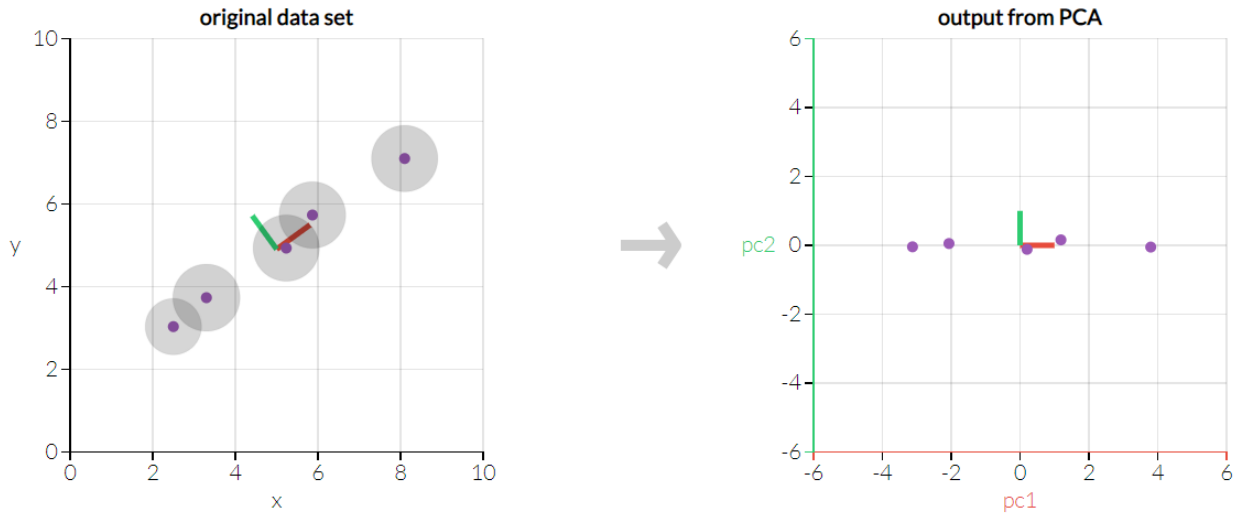

Figure C.1: Example of an application of the PCA: in the first plot, the data set is represented in the original reference system, made up by two different features. We cannot easily see a clear correlation between the axis. In the second plot, there is an evidence of the importance of the pc1 compared to pc2. [47]

Figure C.2: Representation of the data along lines, before and after the application of PCA. [47]

Appendix D

C++ code

The C++ code which has been implemented in Visual Studio® is presented in this Appendix. To make it clear, the different passages are reported separately.

Main

In the main function (D.1), the conditions of RANSAC are imposed: the first filter on physiological range is applied; the algorithm starts only if the number of acquisitions is ≥ 15; the 3-D model is applied if the data in the ML direction have a range $\geq \delta$; if the right convexity is not found with the 3-D model, the 2-D model is applied. Different functions are applied for different compartments.

Listing D.1: RANSAC main pseudocode C++

```
int main(int, char const*[])
{
    RansacCalculator calculator = RansacCalculator();
    vector<vector<float>> matrice = calculator.readMatrix("MDC.txt")
        ;
    char limb = 'R';
    string surface = "dist"; //"post"
    string compart = "MDC"; //'LPC';'MDC';'LDC';'TME';'TLE';
    double delta = 6.5;
    float threshold = 1.2;
    // Physiological range
    vector<vector<float>> matrix = calculator.physiologicFilter(
        matrice, limb, compart);
    // Ransac Application
    vector<int> inliers = calculator.ransacEvaluation( matrix, delta
        , threshold, limb, surface);
     return 0;
}
```

Physiological Range

As explained in 5.1.7, the RANSAC algorithm takes as input all the acquired points which fall within some defined ranges. The acquired points on the bone surface are then transformed into the anatomical RS, and then the coordinates of the principal relative axis are analysed. In the D.2 code, *dim* is the number of acquired points and *matrice* is the matrix of acquired points expressed in the anatomical RS. The matrix is organized in three rows, representing the x, y, and z coordinates in mm, and a number of columns equal to the points acquire during the registration phase (*dim*). The limb is given in input as *'L'* (left) or *'R'* (right), as well as the compartment.

Listing D.2: Deletion of points out of physiological ranges pseudocode C++

```
vector<vector<float>> RansacCalculator::physiologicFilter( vector<
    vector<float>> matrice, char limb, std::string sCompartment )
{
    int dim = matrice[0].size();
    vector<vector<float>> newMatrice( 4 );
    int axis = 2;
    float fRMin = 30.;
    float fRMax = 50.;
    if( sCompartment == "MPC" )
    {
        if( limb == 'L' )
        {
            fRMin = 30.;
            fRMax = 50.;
        }
        else
        {
            fRMin = -50.;
            fRMax = -30.;
        }
        axis = 1;
    }
    if( sCompartment == "LPC" )
    {
        if( limb == 'L' )
        {
            fRMin = 25.;
            fRMax = 50.;
        }
        else
        {
            fRMin = -50.;
            fRMax = -25.;
        }
        axis = 1;
    }
    if( sCompartment == "MDC" || sCompartment == "LDC" )
    {
        if( limb == 'L' )
        {
            fRMin = -25.;
```

```
            fRMax = 5.;
        }
        else
        {
            fRMin = -5.;
            fRMax = 25.;
        }
    }
    if( sCompartment == "TME" || sCompartment == "TLE" )
    {
        if( limb == 'L' )
        {
            fRMin = -10.;
            fRMax = 5.;
        }
        else
        {
            fRMin = -5.;
            fRMax = 10.;
        }
    }
    for( int j = 0; j < dim; j++ )
    {
        if( matrice[axis][j] > fRMin && matrice[axis][j] < fRMax )
        {
            newMatrice.at( 0 ).push_back( matrice[0][j] );
            newMatrice.at( 1 ).push_back( matrice[1][j] );
            newMatrice.at( 2 ).push_back( matrice[2][j] );
            newMatrice.at( 3 ).push_back( matrice[3][j] );
        }
    }
    return newMatrice;
}
```

Ransac function

As an example, the function used for the distal condyles and the tibial plates are presented, using a 3-D model.

Listing D.3: 3-D fitting model pseudocode C++

```
vector<int> RansacCalculator::ransacEvaluation( vector<vector<float
    >> matrix, double delta, float threshold, char limb, std::string
     surface )
{
    vector<int> inliers;
    int p = matrix.at( 0 ).size();
    if( p > 15 )
    {     // delta evaluation
        double xMin = *min_element( matrix[0].begin(), matrix[0].end
            () );
        double xMax = *max_element( matrix[0].begin(), matrix[0].end
            () );
```

```
        double rangeX = fabs( xMin - xMax );
        if( rangeX > delta ) // 3D
        {
            if( surface == "post" )
            {
                inliers = ransac3d_post(matrix, threshold);
                if( inliers.size() == 0)
                    inliers = ransac_post(matrix, threshold);
            }
            else
            {
                inliers = ransac3d_dist(matrix, limb, threshold);
                if( inliers.size() == 0 )
                    inliers = ransac_dist(matrix, limb, threshold);
            }
        }
        else // 2D
        {
            if(surface == "post")
                inliers = ransac_post(matrix, threshold);
            else
                inliers = ransac_dist(matrix, limb, threshold);
        }
    }
    return inliers;
}
vector<int> RansacCalculator::ransac3d_dist(vector<vector<float>>
    data, char limb, float threshold)
{
    const int l = data[0].size();
    int outNum = l;
    vector<int> inliers;
    float maxX = *max_element( data[0].begin(), data[0].end() );
    float minX = *min_element( data[0].begin(), data[0].end() );
    const int nx = 50;
    vector<float> rangex = linspace( minX, maxX, nx );
    float maxY = *max_element( data[1].begin(), data[1].end() );
    float minY = *min_element( data[1].begin(), data[1].end() );
    const int ny = 48;
    vector<float> rangey = linspace( minY, maxY, ny );
    int niter = 40;
    int iter = 0;
    while( iter < niter )
    {
        vector<int> V1( l );
        for( int i = 0; i < l; i++ )
        {
            V1[i] = i;
        }
        std::random_device rd;
        std::mt19937 g( rd() );
        std::shuffle( V1.begin(), V1.end(), g );
        vector<int> v1( 6 );
        for( int i = 0; i < 6; i++ )
        {
            v1[i] = V1[i];
```

```
        }
        vector<int> inlIdx = fit3d_dist( data, v1, nx, ny, rangex,
            rangey, threshold, limb );
        int inlNum = inlIdx.size();
        if( inlNum > 5 )
        {
            vector<int> newInlIdx = fit3d_dist( data, inlIdx, nx, ny,
                rangex, rangey, threshold, limb );
            int newinlNum = newInlIdx.size();
            if( l - newinlNum < outNum )
            {
                outNum = l - newinlNum;
                inliers = newInlIdx;
            }
            if( outNum == 0 )
            {
                break;
            }
        }
        iter = iter + 1;
    }
    return inliers;
}
vector<int> RansacCalculator::fit3d_dist( vector<vector<float>>
    data, vector<int> index, int nx, int ny, vector<float> rangex,
    vector<float> rangey, float threshold, char limb )
{
    int l;
    l = index.size();
    int n;
    n = data[0].size();
    Vector3<double> points[80];
    for( int a = 0; a < l; a++ )
    {
        Vector3<double> p = Vector3<double>();
        int ind = index[a];
        p[0] = data[0][ind];
        p[1] = data[1][ind];
        p[2] = data[2][ind];
        points[a] = p;
    }
    double coeff[6];
    ApprParaboloid3<double> pp;
    double out = pp( l, points, coeff );
    double c1;
    double c2;
    if( limb == 'L' )
    {
        c1 = coeff[0];
        c2 = coeff[2];
    }
    else
    {
        c1 = -coeff[0];
        c2 = -coeff[2];
    }
```

```
    if( c1 > 0 && c2 > 0 )
    {
        vector<vector<float>> values = vector<vector<float>>( nx );
        for( int i = 0; i < nx; i++ )
        {
            float val;
            vector<float> row( ny );
            for( int j = 0; j < ny; j++ )
            {
                val = ( coeff[0] * pow( rangex[i], 2 ) + coeff[1] *
                    rangex[i] * rangey[j] + coeff[2] * pow( rangey[j], 2
                     ) + coeff[3] * rangex[i] + coeff[4] * rangey[j] +
                    coeff[5] );
                row[j] = val;
            }
            values[i] = row;
        }
        vector<float> distMin = vector<float>( n );
        for( int h = 0; h < n; h++ )
        {
            float dMin = std::numeric_limits<float>::max();
            for( int i = 0; i < nx; i++ )
            {
                float d;
                for( int j = 0; j < ny; j++ )
                {
                    d = ( pow( ( rangex[i] - data[0][h] ), 2 ) + pow( (
                        rangey[j] - data[1][h] ), 2 ) + pow( ( values[i][
                        j] - data[2][h] ), 2 ) );
                    if( d < dMin )
                        dMin = d;
                }
            }
            distMin[h] = dMin;
        }
        vector <int> currentInliers;
        for( int h = 0; h < n; h++ )
        {
            if( distMin[h] <= threshold * threshold )
            {
                currentInliers.push_back( h );
            }
        }
        return currentInliers;
    }
    else
    {
        vector<int> currentInliers;
        return currentInliers;
    }
}
```

Bibliography

[1] Saverio Affatato. *Surgical Techniques in Total Knee Arthroplasty (TKA) and Alternative Procedures*. 2014.

[2] Alireza Ahmadian, Anahita Fathi Kazerooni, Saeed Mohagheghi, Keyvan Amini Khoiy, and Moosa Sadr Hosseini. A region-based anatomical landmark configuration for sinus surgery using image guided navigation system: A phantom-study. *Journal of Cranio-Maxillofacial Surgery*, 2014.

[3] O. G. Avrunin, M. Alkhorayef, Husham Farouk Ismail Saied, and M. Y. Tymkovych. The surgical navigation system with optical position determination technology and sources of errors. *Journal of Medical Imaging and Health Informatics*, 2015.

[4] N. Baka, B. L. Kaptein, M. de Bruijne, T. van Walsum, J. E. Giphart, W. J. Niessen, and B. P.F. Lelieveldt. 2D-3D shape reconstruction of the distal femur from stereo X-ray imaging using statistical shape models. *Medical Image Analysis*, 2011.

[5] Paul J. Besl and Neil D. McKay. A Method for Registration of 3-D Shapes. *IEEE Transactions on Pattern Analysis and Machine Intelligence*, 1992.

[6] Mirza Biščević, Mujo Hebibović, and Dragica Smrke. Variations of femoral condyle shape. *Collegium Antropologicum*, 2005.

[7] Ortopedia Traumatologia Borgotaro. Il fallimento di una protesi articolare: la chirurgia di revisione. Quando ne ho bisogno?, 2017.

[8] Carolyn S. K. Chan, Philip J. Edwards, and David J. Hawkes. Integration of ultrasound-based registration with statistical shape models for computer-assisted orthopaedic surgery. In *Medical Imaging 2003: Image Processing*, 2003.

[9] Jiun Hung Chen, Ke Colin Zheng, and Linda G. Shapiro. 3D point correspondence by minimum description length in feature space. In *Lecture Notes in Computer Science (including subseries Lecture Notes in Artificial Intelligence and Lecture Notes in Bioinformatics)*, 2010.

[10] Xiaozhong Chen, Kunjin He, Zhengming Chen, and Lin Wang. A parametric approach to construct femur models and their fixation plates. *Biotechnology and Biotechnological Equipment*, 2016.

[11] Chum. Locally Optimized RANSAC. 2003.

[12] Marzieh Ershad, Alireza Ahmadian, Nassim Dadashi Serej, Hooshang Saberi, and Keyvan Amini Khoiy. Minimization of target registration error for vertebra in image-guided spine surgery. *International Journal of Computer Assisted Radiology and Surgery*, 2014.

[13] Carol Eustice. What You Should Know About Total Knee Replacement Surgery, 2019.

[14] Stefano Zaffagnini Fabio Catani. *Knee Surgery Using Computer Assisted Surgery and Robotics*. 2013.

[15] Martin A. Fischler and Robert C. Bolles. Random sample consensus: A Paradigm for Model Fitting with Applications to Image Analysis and Automated Cartography. *Communications of the ACM*, 1981.

[16] J. M. Fitzpatrick. The role of registration in accurate surgical guidance. *Proceedings of the Institution of Mechanical Engineers, Part H: Journal of Engineering in Medicine*, 2010.

[17] Markus Fleute and Stéphane Lavallée. Building a complete surface model from sparse data using statistical shape models: Application to computer assisted knee surgery. In *Lecture Notes in Computer Science (including subseries Lecture Notes in Artificial Intelligence and Lecture Notes in Bioinformatics)*, 1998.

[18] Markus Fleute, Stéphane Lavallée, and Rémi Julliard. Incorporating a statistically based shape model into a system for computer-assisted anterior cruciate ligament surgery. *Medical Image Analysis*, 1999.

[19] Javad Hashemi, Naveen Chandrashekar, Brian Gill, Bruce D. Beynnon, James R. Slauterbeck, Robert C. Schutt, Hossein Mansouri, and Eugene Dabezies. The geometry of the tibial plateau and its influence on the biomechanics of the tibiofemoral joint. *Journal of Bone and Joint Surgery - Series A*, 2008.

[20] Anders Hast, Johan Nysjö, and Andrea Marchetti. Optimal RANSAC - Towards a repeatable algorithm for finding the optimal set. *Journal of WSCG*, 2013.

[21] D. S. Hungerford. Alignment in total knee replacement. *Instructional course lectures*, 1995.

[22] MD Jared R. H. Foran. Total Knee Replacement.

[23] Raviprasad Kattimani. Component Alignment in Total knee Replacement. *Orthopedics and Rheumatology Open Access Journal*, 2018.

[24] Richard S. Laskin. Total Knee Replacement at HSS: One Size Does Not Fit All, 2009.

[25] Karim Lekadir, Robert Merrifield, and Guang Zhong Yang. Outlier detection and handling for robust 3-D active shape models search. *IEEE Transactions on Medical Imaging*, 2007.

[26] Jian Wu Li and Ang. A Computer-Assisted Non-Image-Based Method for Locating the Center of Femoral Head. *International Journal of Bioscience, Biochemistry and Bioinformatics*, 3(5):4, 2013.

[27] Sebastien Lustig, Cyrille Fleury, Elvire Servien, Guillaume Demey, Philippe Neyret, and Simon T. Donell. The effect of pelvic movement on the accuracy of hip centre location acquired using an imageless navigation system. *International Orthopaedics*, 2011.

[28] F. E. Milano, L. E. Ritacco, G. Farfalli, L. Aponte-Tinao, F. González Bernaldo De Quirós, and M. Risk. An algorithm for automatic surface labeling of planar surgical resections. In *Journal of Physics: Conference Series*, 2011.

[29] A. P. Monk, K. Choji, J. J. O'Connor, J. W. Goodfellow, and D. W. Murray. The shape of the distal femur: A geometrical study using MRI. *Bone and Joint Journal*, 2014.

[30] Oliver Jones. The Knee Joint, 2019.

[31] Physiopedia. Knee, 2020.

[32] S. Plaweski, A. Pearle, C. Granchi, and R. Julliard. PRAXIM ACL navigation system using bone morphing. In *Navigation and MIS in Orthopaedic Surgery*. 2007.

[33] Kamil Říha Radek Beneš, Martin Hasmanda. Non-linear RANSAC method and its utilization. *Elektrorevue*, 2(4):8, 2011.

[34] Kumar T. Rajamani, Johannes Hug, Lutz P. Nolte, and Martin Styner. Bone morphing with statistical shape models for enhanced visualization. In *Medical Imaging 2004: Visualization, Image-Guided Procedures, and Display*, 2004.

[35] Istituto Ortopedico Rizzoli. Ginocchio: La protesi di ginocchio, 2017.

[36] W Norman Scott. Insall and Scott, Surgery of the Knee. In *volumen 2, Capitulo 79*. 2007.

[37] Eun-Kyoo Song, Jong-Keun Seon, Jae-Young Moon, and Yim Ji. The Evolution of Modern Total Knee Prostheses. In *Arthroplasty - Update*. 2013.

[38] E. Stindel, J. L. Briard, C. Plaskos, and J. Troccaz. Navigated total knee arthroplasty and the surgetics bone-morphing system. In *Navigation and MIS in Orthopaedic Surgery*. 2007.

[39] Eric Stindel, J. L. Briard, P. Merloz, S. Plaweski, F. Dubrana, C. Lefevre, and J. Troccaz. Bone morphing: 3D morphological data for total knee arthroplasty. *Computer Aided Surgery*, 2002.

[40] Richard Szeliski and Stéphane Lavallée. Matching 3-D anatomical surfaces with non-rigid deformations using octree-splines. *International Journal of Computer Vision*, 1996.

[41] Gary K.L. Tam, Zhi Quan Cheng, Yu Kun Lai, Frank C. Langbein, Yonghuai Liu, David Marshall, Ralph R. Martin, Xian Fang Sun, and Paul L. Rosin. Registration of 3d point clouds and meshes: A survey from rigid to Nonrigid, 2013.

[42] C. Van Sikes Thomas Parker Vail, Jason E. Lang. Surgical Techniques and Instrumentation in Total Knee Arthroplasty, 2016.

[43] Nicola Pace Ugo De Nicola. *La protesi di ginocchio di primo impianto*. 2005.

[44] Marin Uhečírk, Jan Kybic, Herv Liebgott, and Christian Cachard. Model fitting using RANSAC for surgical tool localization in 3-D ultrasound images. *IEEE Transactions on Biomedical Engineering*, 2010.

[45] M. Valenti, C. Chen, E. de Momi, G. Ferrigno, and G. Zheng. 3D Shape landmark correspondence by Minimum Description Length and local linear regularization. In *IFMBE Proceedings*, 2014.

[46] Dawie J. Van Den Heever, Cornie Scheffer, Pieter Erasmus, and Edwin Dillon. Mathematical reconstruction of human femoral condyles. *Journal of Biomechanical Engineering*, 2011.

[47] Lewin Lehe Victor Powell. Principal Component Analysis, 2015.

[48] Hanzi Wang, Daniel Mirota, Masaru Ishii, and Gregory D. Hager. Robust motion estimation and structure recovery from endoscopic image sequences with an adaptive scale Kernel Consensus estimator. In *26th IEEE Conference on Computer Vision and Pattern Recognition, CVPR*, 2008.

[49] Zixu Yan, Feng Chen, and Dexing Kong. Liver venous tree separation via twin-line ransac and murray's law. *IEEE Transactions on Medical Imaging*, 2017.

[50] Zanchettin. *Algoritmo di RANSAC: panoramica, confronti e applicazioni*. PhD thesis, 2013.

[51] David Zelman. Osteoarthritis of the Knee (Degenerative Arthritis of the Knee), 2019.

Ringraziamenti

Questo lavoro di tesi è il risultato di un percorso che mi ha vista maturare consapevolezze, rapporti, mentalità, sogni, prima ancora delle competenze. Un complesso e soddisfacente punto esclamativo da inserire al fondo di una pagina bella e non sempre facile della mia vita, chiamata università. Ogni persona incrociata in questo cammino ha lasciato in me un piccolo o grande segno, rendendomi ciò che sono oggi. Queste pagine sono anche le vostre.

Grazie alla mia relatrice, la prof.ssa Bignardi, dalla quale mi sono sentita ispirata, incoraggiata, sostenuta, anche quando non era dovuto. La professionalità a volte basta per fare bene il proprio lavoro, ma l'empatia mostratami rimarrà oltre questi numeri.

Grazie ai miei correlatori Simone e Ruben, per aver condiviso con me una piccola ma preziosa parte di questo mestiere, che oggi mi incanta ancor di più rispetto a ieri, e a Nick, Fabri, Lauretta, Linda e tutti i colleghi di Orthokey, per avermi inondata col vostro affetto e la vostra infinita energia.

Grazie a Mamma e Papà per avermi permesso di vivere tutto questo, per aver appoggiato sempre e con amore le mie scelte e per i sacrifici che non mi avete mai fatto pesare. Vorrei un giorno riuscire ad essere quello che voi siete per me. Grazie a mio fratello e a Vale, per essere una preziosa costante nella mia vita e per avermi fatto il regalo più bello: Beatrice.
Grazie alla mia famiglia, perchè in me vive un'eredità fatta dei vostri valori.

Grazie alle mie compagne di viaggio. A Chiara per ogni tua parola di conforto, ma ancor di più per quelle che mi hanno fatto male, perché si sono rivelate sempre la cosa di cui avevo più bisogno, e a Micol per ogni tuo sorriso nato dopo la tempesta, perché ogni volta che sei rinata, io l'ho fatto con te. Ogni nostra vittoria è valsa il triplo, per me. Grazie a Sara, per la complicità che si è creata tra di noi, per le nostre merende consolatorie e perché con nessun altro avrei indossato il pigiama nel bagno del Poli.

Grazie a Martina, perchè sei da sempre un porto sicuro con cui "condividere il silenzio in santa pace". Crescere insieme è un privilegio.

Grazie a chi ha fatto parte della mia vita in questi anni, continuando a camminarmi accanto giorno dopo giorno, cambiando insieme a me, nonostante la distanza, e a chi ha preso strade diverse. Il suono dei nostri passi è stato casa, per me.

Grazie ai miei amici pazzi, perchè da quando ci siete, avete colorato le mie giornate e in modo speciale a Edoardo, per essere un punto di riferimento dai tempi in cui "non sapevo manco 'ndo stavo".

Grazie a Raffaella, Rachele e Francesco, per aver condiviso con me una delle avventure più belle e intense della mia vita e perchè Tel Aviv non sarebbe stata la stessa senza di voi.

Grazie ad Andrea, per continuare a tenermi la mano, ovunque, stringendo nell'altra i nostri sogni.

A me, invece, voglio dire grazie per tutte le volte in cui ho creduto di non farcela, per tutti gli ostacoli che fino alla fine sembravano troppo grandi per essere affrontati, perchè la burrasca che ha stravolto questi anni ha lasciato "il sole nella coda del vento".

“[...]
Io sono,
io sono il giorno,
sono
la luce.
Per questo
ho
doveri di mattina
impegni di pomeriggio.
Devo
andare
con il vento e l’acqua,
aprire finestre,
abbattere porte,
rompere muri,
illuminare angoli.
Non posso
starmene seduto.
A presto.
Domani
ci rivedremo.
Oggi ho molte
battaglie da vincere.
Oggi ho molte ombre
da squarciare e sconfiggere.
Oggi non posso
stare con te, devo
portare a termine il mio compito
di luce:
andare e venire per le strade,
le case e gli uomini
sconfiggendo
l’oscurità. Io devo
farmi in mille
finché tutto sia giorno,
finché tutto sia chiarore
e allegria sulla terra.”

Ode al chiarore, Pablo Neruda